FREQUENCY SHIFTS DURING SPIN-EXCHANGE OPTICAL PUMPING OF ^{3}He AND ^{129}Xe AND APPLICATIONS OF HYPERPOLARIZED ^{129}Xe

by

Zayd Ma

A dissertation submitted to the faculty of
The University of Utah
in partial fulfillment of the requirements for the degree of

Doctor of Philosophy

in

Physics

Department of Physics and Astronomy

The University of Utah

Dcember 2012

The University of Utah Graduate School

STATEMENT OF DISSERTATION APPROVAL

This dissertation of Zayd Ma

has been approved by the following supervisory committee members:

Brian Saam	, Chair	September 25, 2012 Date Approved
Christoph Boehme	, Member	September 25, 2012 Date Approved
Oleg Starykh	, Member	September 25, 2012 Date Approved
Stephan LeBohec	, Member	September 25, 2012 Date Approved
David Goldenberg	, Member	September 25, 2012 Date Approved

and by David Kieda, Chair of

the Department of Physics and Astronomy

and by Charles A. Wight, Dean of the Graduate School.

ABSTRACT

This thesis is focused on the fundamental physics of spin-exchange optical pumping (SEOP) and a few applications of the resultant hyperpolarized ^{129}Xe.

During SEOP, noble-gas and Rb atoms repeatedly collide. During these collisions the Rb valence-electron wavefunction overlaps with the noble-gas nucleus and if either the noble-gas nuclei or Rb electrons are highly spin-polarized then the other will experience, on average, a small additional magnetic field that will manifest itself as a shift in the Larmor frequency. The size of the frequency shift is proportional to the magnetization of the polarized atoms and consequently can be used to perform polarimetry. In this thesis, pulsed NMR was used to measure ^{3}He and ^{129}Xe Larmor frequency shifts, and optically detected continuous-wave electron paramagnetic resonance (EPR) was used to monitor the ^{87}Rb hyperfine transition frequencies.

A successful calibration of the size of the frequency shift due to ^{129}XeRb collisions was done and, using this calibration, preliminary ^{129}Xe polarimetry data were acquired by monitoring the ^{87}Rb EPR frequency inside the Utah flow-through polarizer. The ^{129}Xe polarimetry results were inconclusive due to an unexplained result regarding the sign of the frequency shift; however extensive progress was made in understanding the systematics associated with this type of measurement.

Hyperpolarized ^{129}Xe from the Utah flow-through polarizer was also used to perform measurements with unprecedented precision of the T_1 time of ^{129}Xe in Xe frozen as "ice" and "snow." In addition, hyperpolarized ^{129}Xe was also used in a study focused on interaction of dissolved Xe with wild-type and several mutants of bovine pancreatic trypsin inhibitor (BPTI) protein.

“If your mother says she loves you, make sure you check it out.” - B.T.S.

CONTENTS

ABSTRACT . . . . . **iii**

LIST OF FIGURES . . . . . **viii**

LIST OF TABLES . . . . . **xi**

ACKNOWLEDGMENTS . . . . . **xii**

CHAPTERS

1. INTRODUCTION **1**

1.1 Spin-Exchange Optical Pumping 1
1.1.1 Brief History of Optical Pumping and Spin Exchange 1
1.1.2 Optical Pumping of Rb 2
1.1.3 Rb–Noble-Gas Spin Exchange 5
1.1.4 Practical SEOP 8
1.2 Magnetic Resonance 8
1.2.1 Spins in a Magnetic field 8
1.2.2 Excitation and Detection 10

2. MEASUREMENT OF THE FREQUENCY SHIFT ENHANCEMENT FACTOR DURING RB-XE COLLISIONS **14**

2.1 Introduction 14
2.2 Experiment Design 16
2.3 Apparatus 17
2.4 Data Acquisition 20
2.5 Data Analysis and Discussion 23
2.5.1 ^{129}Xe Diffusion Measurement 29
2.5.2 "Chemical" Exchange Between Regions of Polarized and Unpolarized Rb 30
2.5.2.1 ^{129}Xe Flip Angle Dependence of $(\kappa_0)_{\mathrm{RbXe}}$ 34
2.5.3 ^{129}Xe Imaging to Verify Noble Gas Homogeneity 34
2.5.4 SEOP at High Field: σ_+ and σ_- Energy Shift 35
2.5.5 Numerical Modeling of the Geometric Effect 36
2.5.6 High Xe Concentration Data 38
2.5.7 Molecular Considerations 40
2.6 Conclusions 41

3. ^{129}XE POLARIMETRY USING THE SHIFT OF ^{87}RB HYPERFINE TRANSITION FREQUENCIES **43**

3.1 Introduction 43
3.2 The Utah Flow-Through Polarizer 44

3.3 ^{87}Rb in a Magnetic Field 47
3.4 Steady State Excitation of Rb Hyperfine Transitions While Optically Pumping 50
3.5 Alkali Spin Precession Detected via Transverse Faraday Rotation 53
3.6 ^{87}Rb EPR Detection Apparatus 54
3.6.1 Simple and Inexpensive High-Current Stabilization with an Inductive Load 59
3.7 Data and Discussion 62
3.7.1 Light Shifts 64
3.7.2 Alkali-Alkali Spin Exchange 68
3.7.3 Hyperfine Resonance Shift Due to Collisions With Buffer Gas 68
3.7.4 Attempts at Destroying the ^{129}Xe and ^{131}Xe Polarization via NMR 69
3.7.5 Hyperfine Transition Linewidths During Frequency Shift Measurements 70
3.8 Conclusions 70

4. MEASUREMENTS OF FROZEN ^{129}XE T_1 RELAXATION 73

4.1 Introduction 73
4.2 Apparatus 75
4.3 Method Used to Generate Xe Snow or Ice 78
4.4 Data 79
4.5 Discussion 81
4.6 Conclusions 84

5. CHARACTERIZATION OF ENGINEERED CAVITIES IN PANCREATIC TRYPSIN INHIBITOR BY NMR-DETECTED XE BINDING 85

5.1 Introduction 85
5.2 Hyperpolarized ^{129}Xe NMR 88
5.2.1 Overview of Spin-Exchange Optical Pumping 88
5.2.2 ^{129}Xe Delivery System 89
5.2.3 ^{129}Xe NMR Results 89
5.2.4 Interpreting the ^{129}Xe Chemical Shift as a Function of Protein Molarity 90
5.2.5 Analysis of ^{129}Xe NMR Data 94
5.3 ^{1}H-^{15}N HSQC Under Varying Molarity of Dissolved Xe 94
5.4 Discussion of Results 97
5.5 Acknowledgements 100

APPENDICES

A. CONSERVATION OF THE SPECTRAL CENTER OF MASS 101

B. NUMERIC INTEGRATION OF A SPHERICAL DISTRIBUTION OF DIPOLES **103**

C. CELL FABRICATION PROCESS **107**

D. HYPERFINE SUBLEVEL TRANSITIONS AT LOW FIELD **110**

E. EQUIPMENT AND ELECTRONICS USED TO MEASURE ^{87}RB EPR FREQUENCY **112**

F. PDB ENTRIES USED FOR CAST CALCULATIONS **117**

LIST OF FIGURES

1.1 Basic concept of depopulation optical pumping in an alkali vapor with zero nuclear spin. . . . 4

1.2 ^{87}Rb ground and first excited state hyperfine energy levels at 30 G. . . . 5

1.3 Schematic of how a pulsed NMR experiment works. . . . 12

2.1 Experiment concept to measure $(\kappa_0)_{\mathrm{RbXe}}$ without the need to measured the Rb polarization or density. . . . 18

2.2 Photograph of the 10 mm NMR probe and Cell 155B used in the measurement of $(\kappa_0)_{\mathrm{RbXe}}$. . . . 19

2.3 Photograph of the 35 mm NMR probe used in the measurement of $(\kappa_0)_{\mathrm{RbXe}}$. . 20

2.4 795 nm Optical pumping laser and associated optical in front of superconducting magnet. . . . 21

2.5 Representative ^{129}Xe and ^{3}He FIDs acquired with the Rb in the high and low energy states. . . . 22

2.6 Fourier transforms of ^{129}Xe and ^{3}He FIDs acquired with the Rb in the high and low energy states. . . . 23

2.7 Typical ^{3}He and ^{129}Xe raw spectra from cell 155B acquired under steady-state SEOP conditions. . . . 24

2.8 Enhancement factor $(\kappa_0)_{\mathrm{RbXe}}$ plotted vs. temperature. . . . 28

2.9 CPMG decay acquired on cell 150A at 170°C to measure the ^{129}Xe diffusion coefficient. . . . 30

2.10 Simulated NMR spectra with two distinct resonant frequencies and varying exchange rates. . . . 32

2.11 ^{129}Xe 1D image to verify the ^{129}Xe magnetization is homogeneous. . . . 35

2.12 Demonstration of the ^{129}Xe spectrum dependence on the pump laser frequency. 37

2.13 Numerical integration of the through space dipole field for a sphere with different magnetization distributions verifying the through space dipole field does not appreciably affect the ^{3}He frequency shift. . . . 39

2.14 Enhancement factor $(\kappa_0)_{\mathrm{RbXe}}$ plotted vs. temperature for high-[Xe] cells. . . . 40

3.1 Schematic and photograph of the Utah flow-through polarizer. . . . 46

3.2 ^{87}Rb $5S_{1/2}$ hyperfine structure as a function of field from 0 to 30 G. . . . 48

3.3 Overview of the electronics used to measure a ^{87}Rb hyperfine transition frequency. . . . 55

3.4 Photograph of the inside of the oven on the polarizer where the RF coils (F) excite the ^{87}Rband are probed with a weak transverse D_2 laser. 56

3.5 ^{87}Rb hyperfine sublevel transition spectra acquired on an oscilloscope using the high frequency electronics and the VCO set to sweep frequency. 58

3.6 Circuit design to regulate the current through an inductive load powered by a DC power supply in voltage control mode. 60

3.7 ^{87}Rb $\langle F = 2, \bar{m} = 3/2\rangle$ hyperfine transition frequency as a function of time demonstrating the stability of the magnetic field. 61

3.8 ^{87}Rb hyperfine sublevel transition frequency as a function of time when cycling Xe into and out of the gas stream. 63

3.9 Plot of the additional effective magnetic field from the AC-Stark effect. 66

3.10 Plot of the ^{87}Rb $\langle F = 2, \bar{m} = -3/2\rangle$ hyperfine sublevel transition frequency as a function of time while changing the pump laser characteristics. 67

3.11 ^{87}Rb hyperfine sublevel transition spectra under different pump laser powers and Xe gas densities. 71

4.1 Schematic of the Pyrex condenser/cryostat used to measured frozen ^{129}Xe T_1 relaxation times. 76

4.2 Photograph of the cryostat/condenser used in the ^{129}Xe T_1 measurements. . . . 77

4.3 ^{129}Xe NMR spectra acquired during the transition of the Xe sample from accumulated snow, to liquid, and then to ice. 80

4.4 ^{129}Xe FIDs acquired during the transition from accumulated snow, to liquid, and then to ice. 81

4.5 ^{129}Xe T_1 decay measurements demonstrating the difference between Xe frozen as snow or ice. 82

5.1 Structure of wild-type BPTI and three-cavity forming variants. 86

5.2 Schematic of complete system to deliver hyperpolarized ^{129}Xe to a protein solution. 90

5.3 ^{129}Xe NMR spectra of hyperpolarized Xe in 25 mM phosphate buffer with different concentrations of wild-type BPTI. 91

5.4 ^{129}Xe chemical shift vs protein concentration. 92

5.5 ^{1}H and ^{15}N amide chemical shift changes due to the Y23A substitution and binding of Xe to Y23A BPTI. 96

5.6 ^{1}H-^{15}N chemical shift changes due to Xe binding to Y23A BPTI mapped onto the protein crystal structure. 97

5.7 Binding isotherms for Xe binding to Y23A BPTI. 98

C.1 Schematic of gas handling system used to clean and to fill cells with various gas mixtures. 108

E.1 Photograph of most of the electronic equipment used to monitor the ^{87}Rb frequency. 115
E.2 Control circuit used to condition the lock-in amplifier output before being fed to the VCO. 116

LIST OF TABLES

1.1 Table of typical parameters that can be changed in SEOP experiments and some of the effects they may have inside an optical pumping cell. 9

2.1 Summary of cell contents used in this experiment. All cells are sealed, uncoated Pyrex spheres with inner diameters of ∼7 millimeters. Quoted pressures are referenced to 20 °C and the Xe pressure is subject to ∼ 50% uncertainty due to the filling procedure. Cells 155A-C are referred to as low-[Xe] cells and Cell 150A-C are referred to as high-[Xe] cells. 17

2.2 Sample frequency shift data after processing described in Section 2.5. $\bar{x}$ is the average, and $\sigma_{\bar{x}}$ is the standard deviation of the mean. The error in $(\kappa_0)_{\mathrm{RbXe}}$ is the statistical error of each nucleus added in quadrature. There is an error associated with $(\kappa_0)_{\mathrm{RbHe}}$. However, this has been added to the final result and not to the individual values. For every point in Figure 2.8, a similar set of data was acquired. 27

2.3 Summary of cell contents and $(\kappa_0)_{\mathrm{RbXe}}$ results. $(\kappa_0)_{\mathrm{RbXe}}$ is computed for each of the low-[Xe] cells from the weighted average of that cell's data; we have excluded the high-[Xe] cells because of their anomalous behavior at high temperature (see Section 2.5.6) 27

3.1 Components of the EPR frequency counting apparatus. 57

4.1 T_1 results of ^{129}Xe in natural abundance Xe at 77 K. Each measurement is a completely new accumulation of frozen Xe from the polarizer. The stated errors are from least squares fits. The repeatability of these measurements is unprecedented, and the difference between ice and snow, while not understood at this point, is a possible explanation for variability in all previously published results. 83

5.1 Table of ^{129}Xe NMR chemical shift results from data shown in Figure 5.4 95

5.2 Table comparing ^{129}Xe binding sites in this work to prior publications 99

ACKNOWLEDGMENTS

First and foremost, I need to thank my family for their love and support during graduate school. My mother and father have unconditionally supported me throughout my life whether I was pursuing my dreams in the pool or in the classroom. Without these two amazing people in my life, nothing I have accomplished would have come to pass. My sister was and remains a constant, friendly reminder that I really am an idiot and I am grateful to have her humbling presence. My cousin's frequent calls always made me laugh, even when nothing was working in the lab. I hope I have convinced my family that I did not get my doctorate in telemark skiing.

I want to thank Monica Allen, my girlfriend of four years, for standing by my side as I struggled through several experiments and writing this thesis. Her passion for life constantly reminds me that I don't have to spend 12 hours a day in the lab to be successful. I am very fortunate to have her love, and my time in Utah would not have been the same without her.

While I was spending long days in the lab, there were a few people I came to rely on very frequently. I thank Ed for his patience with my constant questioning and helping me with many of my machining projects. Harold was always around with a good idea or information on the right people to call to get things working when the South Physics building was going through its daily death throes. The front office made my life much easier by helping me navigate the plethora of paperwork over the years.

The last set of acknowledgements is dedicated to the Saam research group. I want to thank Geoff Schrank for helping me get my feet wet with my first project. Eric Sorte provided invaluable help during the $(\kappa_0)_{\mathrm{RbXe}}$ experiment, and I have many fond memories of rock climbing with him in Big Cottonwood Canyon. Mark Limes was a constant source of impossible questions and I couldn't ask for a better labmate.

Lastly, I thank my advisor, Brian Saam, for giving me the chance to join and excel in his research group. I have never met anyone who loves teaching more than Brian. His excitement for experimental atomic physics is truly infectious. I hope I have learned his lessons well, and I promise to not "make him look bad" in whatever I do in the future.

CHAPTER 1

INTRODUCTION

Spin-Exchange Optical Pumping (SEOP) and Magnetic Resonance (MR) will be briefly discussed in this introduction in order to provide the background for understanding the experiments presented in this dissertation.

1.1 Spin-Exchange Optical Pumping

SEOP is a two-step process in which an alkali vapor is spin polarized by optically pumping with circularly polarized light at a resonant atomic transition. The alkali spin polarization is then transfered to noble-gas nuclei through spin-exchange collisions. This process can produce noble-gas samples with nuclear spin polarizations approaching 100% under certain conditions and has been given the catchy name "hyperpolarized noble-gas via SEOP."

1.1.1 Brief History of Optical Pumping and Spin Exchange

The history of optical pumping, the connection with the Overhauser effect, and the discovery of spin-exchange between alkali metals and noble-gas nuclei is an entire book in itself. The rich history of the field and the people involved cannot be adequately covered in one paragraph; nevertheless, a brief summary follows.

In 1952, A. Kastler published a paper in which he pointed out that absorption and scattering of resonant light leads to large population imbalances in atomic spin ground states of alkali atoms [14]. At almost the same time, A. Overhauser predicted that saturation of the electron resonance in metals will create an enhanced nuclear polarization on order of the ratio between the electron and nuclear gyromagnetic ratios [50]. The enhancement arises when the electrons attempt to relax back to thermal equilibrium and spin-flip nuclei. In 1956, the Overhauser effect was first observed in Lithium powder by C. Slichter and T. Carver [15]. T. Carver then moved to Princeton where the first attempts were made to realize the Overhauser effect in alkali–noble-gas mixtures. However, instead of saturating the alkali spin polarization, the alkali vapor was polarized by optical pumping. To further

this work, the first female post-doc at Princeton, M. Bouchiat, was hired to build the apparatus to polarize ^{3}He using SEOP. This was ultimately successful and they polarized ^{3}He to ∼0.01% (4 orders of magnitude over the thermal polarization) [12]. M. Bouchiat then began work on measuring the relaxation rate of Rb vapor in the presence of other noble gases. She discovered the existence of Rb-Xe van der Waals molecules and published two seminal papers on Rb-Xe molecular formation around 1970 [11, 10]. These papers were crucial to the theoretical work published by W. Happer in 1984 [31] that laid the foundation for almost all the work in SEOP that followed. W. Happer, who took over T. Carver's lab, was Brian Saam's doctoral advisor at Princeton University.

1.1.2 Optical Pumping of Rb

An excellent description of the optical pumping and subsequent spin-exchange process can be found in references [30] and [72]; only the highlights will be recounted here. When resonant light is absorbed by an alkali atom, an electron will be moved into an excited state. From the excited state, the electron can relax back to different spin ground-states with probabilities given by matrix elements of the dipole operator [66]. If the resonant light is circularly polarized, then only a subset of the spin ground-states will be excited and a spin population will accumulate in the other ground states as the electrons relax. This is known as "depopulation pumping."

In practice, a typical optical pumping experiment is as follows. A Pyrex cell is filled with a few milligrams of Rb metal and some additional buffer gases (typically He, N_2, and Xe). The cell is heated to 100-200 °C which drives the Rb into vapor according to [38]

$$[\mathrm{Rb}] = \left(\frac{1}{T}10^{26.41+4132/T}\right) \tag{1.1}$$

where T is the temperature in Kelvin, and the numbers have been chosen to make [Rb] have units of atoms per cubic centimeter. This Rb vapor is then irradiated with circularly polarized D_1 light ($\sigma+$ or $\sigma-$). D_1 light excites the valence electron from the $5S_{1/2}$ to the $5P_{1/2}$ state and the circular polarization, due to selection rules, forces the quantum number defining the spin state of the Rb atom to change by ±1 depending on the helicity of light polarization. While in the excited state the Rb atoms collide with buffer gas and, only very occasionally, other Rb atoms. These collisions rapidly mix and equilibrate the excited state populations. At this point, if the Rb atoms are allowed to relax radiatively, an unpolarized D_1 photon will be emitted that can scatter several times. Repeated scattering of unpolarized light in the Rb vapor will ruin the ground state population imbalance because unpolarized

light excites out of all spin-ground states with equal probability. The process of repeated scattering is known as radiation trapping. To avoid radiation trapping, 50-200 Torr of nitrogen is added to the buffer gas mixture. The N_2 molecule has rotational-vibrational states equivalent to the Rb D_1 energy and can carry away the energy of an excited Rb atom allowing it to relax nonradiatively back to the ground state. This optical pumping process is then continued, and eventually a steady state balance is reached between the optical pumping rate and various relaxation rates. In typical optical pumping experiments, the Rb polarization can reach nearly 100% under certain conditions. Figure 1.1 illustrates the optical pumping process for a group of fictitious alkali atom with no nuclear spin ($I = 0$) and zero magnetic field.

Many current optical pumping experiments use Rb for several practical reasons. First, The D_1 and D_2 resonances are far enough apart that, while pumping with D_1 light from typical diode lasers, very little optical pumping power is at the D_2 transition frequency. Pumping with D_2 light is very inefficient because both spin-ground states shown in Figure 1.1 can be pumped out of with either $\sigma+$ or $\sigma-$ light. Second, in typical optical pumping cells the Rb vapor pressure at easily attainable laboratory temperatures (100-200 °C) is hundreds of optical depths thick for D_1 light. Lastly, the D_1 transition is very close to inexpensive high-powered (30-1000 Watt) solid-state laser-diode arrays.

While the description above is sufficient to understand most aspects of optical pumping, the description is a simplified semi-accurate physical picture. In reality, alkali atoms have nuclear spin and almost all optical pumping is done in a nonzero magnetic field. While, optical pumping can be done in zero magnetic field where the quantization axis and direction will be defined by the direction and helicity of pumping light, respectively, any small fluctuating field in the sample will quickly reorient the spins and possibly ruin the ground state population imbalance. To avoid this, the optical pumping setups used in this dissertation use a minimum magnetic field of ∼30 gauss (G) dominates any stray fields in the lab. All alkali atoms have nuclear spin and a magnetic hyperfine interaction $\mathbf{I} \cdot \mathbf{S}$ between the nucleus spin $\mathbf{I}$ and the electron spin $\mathbf{S}$ (see Section 3.3). A 30 G magnetic field will resolve the hyperfine structure and can potentially complicate the optical pumping.

If the optical pumping laser has a narrow spectral width compared to the zero field hyperfine splitting and the Rb D_1 resonance is not broadened in any way, then selectively pumping out of only a few hyperfine states is possible. Selectively pumping out of only a few ground states will decrease the optical pumping efficiency as the atomic spin F can

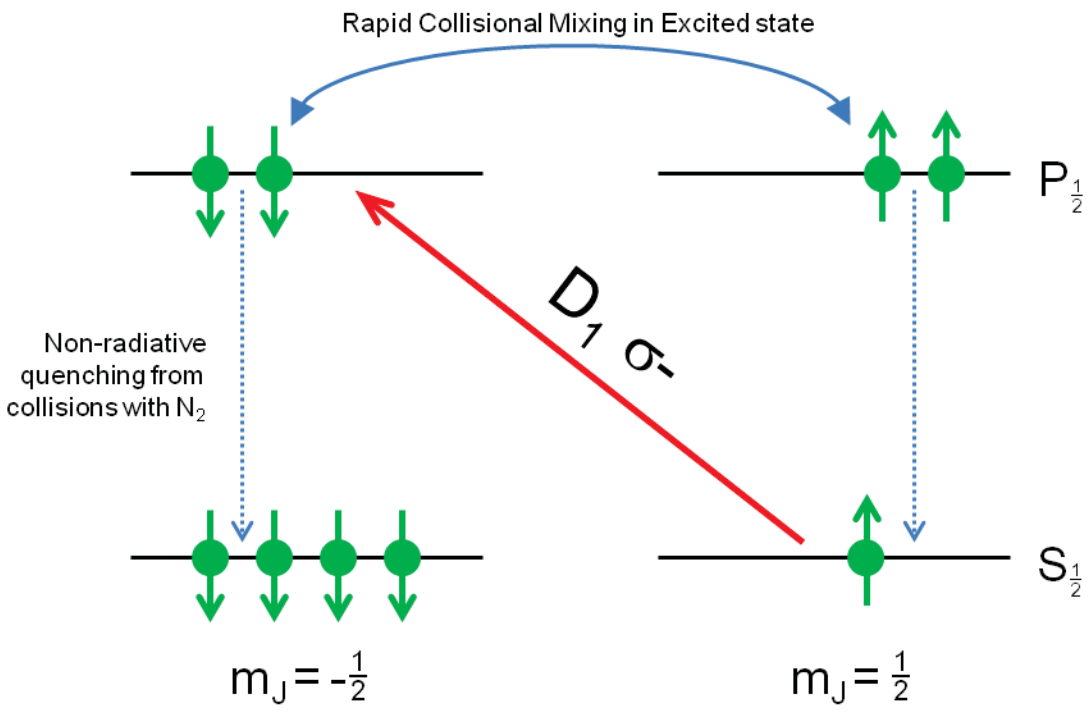

Figure 1.1. Basic concept of depopulation optical pumping in an alkali vapor with zero nuclear spin. Each arrow represents the electron spin of a single alkali atom. The diagram is split vertically in energy by the D_1 transition (7947 Å for Rb) and horizontally by the quantum number m_J of the total angular momentum $\mathbf{J} = \mathbf{L} + \mathbf{S}$. The alkali vapor is excited by D_1, $\sigma-$ light that can only pump out of one of the $m_J = +1/2$ states due to the selection rule imparted by the helicity. The m_J states rapidly mix and equilibrate in the excited state due to collisions with buffer gas and other alkali atoms. The vapor can then relax nonradiatively when colliding with N_2 molecules which have rotational-vibrational states with energies close to the D_1 transition. In the picture shown, the Rb electron spins will then accumulate in the $m_J = -1/2$ state.

accumulate and distribute among states that are not the maximum or minimum spin angular momentum states ($\langle F = 2,\ m_F = \pm 2\rangle$ for ^{87}Rb). Figure 1.2 illustrates this point by showing the atomic levels including hyperfine coupling that can be excited by $\sigma-$ light (the values for ^{87}Rb in Figure 1.2 are from reference [66]). To ensure that optical excitation has an equal probability from all possible spin-ground states, one or more atmospheres of buffer gas is added to the optical cell which broadens the Rb D_1 transition by ~20 GHz/amagat [55] (an amagat is the density of an ideal gas at standard temperature and pressure). In addition, solid-state diode lasers typically have ~100 GHz widths with in-lab after-market narrowing. With lasers this broad, covering the hyperfine structure is no longer a concern. The major concern becomes broadening the D_1 transition enough with buffer gas to ensure

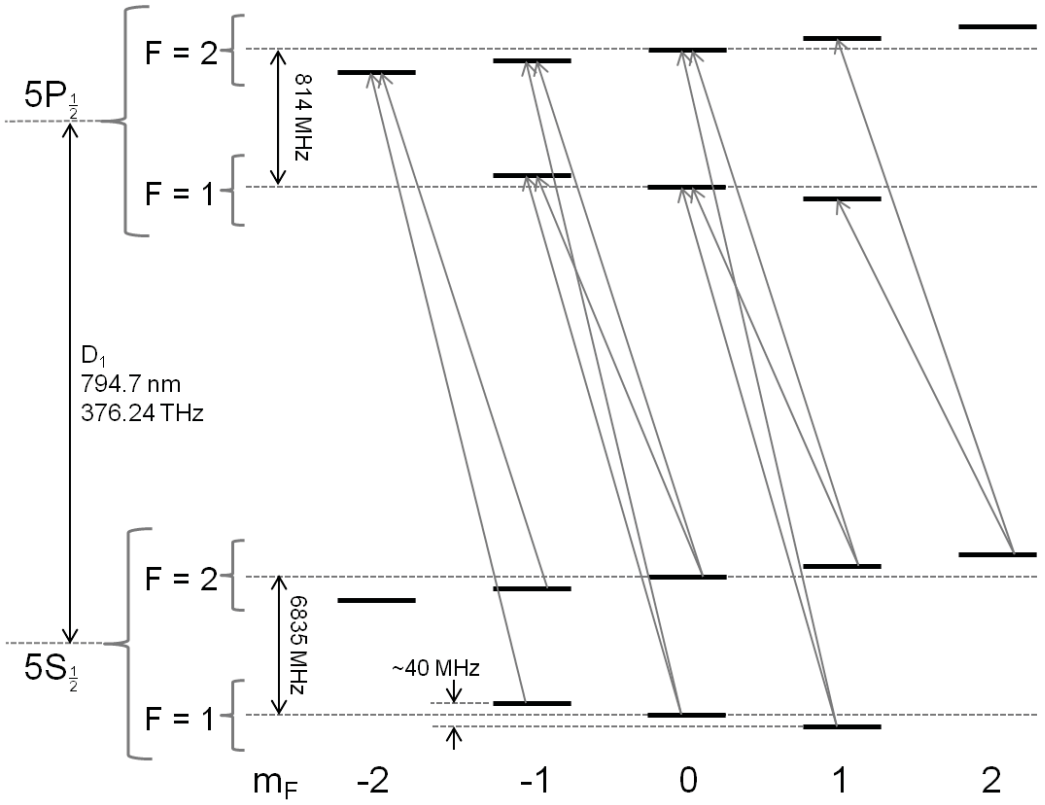

Figure 1.2. ^{87}Rb ground and first excited state hyperfine energy levels at 30 G (not to scale). The arrows represent the allowed transitions under irradiation of D_1, $\sigma-$ light. The atomic states are denoted by $\mathbf{F} = \mathbf{I} + \mathbf{J}$ with azimuthal quantum number m_F. The ground state hyperfine splitting at zero magnetic field is 6835 MHz, and hyperfine sublevel transitions are $\Delta F = 0$, $\Delta m_F \pm 1$. With a sufficiently narrow laser selecting only a few of the allowed transitions is possible which will permit the atomic spin F to accumulate in ground states that are not maximum or minimum spin angular momentum states. This is avoided in two ways: first, spectrally narrowed solid-state diode lasers are typically 100 GHz FWHM which is much broader than the zero-field hyperfine splitting of 6.8 GHz; second, the presence of buffer gas broadens the Rb D_1 resonance by about 20 GHz/amagat.

most of the laser light is used to optically pump Rb and not heat the oven wall behind the cell.

1.1.3 Rb–Noble-Gas Spin Exchange

The depopulation optical pumping process described in Section 1.1.2 can highly polarize a Rb vapor. However, the Rb has several relaxation pathways back to thermal equilibrium and has many mechanisms to do so. These mechanisms include but are not limited to collisions with the container walls, diffusion through magnetic field gradients, radiation trapping, spin-rotation interaction, and spin-exchange [30]. The mechanism that dominates

all others at low magnetic fields is the spin-rotation interaction which occurs when a Rb atom forms a molecule with another atom, and the Rb electron spin **S** precesses about the rotational angular momentum of the molecule **N**. Another possible relaxation pathway is spin-exchange. Spin-exchange conserves the total internal spin of the colliding atoms and can occur between two Rb atoms or Rb and a noble gas atom. Spin exchange between Rb atoms does not change the overall Rb polarization but rather aids in pushing the entire Rb vapor towards a single spin-temperature distribution. Spin exchange between a Rb electron and a noble gas nucleus can randomize the Rb electron spin but it also, as Overhauser predicted, spin-polarizes the noble gas nuclei.

The Rb–noble-gas collisional Hamiltonian consistent with known relaxation mechanisms is [2]

$$\mathcal{H} = A\mathbf{I}\cdot\mathbf{S} + \gamma(R)\mathbf{N}\cdot\mathbf{S} + \alpha(R)\mathbf{K}\cdot\mathbf{S} + g_{\mathrm{s}}\mu_{\mathrm{B}}S_zB_z - \frac{\mu_{\mathrm{I}}}{I}I_zB_z \tag{1.2}$$

where $A\mathbf{I}\cdot\mathbf{S}$ is the coupling between the alkali nuclear spin **I** and the alkali electron spin **S** which gives rise to the akali hyperfine structure; $g_{\mathrm{s}}\mu_{\mathrm{B}}S_zB_z$ and $-\frac{\mu_{\mathrm{I}}}{I}I_zB_z$ are the magnetic dipole couplings of the alkali electron and nuclear moments to the applied magnetic field (taken in the z-direction); $\gamma(R)\mathbf{N}\cdot\mathbf{S}$ is the spin-rotation interaction between the alkali electron spin **S** and the relative angular momentum **N** of the colliding atoms; and $\alpha(R)\mathbf{K}\cdot\mathbf{S}$ is the magnetic dipole coupling between the noble-gas nucleus and the alkali electron. Both the spin-rotation coefficient $\gamma(R)$ and the spin-exchange coefficient $\alpha(R)$ depend on the interatomic distance R between the alkali and noble gas atom. This Hamiltonian has been studied extensively with both perturbative and numerical methods in references [31] and [2]. The details will not be discussed here. However, the qualitative features of the collisional process will be discussed and are essential to understand the experiments presented in this dissertation.

When Rb atoms collide with a buffer gas, two types of collisions are possible: binary and molecular. Binary collisions typically last for a picosecond and can be pictured as two atoms simply "flying by" each other. Whereas, molecular collisions can last from 1-10 nanoseconds depending on gas pressure and occur when a van der Waals molecule is formed between a Rb atom and a noble gas atom. The difference in whether a collision will be molecular or binary depends on the van der Waals potential attracting the two atoms and whether a third body is present. Rb-He van der Waals potentials have no attractive well and therefore the collisions are always binary. In addition to having a short interaction time, a He atom has a low polarizability compared to the other noble gases, and the Rb

electron cannot penetrate the He electron cloud easily to couple to the He nucleus, making the $\alpha(R)\mathbf{K}\cdot\mathbf{S}$ coupling very weak. This weak coupling is reflected experimentally by Rb-^{3}He spin-exchange times on the order of tens of hours. Rb-Xe, on the other hand, has an attractive potential well where the well depth is about one third of kT at typical optical pumping temperatures. Thus even with an attractive potential the vast majority of Rb-Xe collisions will be binary unless a third body is present. The third body can carry away some of the kinetic energy allowing a stable Rb-Xe molecule to form. Molecular formation increases the Rb-Xe interaction time by several orders of magnitude over binary collisions and therefore makes Rb spin-destruction much more rapid. However, Xe is highly polarizable, and the Rb electron can easily penetrate the Xe electron cloud and couple to the nucleus resulting in a much stronger spin-exchange coupling. Numerical calculations of the Rb valence electron in the presence of Xe show that the probability of the electron to be at the Xe nucleus during a collision can be as much as 50%. In contrast to ^{3}He, this strong coupling results in typical Rb-^{129}Xe spin exchange times on the order of minutes. See also references [11, 31, 72, 2].

The term responsible for spin-exchange, $\alpha(R)\mathbf{K}\cdot\mathbf{S}$, is a magnetic dipole interaction that has both a through-space interaction that depends on direction and a Fermi-contact interaction that arises because of the wave function overlap of the Rb electron and the noble gas nucleus. The through-space interaction can potentially contribute a 2% effect during spin exchange and is generally ignored [31], whereas the wave function overlap of the Rb electron and noble-gas nucleus can produce a much stronger effect and is the basis for pursuing the measurements presented in Chapters 2 and 3. Averaged over many collisions, both the alkali electron, and noble-gas nucleus will experience a small nonzero magnetic field if the colliding spins are polarized. This additional magnetic field will shift any Zeeman energies in the noble-gas and alkali atom, and can be experimentally detected by a shift in the Larmor frequency that will be proportional to the polarization of the opposing species. Chapter 2 uses the change in the nuclear magnetic resonance (NMR) frequency of ^{129}Xe and ^{3}He due to collisions with polarized Rb atoms to calibrate the size of the shift for Rb-^{129}Xe collisions [46]. Chapter 3 describes the experiment in which the frequency shift of the ^{87}Rb Zeeman hyperfine sublevels were used to make the first attempts to date at measuring ^{129}Xe polarization inside an optical pumping cell using the frequency shift of the Rb Larmor frequency.

1.1.4 Practical SEOP

The previous sections provided an overview of the most relevant physics in SEOP. However, successfully connecting these concepts to experimental conditions in a lab can be challenging. Table 1.1 is a list of typical operating parameters that can be changed, the effect they will have on the spins in the optical pumping cell, and the associated observables in the lab.

1.2 Magnetic Resonance

Every experiment in this dissertation uses the well known phenomena of magnetic resonance to probe both atomic and molecular interactions. References [64] and [1] have excellent descriptions of many aspects of magnetic resonance as well as detailed mathematical formalisms. While mathematical formalisms are useful for understanding details, a simplified physical picture will be discussed here to give the reader a picture to keep in mind when viewing the data and results of the various experiments.

1.2.1 Spins in a Magnetic field

For the purposes of this discussion, spin is an arrow and the head of the arrow denotes either the north or south end of a tiny bar magnet or magnetic moment. Without a magnetic field a spin has no preferred direction and all spin states are degenerate. The application of a magnetic field $\mathbf{B_0}$ lifts the degeneracy and splits the spin-up and spin-down states (known as the Zeeman effect) by an energy $E = \hbar\gamma \mathrm{B}_0$. γ is the "gyromagnetic ratio" which sets the scale for the size of the Zeeman energy splitting and has units of $\frac{1}{(\mathrm{sec})(\mathrm{G})}$. Electrons and many nuclei have intrinsic spin J that is related to their magnetic moments by $\vec{\mu} = \gamma\hbar\mathbf{J}$. The frequency $\gamma \mathrm{B}_0/(2\pi)$ is called the Larmor frequency. For reference it is 24.5 MHz for ^{129}Xe in a 20,000 G magnetic field and $\sim$19 MHz for a ^{87}Rb hyperfine sublevel transitions in a 30 G magnetic field.

The previous paragraph explains in very basic terms how the energies of an isolated single spin behaves in a magnetic field. Practically, for a sample consisting of a many-spin system where the spins can interact and exchange energy, two macroscopic observables are always relevant. The thermal spin-polarization of the sample and the longitudinal relaxation time (T_1).

The thermal polarization of the sample is given by a Boltzmann distribution, and for spin 1/2, this is the difference in population between spin-up and spin-down normalized by the total number of spins:

Table 1.1. Table of typical parameters that can be changed in SEOP experiments and some of the effects they may have inside an optical pumping cell.

SEOP parameter change	Result
Increase pumping laser power	Increases optical pumping rate Can potentially cause massive local heating in the cell Can cause Rb hyperfine frequency shifts (Section 3.7.1)
Change pumping laser tuning	Changes the absorption of light that can change the optical pumping rates and light penetration Can cause Rb hyperfine frequency shifts (Section 3.7.1)
Increase oven temperature	Increases [Rb] according to equation 1.1 Increases Rb-Rb spin-exchange and spin-destruction rates [34] Increases Rb-^{129}Xe and Rb-^{3}He spin-exchange rates [18, 17] Decreases the characteristic optical depth of the cell potentially leading to significant laser attenuation
Increase magnetic field	Decreases Rb spin-destruction from molecular formation [11] Increases the splitting between the Zeeman hyperfine sublevels in Rb (Section 3.3)
Addition of N_2 into cell	Allows Rb to relax nonradiatively (Section 1.1.2 and [30]) Broadens the Rb D_1 and D_2 absorption width [55] Aids in formation and breakup of Rb-Xe van der Waals molecules Increases Rb hyperfine splitting [47]
Addition of He into cell	Broadens Rb absorption lines [55] Aids in formation and breakup of Rb-Xe van der Waals molecules Increases the Rb hyperfine splitting [47]
Addition of Xe into cell	Dramatically increases Rb spin-destruction [48] which has the possibility of affecting laser attenuation Aids in formation and breakup of Rb-Xe van der Waals molecules Broadens Rb absorption lines [55], but typical Xe concentrations are too low to see an effect Decreases Rb hyperfine splitting [47]

$$P = \frac{N\uparrow - N\downarrow}{N\uparrow + N\downarrow} = \tanh\left(\frac{\mu \mathrm{B}_0}{kT}\right) \tag{1.3}$$

where B_0 is the magnetic field, k is the Boltzmann constant, and T is the absolute temperature of the sample. Typical thermal polarization for nuclear spins in a modest magnetic field (2 T) at room temperature is 10^{-5} to 10^{-6}. In experiments where the spins are being detected directly, the size of the signal will be proportional to the magnetization which is the product of the magnetic moment, polarization, and density of the spins. Typical gas densities are of order 10^{19} atoms per cubic centimeter (compared to 10^{22} hydrogen atoms per cubic centimeter of water) and detecting ^{129}Xe or ^{3}He nuclei through induction (see Section 1.2.2) is impossible unless the nuclear spin polarization is at least 0.01 which can lift the signal above typical electronic noise, hence the need for hyperpolarized gas. The temperature T in Equation 1.3 is generally considered to be the sample temperature, which is correct for thermally polarized samples. However, T can also be used to describe the spin polarization of the sample. For example, hyperpolarized ^{129}Xe in a glass cell at room temperature has a much lower "spin temperature".

For particles that do not have spin 1/2, the definition of "polarization" must be generalized. A sample of non-spin 1/2 particles will have a population distributed through the Zeeman states described by a Boltzmann distribution and the polarization is defined as $P = \frac{\langle \mathrm{I}_z \rangle}{\mathrm{I}}$. For example, in a Rb vapor the atomic polarization is described by $\frac{\langle \mathrm{F}_z \rangle}{\mathrm{F}}$, and the electron spin polarization is $\frac{\langle \mathrm{S}_z \rangle}{\mathrm{S}}$.

The longitudinal relaxation time T_1 is the characteristic time for a sample to relax up or down to its thermal polarization described above. This process requires local oscillating transverse magnetic fields at the Larmor frequency which will induce transitions from spin-up to spin-down and vice versa. The possible sources of energy to modulate the magnetic field and induce spin flips are very diverse. In a solid insulator, the mechanism is usually lattice vibrations from phonons; in a liquid sample it can be from spin-rotation modulated by collisions or dipole-dipole interactions with other spins; in a gas sample spin-rotation, spin-exchange, diffusion through field gradients, and wall interactions are all possible mechanisms.

1.2.2 Excitation and Detection

To induce transitions between energy levels split by the Zeeman effect, a second (RF) magnetic field $\mathbf{B_1}$ oscillating at the Larmor frequency is applied transverse to the static magnetic field $\mathbf{B_0}$. This application of RF, viewed in a reference frame rotating at the

Larmor frequency (called the rotating frame), will torque the magnetization away from the static magnetic field direction towards the transverse plane. The RF can be stopped at a time when the magnetization lies in the transverse plane and the spins will then precess about the main magnetic field $\mathbf{B_0}$ at approximately the Larmor frequency. Deviations from the exact Larmor frequency occur because the magnetic field at each point in the sample will not be identical because of dipole fields from nearby spins or magnetic field inhomogeneities. This difference in magnetic field across the sample will cause some spins to precess faster than others. The difference in precession frequencies dephases the spins resulting in a decay of the magnetization coherence in the transverse direction with a characteristic time T_2^*. This method of inducing transitions between Zeeman energy levels for a finite time to tip the spins in a sample to a specific angle then monitoring the transverse decay is referred to as pulsed MR. The duration of the RF excitation is called the pulse length, and the angle the magnetization resides at with respect to the static magnetic field is called the flip angle.

The nuclear MR (NMR) experiments in this dissertation are all done with pulsed NMR. The remainder of this section will describe pulsed NMR and how T_2^* relates to spin dynamics in a sample.

In all pulsed NMR experiments, a collection of electronics referred to as the spectrometer outputs an RF pulse with a specific frequency, shape, and duration. The pulse is amplified, and sent to an inductor that is oriented perpendicular to the main magnetic field and also contains the sample. To minimize the transmission loss between the amplifier and inductor, the inductor is capacitively coupled such that the impedance at the desired frequency matches the output impedance of the amplifier. The capacitive and inductive structure is called the probe and typically contains tunable capacitors that can change the probe impedance at specific frequencies. This impedance matching is typically narrow in frequency ($\frac{f}{\Delta f}$ is usually 50-100, where f is the resonant frequency and Δf is the FWHM) which makes the probe an excellent notch filter that is highly sensitive to induction at only the resonant frequency.

After the RF pulse ends, the magnetization will precess at the Larmor, frequency and this precessing magnetization will induce an oscillating voltage in the probe. The typical induced voltage in the probe is not much more than a few microvolts, and an NMR spectrometer essentially acts as a high-frequency, high-gain, high-fidelity lock-in amplifier to lift the signal out of the noise and demodulate it down to audio frequency. This demodulated signal, known as a free induction decay or FID, can then be outputted to an oscilloscope

or a computer. A FID is a decaying oscillation at the precession frequency in the rotating frame, which has a frequency set by the central excitation frequency, and the envelope decay is the magnetization coherence loss in the transverse direction. See Figure 1.3 for a schematic of the pulse-receive process and a sample FID from a hyperpolarized ^{3}He sample.

Since the FID is a measure of the loss of spin-coherence vs time, it can be Fourier

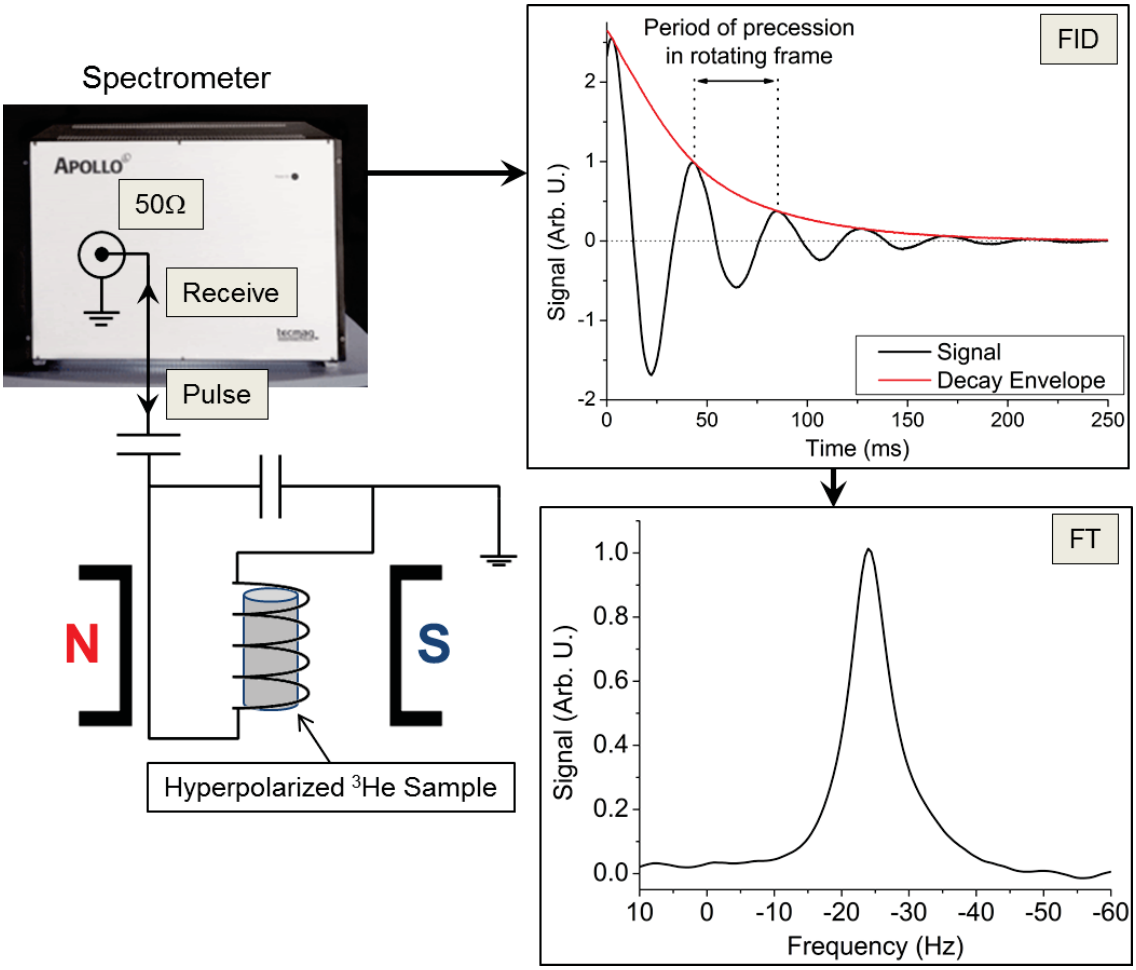

Figure 1.3. Simplified NMR experiment. The spectrometer provides an RF pulse that is amplified and transmitted to the probe which is impedance matched to spectrometer and frequency tuned to the the Larmor frequency of the spins in the sample. After the RF pulse finishes the spins precess in the sample. This precession is picked up by the same inductor that delivered the RF and is transmitted back to the spectrometer to be amplified and mixed down to audio frequency. The spectrometer outputs the free induction decay (FID) to an oscilloscope or computer (upper right). The FID shown is from a hyperpolarized ^{3}He sample in a 2 T magnetic field. This FID can be Fourier transformed (FT) to give a frequency spectrum of the resonant frequencies in the sample. In this case the FT results in a single resonance frequency with a width that is determined by magnetic field inhomogeneities.

transformed to generate the spectrum of the frequencies required to generate the coherence loss. R. Norberg and I. Lowe proved that that a Fourier transform of the FID contains all of the same frequency information as monitoring the absorption of continuous-wave (CW) RF by a sample as spins are brought into and out of resonance by slowly sweeping the magnetic field. This discovery revolutionized the fields of high resolution NMR spectroscopy and magnetic resonance imaging as well as opened the doors to complex structural and molecular dynamic information about molecules in solution using multidimensional Fourier transform spectroscopy.

The Fourier transform of an FID is a frequency spectrum comprised of one or more resonance peaks with associated widths. The width of the resonances are inversely related to the characteristic decay time T_2^* of the FID envelope which can be affected by many physical processes. A few of these processes will be mentioned here and then discussed in more detail in the relevant chapters.

T_2^* is generally expressed as

$$\frac{1}{T_2^*} = \frac{1}{T_2} + \Gamma_i, \tag{1.4}$$

where T_2^* is the experimental decay constant, T_2 is the decay time from microscopic interactions in the sample, and Γ_i is the dephasing caused by inhomogeneity in the main magnetic field $\mathbf{B_0}$. In all experiments presented here, T_2^* is minimized by a process called shimming in which the homogeneity of the main magnetic field $\mathbf{B_0}$ is adjusted by adding small additional fields in different directions. If $T_2^* \rightarrow T_2$, linewidths have physical significance relevant to the spin dynamics in the sample. The analysis in Chapter 2 used ^{3}He and ^{129}Xe NMR spectra that were field-inhomogeneity and chemical-exchange broadened respectively. The frequency shift measurements in Chapter 3 followed the frequency of a ^{87}Rb hyperfine sublevel transition frequency with linewidths determined by optical pumping and collisional relaxation rates. In Chapter 4, frozen ^{129}Xe T_1 was measured using the decay of dipolar-broadened resonance lines. Lastly, in Chapter 5, one aspect of the protein characterization used the frequency shift of a dissolved ^{129}Xe resonance that was broadened by inhomogeneity.

CHAPTER 2

MEASUREMENT OF THE FREQUENCY SHIFT ENHANCEMENT FACTOR DURING RB-XE COLLISIONS

In 1978 while doing measurements to detect nuclear ^{129}Xe polarization via Rb electron paramagnetic resonance (EPR), B. C. Grover noticed that the magnetic field induced by the noble-gas polarization experienced by the Rb atoms was two orders of magnitude larger than what was classically predicted [29]. He immediately hypothesized that this was due to a strong Fermi-contact interaction during binary collisions; while we now understand that Xe and Rb undergo both binary and molecular collisions, his explanation of the effect was correct. This enhancement is characterized by a dimensionless factor κ, and we have successfully measured it to be [46]

$$(\kappa_0)_{\mathrm{RbXe}} = 493 \pm 31 \ . \tag{2.1}$$

This chapter is devoted to the motivation, background, experimental details, and data analysis associated with this measurement.

2.1 Introduction

Much of the physics and theory of SEOP has been worked out in great detail [31, 2], and is well understood. However, the problem of optimizing SEOP equipment to produce large volumes of highly polarized ^{129}Xe efficiently remains open. Many current methods exists to characterize an optical pumping apparatus [61]. However, the ability to measure the ^{129}Xe polarization inside an optical pumping cell (without a thermal NMR reference) while actively pumping has not been realized. This measurement of $(\kappa_0)_{\mathrm{RbXe}}$ provides the crucial missing link to make measuring the ^{129}Xe polarization possible.

As discussed in Section 1.1.3, the Fermi-contact hyperfine interaction $\alpha\mathbf{K}\cdot\mathbf{S}$ between the noble-gas nuclear spin $\mathbf{K}$ and the alkali-metal electron spin $\mathbf{S}$ is responsible for alkali–noble-gas spin-exchange. In addition, if the Rb vapor and the noble-gas are highly polarized,

then a Larmor frequency shift (relative to zero polarization) will occur in the alkali EPR frequency and the noble-gas NMR frequency. This shift in frequency is due to repeated collisions with spins aligned in the same direction which will, on average, provide a small additional non-zero magnetic field. The shift in the nuclear Larmor frequency due to the hyperfine interaction was first observed by W. D. Knight while doing an NMR experiment on powdered ^{63}Cu [39]. However, the observed effect in ^{63}Cu was due to the intra-atomic hyperfine interaction between Cu conduction electrons and Cu nuclei. In this measurement the hyperfine interaction is interatomic between polarized Rb electrons and noble-gas nuclei.

The small collisionally averaged additional field seen by the noble gas and the resulting frequency shift has been calculated in spherical geometry to be [59]

$$\Delta |\nu_X| = -\frac{1}{h}\frac{|\mu_K|}{K}\frac{8\pi}{3}\mu_B g_S \kappa_{XA}[A]\langle S_z\rangle, \tag{2.2}$$

where X is the noble gas species, A is the alkali metal species, h is Planck's constant, μ_K is the nuclear magnetic moment, μ_B is the Bohr magneton, $g_S \approx 2$ is the Landé factor, $[A]$ is the alkali-metal number density, and $\langle S_z\rangle$ is the volume-averaged expectation value of the z-component of the alkali-metal electron spin (in units of $\hbar$). $\kappa_{XA} = (\epsilon_{XA} - 1)\kappa_1 + \kappa_0$ is the complete enhancement factor which contains both molecular (κ_1) and binary (κ_0) collision contributions and a supression factor ϵ_{XA} that depends on the gas pressure [59]. Our measurement was done in the regime where the enhancement is solely due to κ_0, and a complete discussion of neglecting the molecular contribution is given in Section 2.5.7. An equation analogous to 2.2 for the EPR shift at low magnetic field where the alkali hyperfine splitting is much greater than the Zeeman energy is given by [59]

$$\Delta |\nu_A| = \frac{1}{h}\frac{\mu_B |g_s|}{(2I+1)}\frac{8\pi}{3}\frac{\mu_K}{K}\kappa_{AX}[X]\langle K_z\rangle. \tag{2.3}$$

where I is the alkali metal nuclear spin, $[X]$ is the noble gas number density, and $\langle K_z\rangle$ is the ensemble averaged expectation value of the nuclear spin in units of $\hbar$.

An accurate measurement of κ_0 can provide important constraints on the problem of calculating Rb valence electron wavefunctions during a van der Waals collision or computing the van der Waals potential numerically. However, the most immediate application of this measurement is *in situ* noble gas polarimetry. Equation 2.3 is proportional only to known fundamental constants, κ_0, and the noble gas magnetization. Therefore with knowledge of κ_0, the noble gas number density, and an accurate measurement of the Rb EPR frequency the polarization of the noble gas can be deduced. Using the classical through-space dipole

field (non-zero for all geometries not a sphere) of a cylinder, a 1.5% measurement of $(\kappa_0)_{\mathrm{RbHe}}$ was done [8, 54] and $(\kappa_0)_{\mathrm{RbHe}}$ has been used to measure ^{3}He polarization in neutron spin structure experiments [65].

All ^{129}Xe polarization measurements prior to this dissertation have been done by referencing a thermal NMR signal and suffer from several shortcomings. The measurements rely on a comparison of the ^{129}Xe NMR signal intensity to a thermally polarized sample with a known spin density that fills the exact same volume as the ^{129}Xe sample. If the hyperpolarized (HP) ^{129}Xe signal is compared to a thermally polarized ^{1}H sample, the different gyromagnetic ratios requires electronics that respond identically to a frequencies that are different by a factor of four or the static magnetic field must be adjustable. If the HP ^{129}Xe signal is compared to thermally polarized ^{129}Xe, then the thermal sample must be filled with $\sim$10 atmospheres to get any usable signal. Guaranteeing the thermal sample occupies the same volume as the hyperpolarized sample can indeed become a dangerous endeavor as any nonspherical geometry is very susceptible to explosions. Furthermore, thermal NMR polarimetry must be done at relatively high-fields where the thermal polarization is high enough to induce a measurable voltage in the probe. Optical pumping experiments are generally done in low fields ($\sim$30 G) for practical reasons and moving the polarized gas to a higher field and then measuring the polarization will provide a reasonable estimate of the noble gas polarization, but will not provide time resolved information regarding the dynamics inside of the optically pumping cell.

$(\kappa_0)_{\mathrm{RbHe}}$ has been measured before to be $(\kappa_0)_{\mathrm{RbHe}} = 4.52 + 0.00934T$ [54] (where T is temp in Celcius) and $(\kappa_0)_{\mathrm{RbXe}}$ has been measured to be 650 ± 350 [59] respectively. The measurement of $(\kappa_0)_{\mathrm{RbXe}}$ has a very large error dominated by models of the Rb polarization used in the measurement of $(\kappa_0)_{\mathrm{RbXe}}$.

2.2 Experiment Design

As can be seen in Equation 2.2, a direct measurement of the enhancement factor κ requires knowledge of the Rb magnetization, the frequency shift of the noble gas, and the precise values of the fundamental constants. To avoid measuring the Rb density (difficult for several experimental reasons) stable optical pumping conditions were prepared and the NMR frequency of the ^{3}He and ^{129}Xe shift was recorded before and after a reversal of the Rb magnetization direction. If the Rb magnetization does not change between the frequency shift measurements for ^{129}Xe and ^{3}He then the ratio of the enhancement factor for Rb-^{129}Xe

to Rb-^{3}He is

$$(\kappa_0)_{\mathrm{RbXe}} = (\kappa_0)_{\mathrm{RbHe}} \left(\frac{\gamma_{\mathrm{He}}}{\gamma_{\mathrm{Xe}}}\right) \left(\frac{2\Delta\nu_{\mathrm{Xe}}}{2\Delta\nu_{\mathrm{He}}}\right). \tag{2.4}$$

where γ_X are the noble-gas gyromagnetic ratios and $2\Delta\nu_{\mathrm{X}}$ are the shifts in the respective noble-gas NMR frequency when the Rb vapor is exactly flipped from the low- to high-energy Zeeman polarization state.

This procedure has several advantages. With a reversal of the Rb magnetization from the high energy state (HES) to low energy state (LES) the frequency shift will be twice as large as the shift from zero Rb polarization. If the procedure takes much less time than the drift of the applied magnetic field $\mathbf{B_0}$, the individual shift measurements can be averaged together as independent measurements (Note: the shift is independent of field). Many acquisitions of identical shift measurements permits the use of the average for each nucleus to be used in equation 2.4. Figure 2.1 shows a graphical representation of the experimental concept.

2.3 Apparatus

Six sealed, uncoated Pyrex-glass spheres with an inner diameter d of 7 millimeters were fabricated. Each cell contained a few milligrams of natural isotopic abundance Rb metal along with ^{3}He, Xe (enriched to 86% ^{129}Xe), and N_2 in the various ratios shown in Table 2.1. The cells were prepared with the method briefly outlined in Appendix C.

During the experiment these cells were placed in a safflower oil bath, heated by an aluminum block that was heated by air blown over an external filament heater outside the magnet. The oil was found to be necessary as measured temperature gradients were as much as 20 °C across the cell while heating the cell directly with forced air. The cells

Table 2.1. Summary of cell contents used in this experiment. All cells are sealed, uncoated Pyrex spheres with inner diameters of ∼7 millimeters. Quoted pressures are referenced to 20 °C and the Xe pressure is subject to ∼ 50% uncertainty due to the filling procedure. Cells 155A-C are referred to as low-[Xe] cells and Cell 150A-C are referred to as high-[Xe] cells.

Cell	Xe:N_2:He (Torr)	% Xe
155A	5:160:2200	0.2
155B	10:250:2300	0.4
155C	10:168:2300	0.4
150A	50:175:1000	4.1
150B	110:350:2040	4.4
155D	50:172:1200	3.5

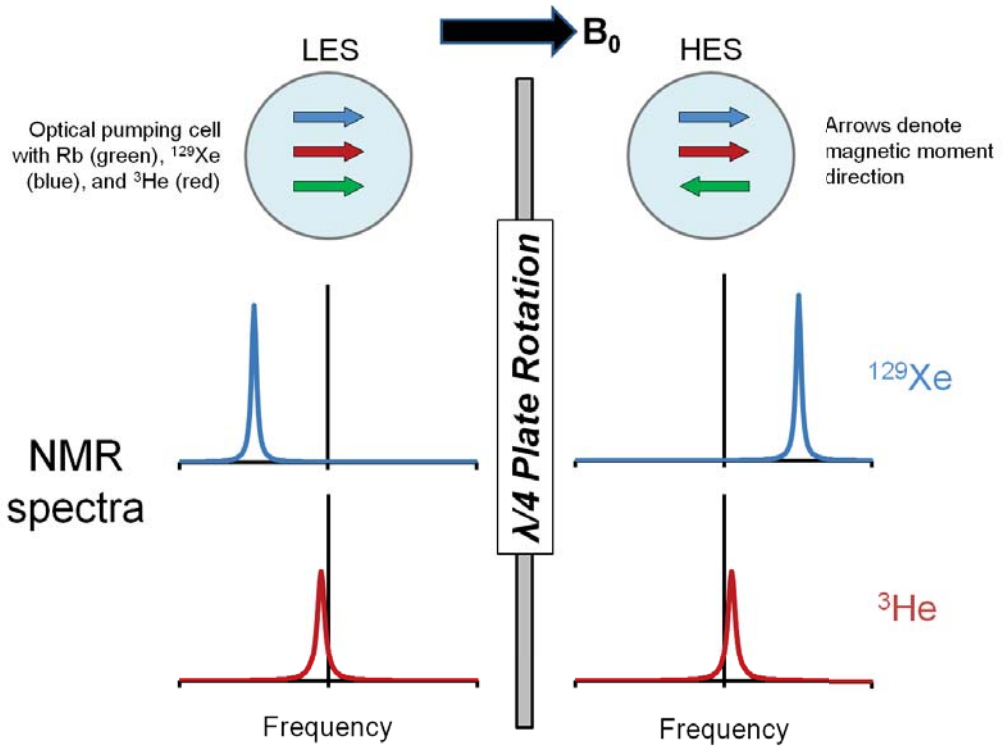

Figure 2.1. Experiment Concept. By measuring both the ^{129}Xe and ^{3}He NMR frequency before and after Rb reversal from HES to LES, $(\kappa_0)_{\mathrm{RbXe}}$ can be deduced by multiplying the ratio of the frequency shift with $(\kappa_0)_{\mathrm{RbHe}}$ and the ratio of the gyromagnetic ratios (Equation 2.4). Rb is reversed by a rotation of the $\frac{\lambda}{4}$ plate in the optic train of the pumping laser. NMR spectra shown are for illustration of the frequency shift only. The spectra are not actual data and are not representative of experimental lineshapes.

were placed in the center of the NMR coil which was wound in a single-turn Helmholtz configuration. When using the ∼10 mm diameter coil (Figure 2.2), the cell was held in place with the coil. When using the ∼35 mm diameter coil a stand was glued in the center of the oil bath to support the cell (Figure 2.3). All results presented here are from the 35 mm probe as $(\kappa_0)_{\mathrm{RbXe}}$ results from the 10 mm probe showed a flip angle dependence that is well explained by B_1 inhomogeneity and the model of chemical exchange invoked to explain the two peak structure present in the ^{129}Xe spectra (see Section 2.5.2 and 2.5.2.1 for further discussion). In both situations the coil was tuned to both the ^{129}Xe (24.5 MHz) and ^{3}He (67.6 MHz) NMR frequencies with tunable capacitors mounted behind the aluminum block. A switch was added to the tuning circuit that enabled switching between the two nuclei without disturbing the experiment in any other way.

The NMR probe (Figure 2.3) was placed in a horizontal 2 T superconducting magnet

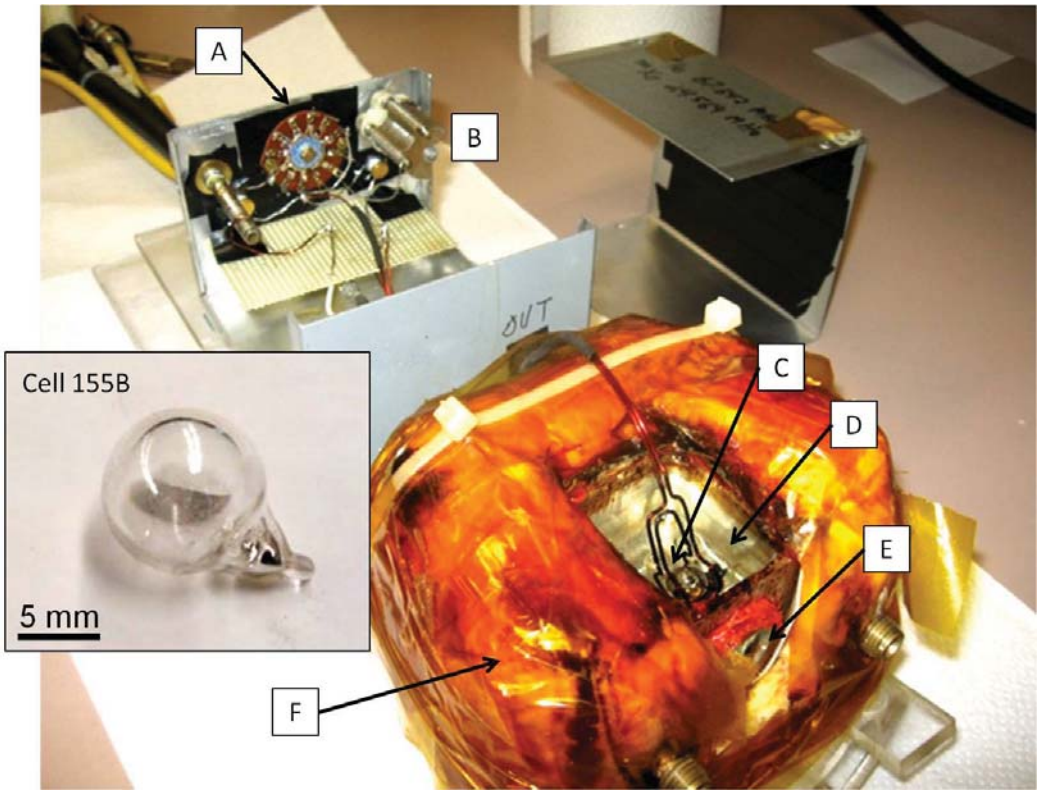

Figure 2.2. Photograph of the 10 mm NMR probe and Cell 155B. (A) Switch to add/remove capacitance in order to change between ^{129}Xe and ^{3}He resonances without disturbing the apparatus. (B) Capacitors to tune the resonance frequency of the tank circuit. (C) NMR coil (∼10 mm diameter) holding the cell immersed in safflower oil (D). (E) Optic window to admit pumping laser light. (F) Hollowed out aluminum housing heated by external filament heater.

(Oxford) that also contained a set of gradient coils (SGRAD MKII 250/150, Techtron 7000 amplifiers) for imaging and a set of rooms temperature shims (Oxford) to homogenize the applied magnetic field. A high-resolution Apollo (Tecmag) NMR spectrometer was used to excite the noble gas and record the FIDs. The FIDs were then outputted to NTNMR software on a computer.

To optically pump the Rb vapor, a 30 W diode-laser array model A317B (QPC Lasers) was used. The laser was tuned to the 795 nm D_1 resonance and narrowed to ∼0.3 nm (∼130 GHz) with a Littrow cavity [19] with a maximum narrowed output of ∼20 W. The Littrow cavity employs an adjustable diffraction grating that allows tuning of the output wavelength by selectively feeding back a specific wavelength into the diode array. The laser was mounted on an optical table with the optical axis aligned with the magnet bore. The optic axis aligned with the magnet bore will henceforth be referred to as horizontal. The

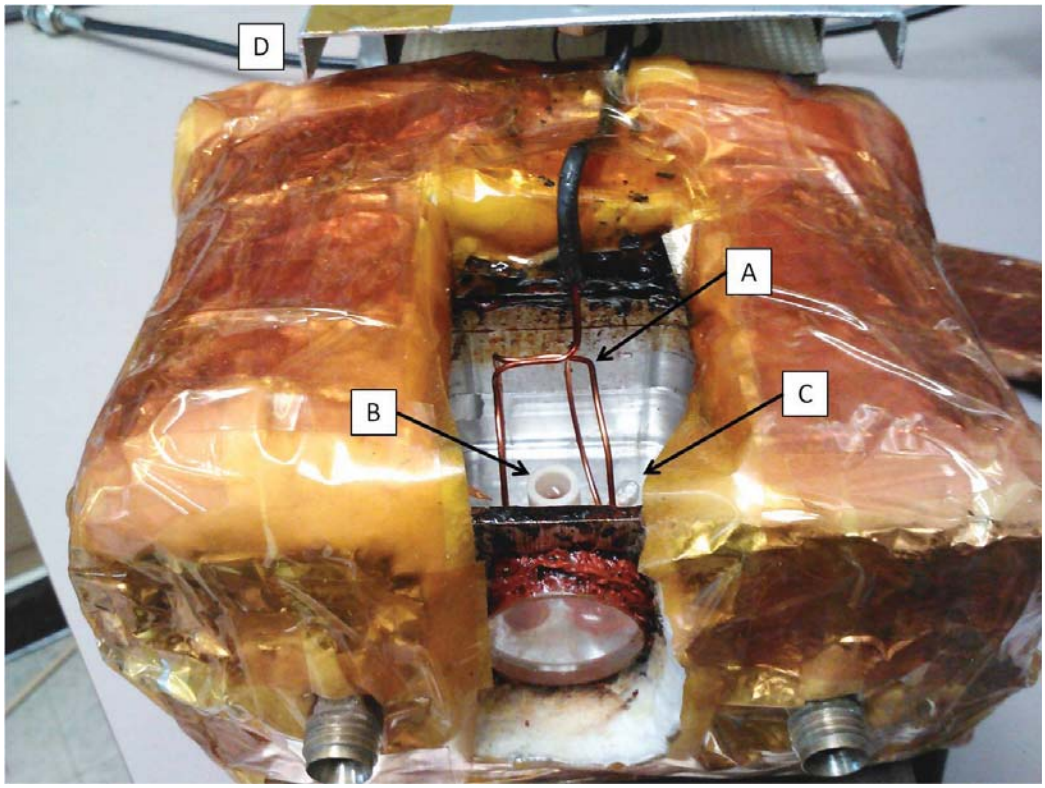

Figure 2.3. Photograph of the 35 mm probe NMR used in the experiment. (A) NMR Coil and (B) stand to support the cell. (C) Resistive thermal device to monitor the oil temperature. (D) Electronics box with the same tunable capacitors and switch shown in Figure 2.2.

final optical element before the last collimating lens was a quarter wave plate that could be easily rotated 180° about an axis through its optical post (perpendicular to horizontal). When the circular polarizer is set at 45° with respect to incident linear polarization, a 180° rotation about the optical post is identical to a 90° rotation of the fast axis about the horizontal axis. The result of either of these rotations is a reversal of the helicity of light. The reversal of the helicity of the pumping light will reverse the Rb magnetization by 180° with respect to the static magnetic field. Figure 2.4 is an image of the laser and associated optics.

2.4 Data Acquisition

The following procedure was used to acquire data. 1) Heat the oil and cell to the desired temperature. 2) Check that the probe is correctly tuned for both ^{129}Xe and ^{3}He. 3) Optically pump for 1-2 hours to allow the ^{3}He polarization to build up. 4) Use the auto-

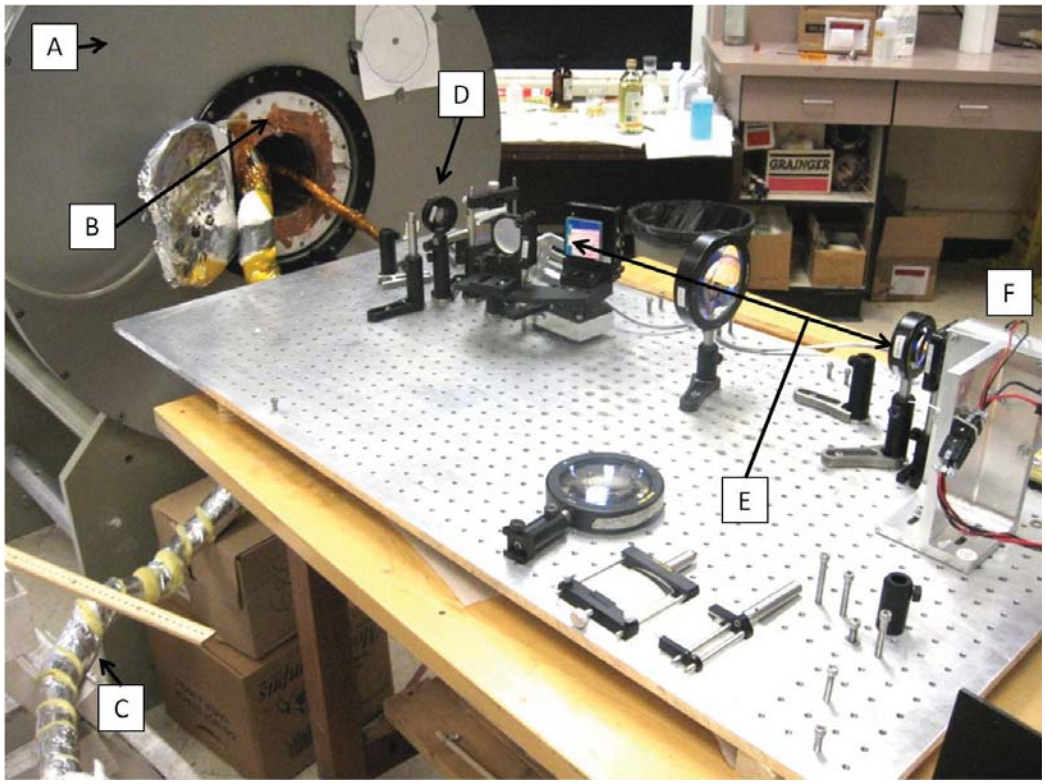

Figure 2.4. 30 W, 795 nm optical pumping laser and optics. (A) 2 T superconducting magnet. (B) Room temperature shims and gradient coils. (C) Pipe carrying warm air from the heating element to probe. (D) $\frac{\lambda}{4}$ plate rotated to reverse Rb magnetization. (E) External Littrow cavity to narrow the pumping light from the diode array. (F) Watercooling block to which the diode array is mounted.

shimming procedure provided with the NTNMR software to control the room temperature shims and maximize the ^{3}He T_2^*. The ^{3}He FID was used to shim because it is unaffected by diffusion of ^{3}He through regions of polarized and unpolarized Rb and guarantees the most homogeneous field across the cell. 5) Acquire 20-80 FIDs with a rapid reversal of the Rb magnetization between each acquisition ($\sim$10 minutes). 6) Switch the NMR probe to the other nucleus without otherwise changing the apparatus. 7) Acquire 20-80 FIDs again with a rapid reversal of the Rb magnetization between each. 8) Switch back and forth between ^{3}He and ^{129}Xe to improve statistics if desired.

The idea behind this procedure of rapid switching of the Rb magnetization between acquisitions was to remove any effects of a slow drift of the applied magnetic field, i.e., the frequency shift is independent of magnetic field and as a long as the FIDs are acquired rapidly (1-2 seconds) compared to any static field drift, the shifts measured between any two consecutive shots can be averaged together as identical independent measurements. Figure

2.5 and 2.6 show a simple schematic of this procedure as well as representative data. Reversal of the Rb magnetization was done "by hand" by rotating the $\frac{\lambda}{4}$ plate 180° about it's vertical axis as fast as possible. The Rb optical pumping time is of order milliseconds and thus the Rb magnetization is reversed instantaneously relative to the ^{129}Xe (∼5-30 seconds) and ^{3}He (∼60 minutes) spin-exchange times allowing NMR spectra to be acquired after rotation of the $\frac{\lambda}{4}$ plate before any appreciable loss of the noble gas magnetization.

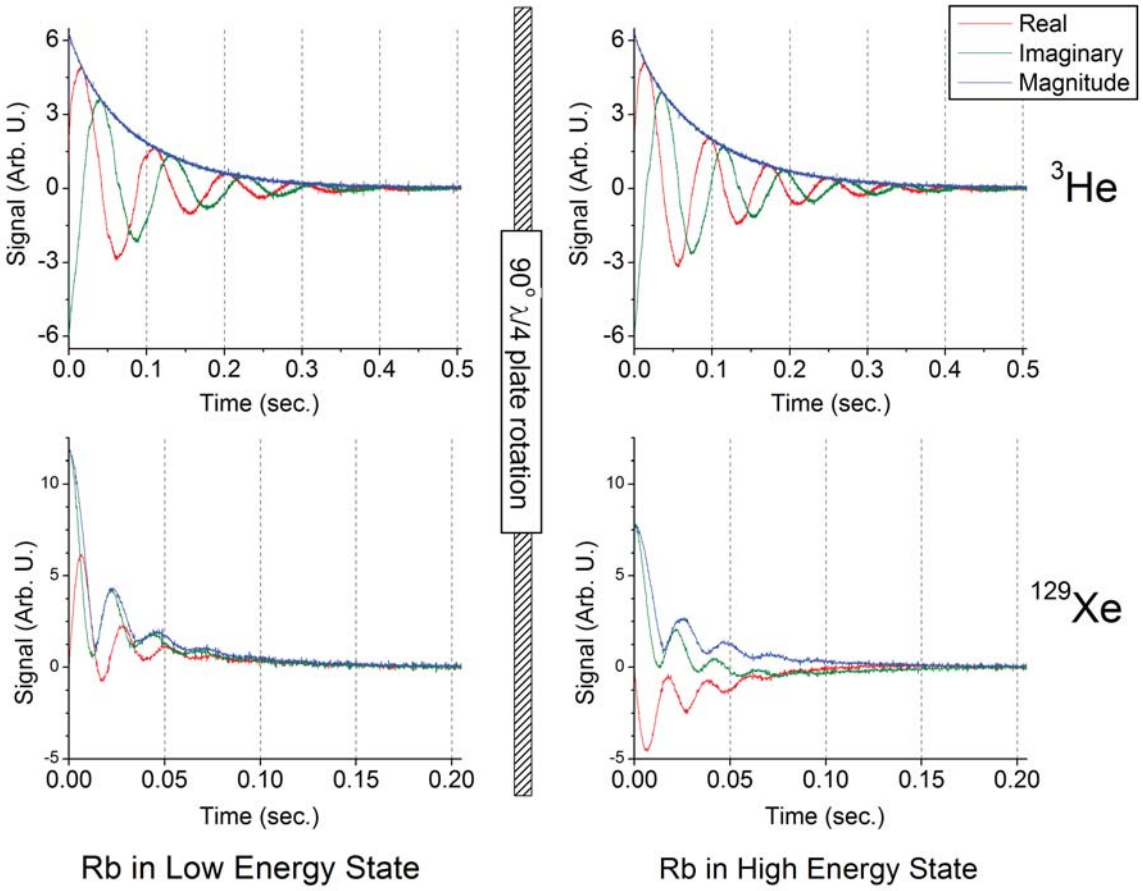

Figure 2.5. Graphical representation of the experiment and representative data. An FID is acquired, the $\frac{\lambda}{4}$ plate is rotated (reversing the Rb magnetization), and another FID is immediately acquired. The entire procedure (acquire-reverse-acquire) takes ∼1-2 seconds This is done for ^{129}Xe and ^{3}He 10-40 times to allow for averaging. The ^{3}He FID's exhibit smooth exponential decays in all cases. The ^{129}Xe FID's were acquired in identical experimental conditions as the ^{3}He FID's and show a beating which is characteristic of two resonances. The data shown are from Cell 150A at 200 °C.

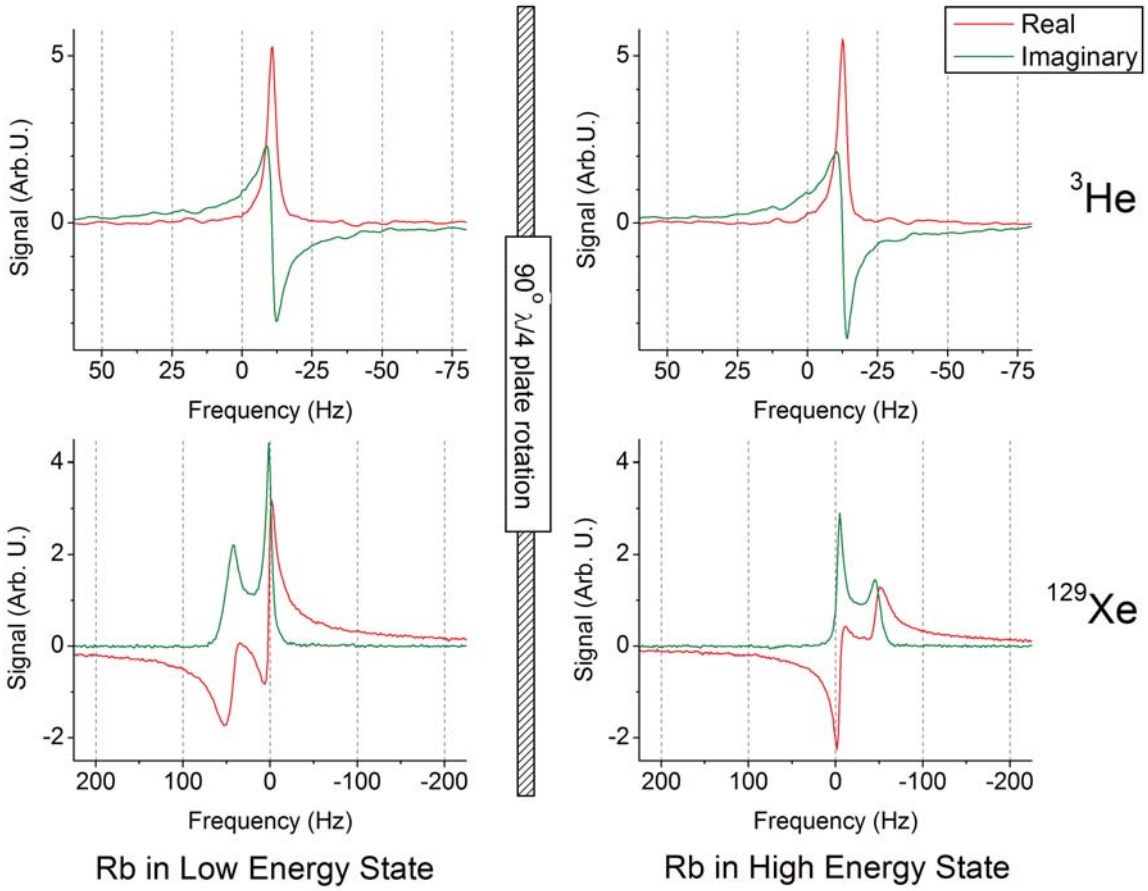

Figure 2.6. FFT of the data shown in Figure 2.5. The ^{3}He spectra show a single, narrow peak that shifts slightly under Rb magnetization reversal as opposed to the Xe where the spectrum is reversed and shifts by ∼50 Hz, but the peak near 0 Hz does not shift much. The ^{129}Xe peak that stays near 0 Hz is from ^{129}Xe colliding with unpolarized Rb, and the peak that shifts by ∼100 Hz is from ^{129}Xe colliding with polarized Rb. See Section 2.5 for further discussion about the exchange broadened ^{129}Xe spectra.

2.5 Data Analysis and Discussion

With a high precision measurement of the noble-gas NMR frequency and knowledge of $(\kappa_0)_{\mathrm{RbHe}}$ Equation 2.4 can be used to obtain values for $(\kappa_0)_{\mathrm{RbXe}}$. However, given the shape of the spectra demonstrated in Figure 2.6 the analysis of the NMR frequency shift requires careful handling of several subtleties.

Figures 2.6 and 2.7 show typical FFT spectra prior to any data analysis. The ^{129}Xe and ^{3}He have decidedly different structures with the following characteristics: 1) the ^{3}He spectra always exhibit a single, narrow resonance that never changes shape; 2) the ^{129}Xe spectra always exhibit two peaks; 3) the ^{129}Xe peak separations and widths increase with

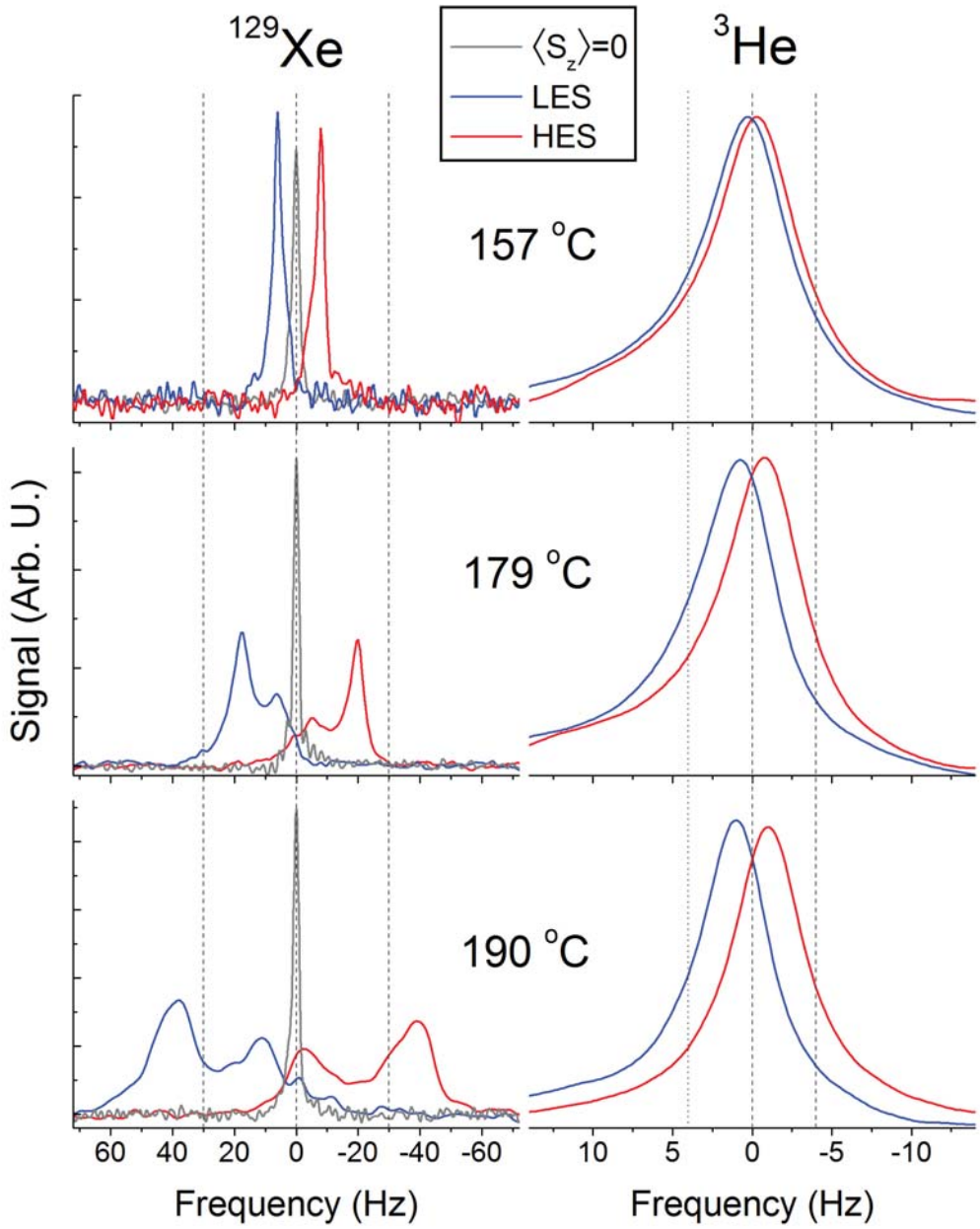

Figure 2.7. Typical ^{3}He and ^{129}Xe raw spectra from cell 155B acquired under steady-state SEOP conditions. The narrow ^{129}Xe peak at 0 Hz was acquired with the laser blocked; it has been amplitude-normalized to appear on the same graph. The double peak in the ^{129}Xe spectra at all but the lowest temperatures represents regions of highly polarized and nearly unpolarized Rb vapor; the lines are broadened and begin to coalesce due to diffusion of ^{129}Xe between these two regions. For ^{3}He, the much smaller frequency-shift dispersion and more rapid diffusion yields a single narrow peak in all cases. The respective shifts in the spectral center of mass upon reversal of the Rb magnetization were used in Eq. 2.4 to extract $(\kappa_0)_{\mathrm{RbXe}}$.

temperature; 4) the relative strength of the two peaks becomes more equal at higher temperatures; 5) when blocking the laser the ^{129}Xe peak is always very narrow (∼2-4 Hz), single resonance directly between the HES and LES spectra.

The ^{129}Xe peak structure is due to Xe diffusing between regions of polarized and unpolarized Rb much more rapidly than the Rb-Xe spin exchange rate and on the order of the difference in resonance frequency between regions of polarized and unpolarized Rb as defined by Equation 2.2. This is identical to the NMR phenomena known as chemical exchange [5], except instead of *exchanging* between two chemically distinct sites, the ^{129}Xe is *diffusing* between regions of polarized and unpolarized Rb in the cell (see Section 2.5.2). These distinct regions of polarized and unpolarized Rb are due to attenuation and lensing of the optical pumping laser inside the optical pumping cell.

Since Equation 2.2 is a collisionally averaged shift that is proportional to the *volume averaged* expectation value of the a electron spin, the correct frequency shifts to use in Equation 2.4 are the spectral center-of-mass (COM) or "first moment" [64] shifts. However, using a COM analysis to compensate for an inhomogeneous Rb magnetization has three requirements.

1) The ^{3}He and ^{129}Xe magnetization distributions must be identical in the cell. That is, the ^{129}Xe spectrum must not be weighted incorrectly towards the polarized Rb peak when compared to the ^{3}He spectrum. Another way to view this is that the ^{129}Xe must diffuse around the cell much faster than the characteristic ^{129}Xe-Rb spin-exchange time. This was found to be true as the characteristic spin-exchange time was measured to be 3-20 seconds, compared to the diffusion time measured at ∼150 ms (see Section 2.5.1). ^{129}Xe was also found to be homogeneous with imaging (see Section 2.5.3).

(2) The Rb magnetization distribution must not change between measurements of the ^{129}Xe and ^{3}He shifts (typically 10-15 minutes). This could not be determined experimentally since Rb electron resonances at 2 T are well into microwave frequencies and pose many experimental difficulties. However, stability of the Rb magnetization between ^{3}He and ^{129}Xe measurements was inferred from the repeatability and stability of the measured value of $(\kappa_0)_{\mathrm{RbXe}}$. Over 3000 frequency shifts were measured at different temperatures over the course of several months.

(3) Since the Rb magnetization is inhomogeneous there is a through space magnetic field inside of the cell generated by the Rb atoms. If this through space field, on average, generates a ^{3}He frequency shift on order of the contact shift due to $(\kappa_0)_{\mathrm{RbHe}}$, then the ^{3}He

shift cannot be easily related to the ^{129}Xe shift and Equation 2.4 is no longer valid. To determine if this was indeed the case, numerical modeling was done of the through-space dipole field inside of a sphere with various magnetization geometries (see Section 2.5.5). The most extreme geometries yielded, at most, less than a 1% effect.

Given the above conditions were satisfied, the COM shift can be used in equation 2.4. Measuring the ^{3}He spectral COM is simple since ^{3}He is undergoes fast exchange (see Section 2.5.2), and consequently the position of the peak corresponds to the spectral COM. The ^{129}Xe spectral COM were not so simple. The first attempts were numeric integrals over a chosen frequency range, but the results were wildly inconsistent due to integration of the noise not resulting in zero, and the integrals were also dependent on the phase of the real signal relative to the spectrometer reference. Attempts were also made at fitting the peaks to two-site chemical exchange models; however, the expression is complicated (Equation 2.5) and the assumption that only two sites exist is not true, although it is a reasonable simimation (see Section 2.5.2). Instead the ^{129}Xe FIDs were multiplied by an exponential (apodization) with a time constant approximately four to five times the resonance splitting, Fourier transformed, and the position of the maximum value of the magnitude signal was recorded. This procedure conserves the COM information (Appendix A) and the maximum value of the magnitude will correspond to the peak position of a correctly phased real spectrum. Thus, a comparison of the ^{3}He peak shift to the ^{129}Xe apodized peak shift can be done to extract $(\kappa_0)_{\mathrm{RbXe}}$. Table 2.2 shows sample frequency shift data.

Six cells were made and they can be broadly divided into two categories: high Xe-concentration with 50-100 Torr (high-[Xe]), and low Xe-concentration with 5-10 Torr (low-[Xe]). See Table 2.1 for a complete description of the cell contents. The calculated values of $(\kappa_0)_{\mathrm{RbXe}}$ are plotted vs. temperature T for the three low-[Xe] cells in Figure 2.8. The error bars shown reflect only the statistical uncertainty in the measured frequency-shift ratio and do not include the uncertainty in $(\kappa_0)_{\mathrm{RbHe}}$; at the lower temperatures the error is dominated by the large relative uncertainty in the small ^{3}He frequency shifts. The low-[Xe] cells (both individually and collectively) show no significant temperature dependence between 140-220 °C; the weighted average of all of these points yields an uncertainty of $< 1\%$. If we take the same weighted average on a cell-by-cell basis, a larger spread is observed (see Table 2.3), suggesting some unknown systematic errors of a few-percent. These errors could include small cell-dependent geometrical effects. In some cases, residual asymmetries were apparent in the HES and LES ^{129}Xe spectra with respect to the unpolarized-Rb peak

Table 2.2. Sample frequency shift data after processing described in Section 2.5. $\bar{x}$ is the average, and $\sigma_{\bar{x}}$ is the standard deviation of the mean. The error in $(\kappa_0)_{\mathrm{RbXe}}$ is the statistical error of each nucleus added in quadrature. There is an error associated with $(\kappa_0)_{\mathrm{RbHe}}$. However, this has been added to the final result and not to the individual values. For every point in Figure 2.8, a similar set of data was acquired.

	Experiment #61: 201°C		Experiment #61a: 190°C	
	$\Delta\nu$ ^{3}He (Hz)	$\Delta\nu$ ^{129}Xe (Hz)	$\Delta\nu$ ^{3}He (Hz)	$\Delta\nu$ ^{129}Xe (Hz)
	3.052	91.6	1.908	56.9
	3.242	95.6	1.812	61
	3.147	85.5	1.812	52.9
	3.243	99.8	1.812	55
	3.242	91.6	1.812	56.9
	3.147	111.8	1.908	52.9
	3.433	91.6	1.908	52.9
	3.243	97.7	2.098	50.8
	3.052	86.8	1.811	56.9
	3.147	95.6	1.716	56.9
$\bar{x} \pm \sigma_{\bar{x}}$	**3.19±.04**	**94.8±2.7**	**1.86±.03**	**55.3±1.0**
$(\kappa_0)_{\mathrm{RbHe}}$	6.397		6.295	
$(\kappa_0)_{\mathrm{RbXe}}$	**519±16**		**512±12**	

Table 2.3. Summary of cell contents and $(\kappa_0)_{\mathrm{RbXe}}$ results. $(\kappa_0)_{\mathrm{RbXe}}$ is computed for each of the low-[Xe] cells from the weighted average of that cell's data; we have excluded the high-[Xe] cells because of their anomalous behavior at high temperature (see Section 2.5.6)

Cell	Xe:N_2:He (Torr)	$(\kappa_0)_{\mathrm{RbXe}}$
155A	5:160:2200	495±6
155B	10:250:2300	490±5
155C	10:168:2300	530±9
150A	50:175:1000	–
150B	110:350:2040	–
155D	50:172:1200	–

(Figures 2.7 and 2.6). These may be due to imperfections or drifts in laser tuning (see Section 2.5.4) or power and may introduce some additional error at the ∼1% level. However, we found the two spectral COMs to be equidistant from the unpolarized-Rb peak in all data used to measure $(\kappa_0)_{\mathrm{RbXe}}$. For the above reasons, the error was accordingly increased in the shift ratio, which is represented by the hatched range in Figure 2.8. Finally, we add the 1.8% uncertainty in the value of $(\kappa_0)_{\mathrm{RbHe}}$ [54] in quadrature to this range to arrive at our final result in Equation 2.1.

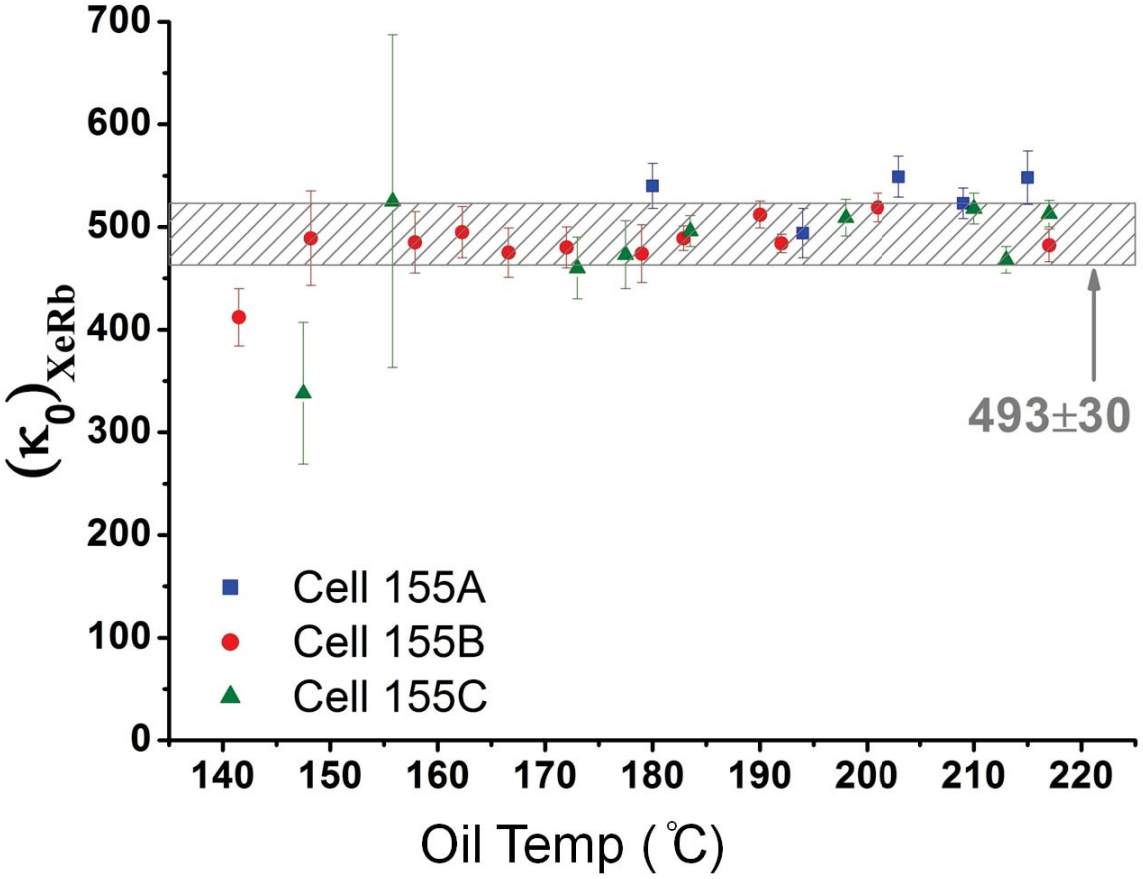

Figure 2.8. Enhancement factor $(\kappa_0)_{\mathrm{RbXe}}$ plotted vs. temperature for three low-[Xe] cells. The weighted average of all the low-[Xe] data points is 493, with the estimated uncertainty shown by the gray hatched region. This uncertainty is estimated from cell-to-cell variations in the weighted average of $(\kappa_0)_{\mathrm{RbXe}}$ (see Table 2.3). These temperature-independent data represent the best estimate of $(\kappa_0)_{\mathrm{RbXe}}$.

Theoretical calculations in reference [59] resulted in $(\kappa_0)_{\mathrm{RbXe}} \approx 700$ with little to no temperature dependence. The discrepancy from our value is most likely due to imprecise knowledge of the molecular van der Waals potentials and unperturbed valence electron wavefunction enhancement values.

The remainder of this chapter will be broken into sections to discuss several control experiments, chemical exchange, additional experimental observations, and the anomalous high-[Xe] measurements.

2.5.1 ^{129}Xe Diffusion Measurement

A measurement of the ^{129}Xe diffusion coefficient will provide two pieces of information. First, it will provide a check on the assumption that ^{129}Xe diffuses across the cell faster than the spin-exchange time resulting in a homogeneous noble-gas magnetization. Second, it can provide an estimate of the exchange rate to support the hypothesis of chemical exchange broadened ^{129}Xe spectra.

Measurement of the diffusion coefficient D_{Xe} was performed using the Carr-Purcell-Meiboom-Gill (CPMG) pulse sequence [64]. The CPMG sequence is a 90° pulse followed by a series of 180° pulses of alternating phase all done while applying a Z-gradient of known value. The 180° pulses refocuses transverse coherence loss due to magnetic field inhomogeneities into echos between pulses, and the resulting echo decay envelope is due to diffusion through the applied gradient. The phase alternation removes the error accumulated from sequential imperfect 180° pulses. The CPMG was performed six times under varying conditions: an identical pulse sequence (same echo delay) was done with the pump laser on and off, and with the Z-gradients set to 0%, 4% (.81 G/cm), and 6% (1.21 G/cm) of their maximum operating range. The result for D_{Xe} from the 4% and 6% gradients were averaged together and assigned a 10% error from the equipment manufacturers specifications. Figure 2.9 shows sample data.

The average of all the different CPMG runs together yielded $D_{\mathrm{Xe}} = 0.51 \pm 0.05$ cm^2/s. The diffusion coefficient is highly dependent on the gas composition and using previously measured values from the literature to estimate the diffusion coefficient for the gas composition in this experiment demonstrated reasonable agreement. The diffusion coefficient of Xe in 1 atmosphere of N_2 is $\sim$0.21 cm^2/s [74] when scaled for temperature ($D \propto T^{3/2}$ [52]). In reference [37], the calculated diffusion coefficient for a 25%-75% mixture of Xe-He at 175 °C is stated to be $\sim$1 cm^2/s. Scaling the diffusion coefficients for pressure

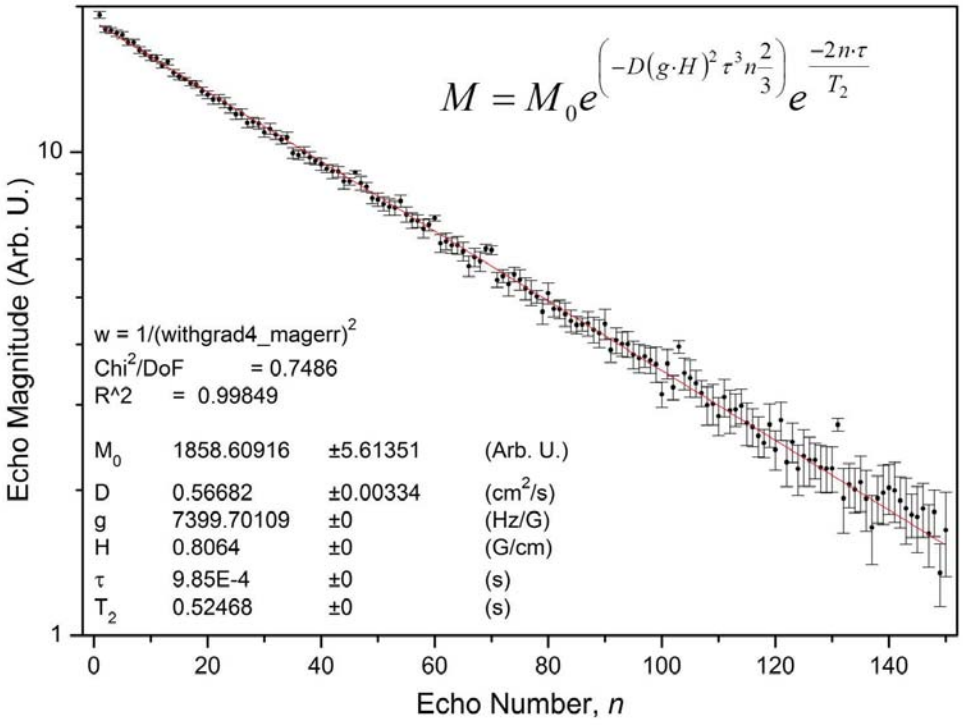

Figure 2.9. CPMG decay taken on cell 150A at 170°C. The error bars are from finding the standard deviation of the top 11 points of each echo. The parameters D and M0 are allowed to float; T2 was found by plotting the data with no gradient, setting D and H to zero, and allowing T2 to float.

and the gas ratio in this experiment, and then adding them in reciprocal, gives .54 cm^2/s. This is probably an underestimate of the diffusion coefficient given the gas composition in this experiment since cell 150A does not have a 25%-75% Xe-He gas ratio; however, the results are consistent.

The spherical measurement cells had an inner diameter of ∼7 millimeters, and the characteristic diffusion rate $1/\tau_d \approx 6D_{\mathrm{Xe}}/d^2 \approx 10$ hz. This is on the order of the typical resonance splitting seen in the ^{129}Xe spectra and the characteristic diffusion time (∼100 ms) is much faster than the measured Rb-^{129}Xe spin-exchange times (which were 3-20 seconds depending on temperature).

2.5.2 "Chemical" Exchange Between Regions of Polarized and Unpolarized Rb

The well-known NMR phenomenon of chemical exchange [5, 58] has been studied extensively and can provide much physical insight into the dynamics of spin systems. This

effect manifests itself when spins move between distinct resonances on T_2 timescales, i.e., timescales that correspond to the difference in precession frequencies across the sample. Depending on the exchange rates relative to the difference in frequencies, the NMR spectrum can be drastically different.

The equation for a NMR spectrum where spins are exchanging between two distinct resonant frequencies can be acquired by solving the modified Bloch equations with 2-site chemical exchange [58]:

$$f(\nu) = \Im\left[\frac{i\gamma B_1 M_0 \left(\left(\frac{1}{T_2} - 2i\pi\left(\Delta\nu_{\mathrm{B}}\right)\right) P_{\mathrm{A}} + k_{\mathrm{A}} + k_{\mathrm{B}} + \left(\frac{1}{T_2} - 2i\pi\left(\Delta\nu_{\mathrm{A}}\right)\right) P_{\mathrm{B}}\right)}{\left(\frac{1}{T_2} - 2i\pi\left(\Delta\nu_{\mathrm{B}}\right)\right)\left(\frac{1}{T_2} - 2i\pi\left(\Delta\nu_{\mathrm{A}}\right)\right) + k_{\mathrm{B}}\left(\frac{1}{T_2} - 2i\pi\left(\Delta\nu_{\mathrm{A}}\right)\right) + k_{\mathrm{A}}\left(\frac{1}{T_2} - 2i\pi\left(\Delta\nu_{\mathrm{B}}\right)\right)} \right], \tag{2.5}$$

where ν is the excitation frequency, $i = \sqrt{-1}$, γ is the gyromagnetic ratio, B_1 is the RF field strength, M_0 is the magnetization, $\Delta\nu_{\mathrm{B}} = \nu_{\mathrm{B}} - \nu$ and $\Delta\nu_{\mathrm{A}} = \nu_{\mathrm{A}} - \nu$, ν_{A} and ν_{B} are the rotating-frame precession frequencies while in site A and B, respectively, T_2 is the relaxation in the absence of exchange which can be different for the two sites but has been chosen to be equal for simplicity, k_{A} and k_{B} are the exchange rates per atom from A to B and B to A, respectively, and P_{A} is the relative population of A with $P_{\mathrm{A}} + P_{\mathrm{B}} = 1$. A plot of this function with different exchange rates is shown in Figure 2.10.

In terms of shaping an NMR spectrum, three different chemical-exchange regimes exist which are demonstrated in Figure 2.10. The "slow exchange" regime where two distinct resonant peaks are apparent with minimal broadening is defined by $\tau_{\mathrm{ex}}\left(\Delta\omega\right) \ll 1$ where $\Delta\omega$ is the difference between the two resonant frequencies. The "intermediate exchange" regime where the two resonances begin to broaden and coalesce is defined by $\tau_{\mathrm{ex}}\left(\Delta\omega\right) \simeq 1$. The "fast exchange" regime is when the individual resonances have narrowed to a single resonance positioned at the population-weighted average of the two resonances. Fast exchange is defined by $\tau_{\mathrm{ex}}\left(\Delta\omega\right) \gg 1$. These different exchange regimes can be thought about qualitatively by picturing spins (or arrows) dephasing in the rotating frame. After a 90° pulse the spins are all in the transverse plane in the same direction. The two resonant frequencies will each have a given population that can be thought of as two groups of spins and each group has their own T_2 determined by the sample environment. In the slow exchange regime, the two groups of spin never exchange and the transverse coherent magnetization will "beat" with the difference in precession frequency in the rotating frame

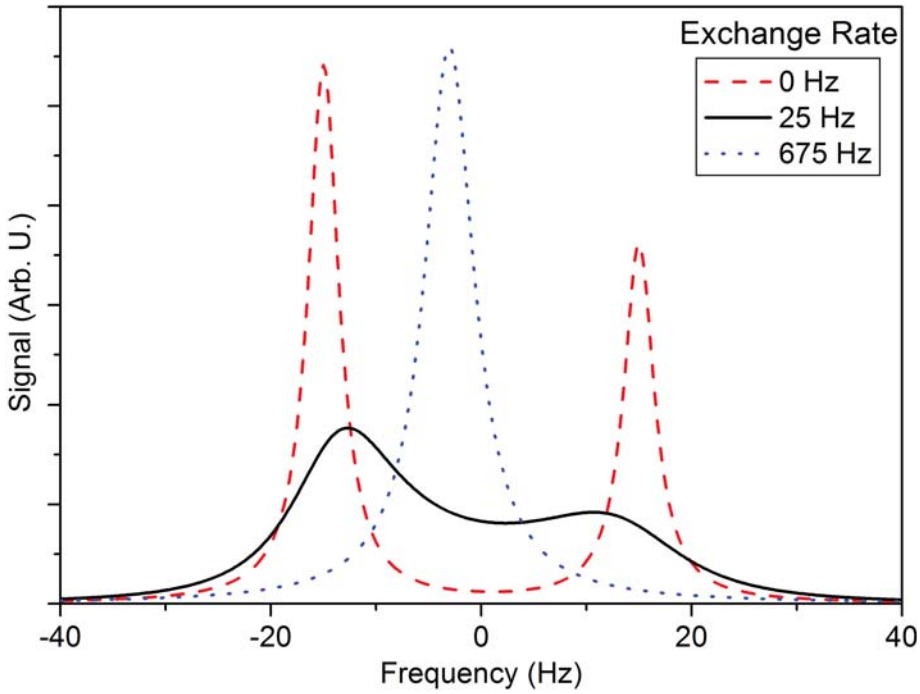

Figure 2.10. Simulation of two site chemical exchange using equation 2.5. The average exchange rate per atom is shown in the legend. The population ratio of the two sites is 60/40 with a resonance splitting of 30 Hz. Actual ^{129}Xe spectra are similar in shape to the intermediate exchange (black line) where it is clear the peaks are broadening and moving towards each other with increasing exchange, whereas ^{3}He data are better represented by the fast exchange peak (blue).

and dephase with a combination of the T_2s from the different resonances. In the fast exchange regime, the spins are mixed too fast to generate a coherent difference between the two resonances resulting in an average of two frequencies. Intermediate exchange is a combination of slow and fast exchange. While the concept of exchange broadening has been introduced in the context of two distinct resonant frequencies, it should be understood that any number of resonances can be present, but the physical picture will not change much. However, Equation 2.5 will no longer be valid and picturing the spins bouncing between different resonances in the rotating frame becomes confusing.

The connection to chemical exchange in an optical pumping cell is best thought of in terms of where the optical pumping light is inside the optical pumping cell. The cell is spherical and will focus the incoming optical pumping light, which will create a sharp boundary between regions of light and no-light as the laser propagates towards the back of the cell. In addition to lensing, the pumping laser can be attenuated by the Rb vapor.

At typical running temperatures, the cell is hundreds of optical depths thick. Because the absorption of the laser light is polarization dependent once the photon flux drops below the necessary threshold to polarize the Rb vapor, the light will penetrate about only one optical depth further into the cell [72]. Given that our cells were ∼7 millimeters in diameter, one optical depth would be ∼100 micrometers thick. Thus, the two effects that shape the laser profile inside the cell will both create sharp boundaries between regions of polarized and unpolarized Rb, which can lead to an exchange broadened spectrum because, according to Equation 2.2, the resonant frequency for ^{129}Xe is dependent on the Rb polarization.

The ^{129}Xe spectra always have two peaks. One of the two peaks is close to 0 Hz and when the Rb is reversed only moves a small amount to the other side of 0 Hz. If this peak is due to contact with unpolarized Rb, it should not move when the Rb is reversed. However, if the ^{129}Xe is exchanging with a different resonant frequency (namely coming in contact with polarized Rb), the unpolarized peak that should be at 0 Hz can be shifted slightly slightly off of 0 Hz towards the other resonance. The shift of the ^{129}Xe resonance in contact with unpolarized Rb is evidence that strongly indicates the ^{129}Xe spectra are, in fact, exchange broadened. Additional qualitative proof of exchange broadened ^{129}Xe spectra is that the simulated intermediate-exchange spectrum (black line in Figure 2.10) is very similar to actual ^{129}Xe spectra (Figures 2.6 and 2.7) at higher temperatures.

The change in the ^{129}Xe spectra as a function of temperature (Figure 2.7) is easily understood in the context of chemical exchange. At the lowest temperatures (Figure 2.7 150 °C) the contribution from the unpolarized Rb peak is small and results in just a "shoulder" towards 0 Hz on the main peak, and at the highest temperatures, the spectra exhibit two distinct peaks mirrored about zero. The reason for this change as a function of temperature is twofold. First, the Rb number density increase exponentially with temperature [38], and for a given polarization the difference in ^{129}Xe frequency when in contact with polarized and unpolarized Rb should increase exponentially as well. Second, because the Rb number density increases with temperature the pumping laser cannot penetrate as deep into the cell at the higher temperatures making the region of polarized Rb much smaller. The diffusion coefficient will change by only about 15% from 150 °C to 200 °C and as a result, the lower temperature ^{129}Xe spectra more closely represent fast-exchange, whereas at higher temperatures, the spectra become distinctly reminiscent of the intermediate-exchange regime. That is, the increase in diffusion coefficient cannot keep up with the increase in frequency difference as the temperature increases.

2.5.2.1 ^{129}Xe Flip Angle Dependence of $(\kappa_0)_{\mathrm{RbXe}}$

While making early measurements of $(\kappa_0)_{\mathrm{RbXe}}$, a dependence on the size of the ^{129}Xe flip angle was noticed. This dependence does not make sense from the theory that yields Equation 2.2. The frequency shift is dependent only on $(\kappa_0)_{\mathrm{RbXe}}$ and the Z-component of the Rb magnetization. For a transverse noble gas magnetization to appreciably effect its own frequency shift, the Rb magnetization would have to be affected on T_2 timescales. This cannot be true since the fastest measured spin-exchange times were of order 5 seconds and T_2^* with the laser blocked (no Rb polarization) was never longer than a few hundred milliseconds.

The cause of this flip angle dependence was due to the RF field strength being inhomogeneous across the sample, which caused a difference in the flip angle between ^{129}Xe in regions of polarized and unpolarized Rb. Even though the ^{129}Xe magnetization is uniform across the cell, the time required to rehomogenize the cell by diffusion after disturbing the magnetization is on the order of 100 ms (see Section 2.5.1). Therefore, if the ^{129}Xe that is in contact with unpolarized Rb is flipped by the RF pulse slightly less than ^{129}Xe in contact with polarized Rb, then the spectrum will be weighted towards the polarized Rb peak. This, in turn, will give an incorrect result for $(\kappa_0)_{\mathrm{RbXe}}$ when compared to ^{3}He, which homogenizes instantaneously on all timescales relevant to this experiment.

With the the 10 mm coil (Figure 2.2) at small ^{129}Xe flip angles (less than 20°), the effect was found to disappear. However, to avoid this issue completely, a bigger Helmholtz coil was constructed (Figure 2.3) to generate a homogeneous RF field strength across the entire cell.

2.5.3 ^{129}Xe Imaging to Verify Noble Gas Homogeneity

The assumption that the ^{129}Xe magnetization distribution must be identical to the ^{3}He (i.e., it must be uniform) is essential to perform a first-moment analysis. The CPMG diffusion measurements provide strong evidence for ^{129}Xe homogeneity, however, imaging provided direct verification.

1-D slice selection MRI was done on cell 150A at 170°C. 1-D slice select in the Z-direction selects slices and collapses all the signal amplitude from the X and Y directions to a single point. Therefore the signal strength S of an image of a uniformly magnetized sphere is $S(z) \propto \pi\left(R^2 - z^2\right)$ where z is the position along the sphere with the center of the sphere at 0, and R is the radius of the sphere. Figure 2.11 shows the images acquired with

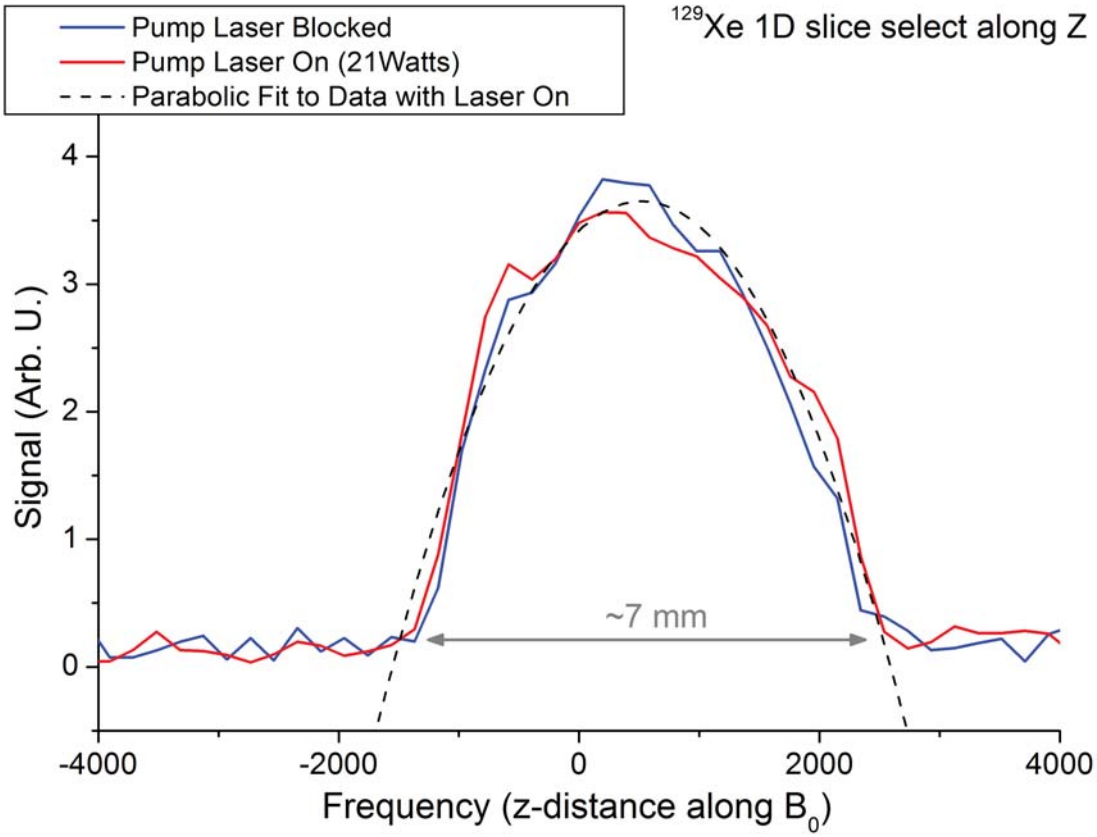

Figure 2.11. ^{129}Xe signal strength as a function of position along the z-axis (along the magnetic field and optical pumping axis). The signal strength represents all the signal from ^{129}Xe in the x and y directions at a chosen z value. The signal with the laser on has been scaled to amplitude match the signal with the laser off. No significant difference between signals with the laser on and laser off indicates the ^{129}Xe frequency shift data is not preferentially weighted towards the polarized Rb peak.

no difference within error between the images acquired with the pump laser on or off and both images are parabolic as expected. If the Xe magnetization is inhomogeneous while optically pumping, then there would be a difference between the images with the laser on or off.

2.5.4 SEOP at High Field: σ_+ and σ_- Energy Shift

In early measurements, after extensive shimming of the main magnetic field using the ^{3}He T_2^*, an asymmetry in the spectrum shape was sometimes still observed between the ^{129}Xe LES and ^{129}Xe HES spectra. The cause of this asymmetry was traced back to the tuning of the optical pumping laser. To reverse the Rb magnetization, the pumping laser is switched from $\sigma+$ to $\sigma-$ or vice versa (Section 1.1.2), and because the alkali vapor is

being optically pumped at 2 T, the $m_j = -1/2 \rightarrow m_j = 1/2$ transition selected by $\sigma+$ will be shifted in energy relative to the $m_j = 1/2 \rightarrow m_j = -1/2$ transition selected by $\sigma-$ by ∼30 GHz. The pumping laser had a narrowed width of ∼0.3 nm at 795 nm which is ∼140 GHz. If the spectrum of the pumping laser is such that the absorption of $\sigma+$ light is different than $\sigma-$ then the penetration depth of the laser will change and consequently the NMR spectrum will change as it depends heavily on the ratio of polarized to unpolarized Rb in the cell. Figure 2.12 shows ^{129}Xe spectra as a function of laser tuning.

In all data presented in this dissertation, the laser was tuned prior to data acquisition to ensure the HES and LES spectra were symmetric and, more importantly, the COM was positioned an equal amount away from zero for both HES and LES spectra.

2.5.5 Numerical Modeling of the Geometric Effect

The imaging and diffusion measurements provide strong evidence that the noble gas magnetization is uniform and will therefore not have a through-space effect on the NMR shift. However, a through-space magnetic dipole field from the nonspherical geometry of the Rb magnetization can possibly have an effect on the noble-gas NMR. To test this, numerical modeling was done on several geometries, and the averaged through-space magnetic field was compared to $\frac{8\pi}{3}\left(\kappa_0\right)_{\mathrm{RbHe}}$. In the most extreme cases, the numerical modeling results showed the effect would be negligible.

The magnetic field due to a magnetized object discretized as a collection of magnetic dipoles is written as [33]

$$\mathbf{B} = \int \frac{3\mathbf{n}(\mathbf{n}\cdot\mathbf{M}) + \mathbf{M}}{|\mathbf{x}-\mathbf{x}'|^3}\,\mathrm{d}^3x' + \frac{8\pi}{3}\delta(\mathbf{x}-\mathbf{x}')\ , \tag{2.6}$$

where $\mathbf{x}$ is the field point, $\mathbf{x}'$ is the source point, $\mathbf{n}$ is the unit vector in the $\mathbf{x}-\mathbf{x}'$ direction, and $\mathbf{M}$ is the magnetization of the infinitesimal volume d^3x'. The first term in the through space dipole field generated at any point in space is due to a magnetized object. However this integral cannot include the point $\mathbf{x} = \mathbf{x}'$ since the field will diverge. To complete the description, a second term is added to include "contact" with the piece of magnetization at the field point. This contact term is identical to what one finds for the field inside of a uniformly magnetized sphere when performing a surface charge integral; As the sphere volume is decreased, the description becomes a delta function. A comparison of the first term to the second was done to test the possible contribution from an inhomogeneous Rb magnetization.

To perform the numeric integration of the first term in Equation 2.6, a 43x43x43 array

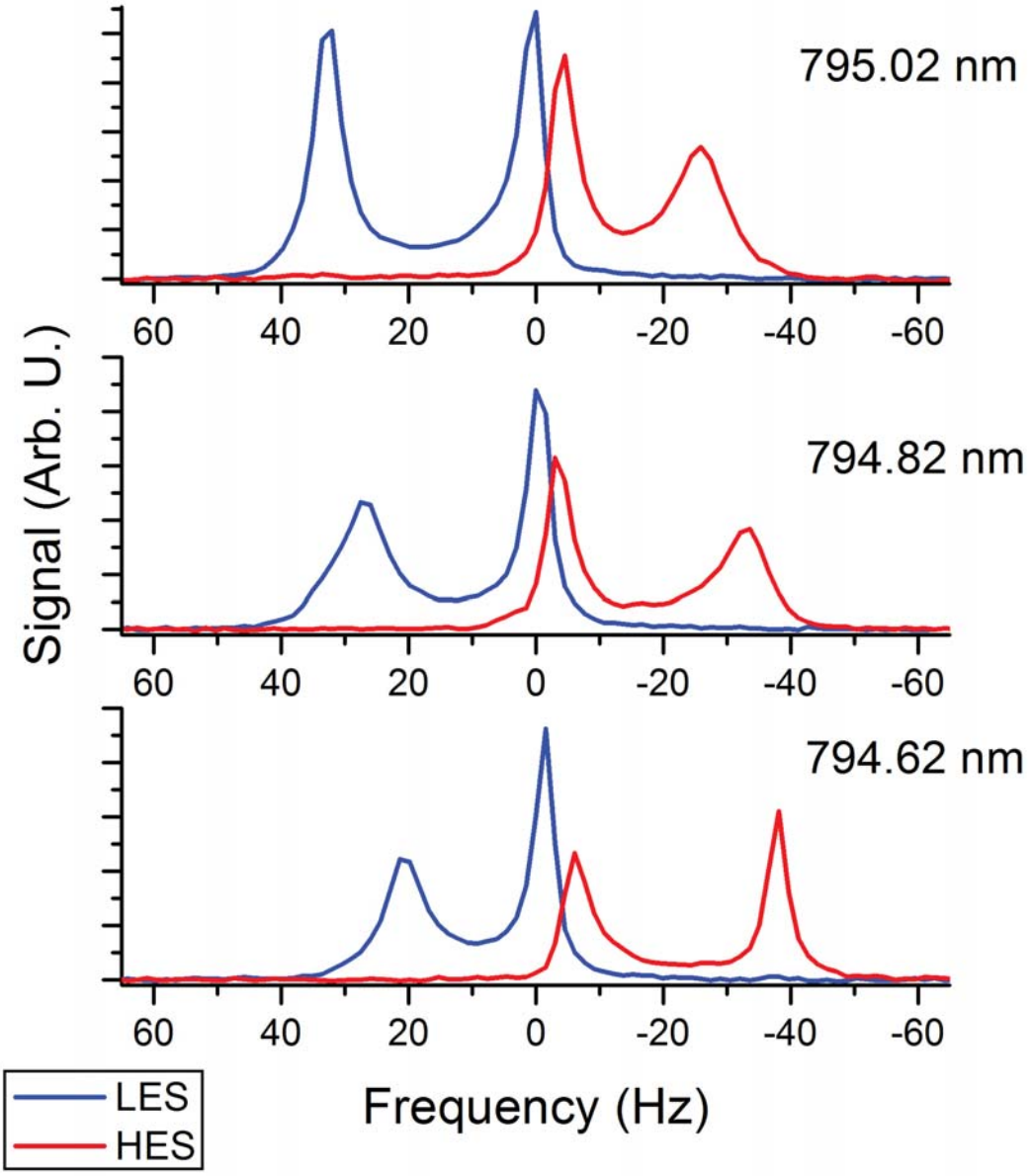

Figure 2.12. Demonstration of the ^{129}Xe spectrum dependence on the pump laser tuning. The wavelength listed on the right is the peak of the laser spectrum viewed on an Ocean Optics Spectrometer, in all cases the laser has a spectral width of ∼0.3 nm FWHM with an approximate Lorentzian/Gaussian lineshape. As the laser is tuned through the D_1 resonance (∼794.7 nm) the HES and LES spectra swap characteristics. This dependence of the ^{129}Xe spectrum on the pump laser tuning is a result of the $\sigma-$ and $\sigma+$ absorption energy being shifted when a Rb atom resides in a 2 T magnetic field.

was set up with the coordinate system origin and center of the sphere placed at the center of the array. A magnetization M = 1 in the Z-direction was assigned to each point with the option to cutoff the magnetization and make it 0 at any point. This roughly simulates the pumping laser magnetizing the Rb and then being quickly attenuated. Then each point was stepped through and the field calculated by summing the contributions from all other dipoles in the array. A series of If-Then statements were used to determine whether magnetization existed at a given point. The X,Y, and Z components at each field point were outputted to a text file and then analyzed. The code used is shown in Appendix B. No susceptibility effect of the glass was taken into account, and the permeability of the sphere was neglected as a dilute gas has essentially zero permeability. Figure 2.13 shows the results.

The numerical modeling is conclusive evidence that the Rb through-space fields can be neglected while analyzing the ^{3}He frequency shift. The through-space effect on the ^{129}Xe can be neglected in all cases because $(\kappa_0)_{\mathrm{RbXe}}$ is two orders of magnitude larger than $(\kappa_0)_{\mathrm{RbHe}}$ (i.e. the second term in 2.6 is large compared to the first no matter what geometry of the Rb magnetization is present).

Additional proof the numeric integral was done correctly is in the lower right figure where the magnetization is cylinder-like. A uniformly-transverse magnetized cylinder has a total magnetic field (inside) of $-2\pi\mathbf{M}$ with a through space field of $-\frac{2\pi}{3}\mathbf{M}$. In the numeric results, the regions of most negative values of field, $B_z \approx -0.1\frac{8\pi}{3}(\kappa_0)_{\mathrm{RbHe}}\mathbf{M} = -\frac{4.8\pi}{3}\mathbf{M}$, which is on order of what is expected for a perfect cylinder.

2.5.6 High Xe Concentration Data

Below $T\approx$175 °C, the data for the high-[Xe] cells (Figure 2.14) are generally consistent with the hatched range (Figure 2.8) that characterizes the low-[Xe] data. However, at the highest temperatures the measured shift ratio drops by about 20%. These 10 or so data points out of 60 acquired for all six cells are at the extremes of high temperature, high [Rb], and rapid Rb spin-destruction (due to higher [Xe]); yet we are unable to connect these physical conditions in a plausible way to the observed systematic depression of the shift ratio. We considered whether fast Rb-^{129}Xe spin exchange might lead to a violation of our fundamental assumption of uniform nuclear magnetization, but this would *increase* the shift ratio by preferentially weighting the regions of higher Rb magnetization in the ^{129}Xe spectrum. We also tested for extreme geometrical effects by remeasuring the shift ratio for both high- and low-[Xe] cells at a given temperature after significantly decreasing the laser

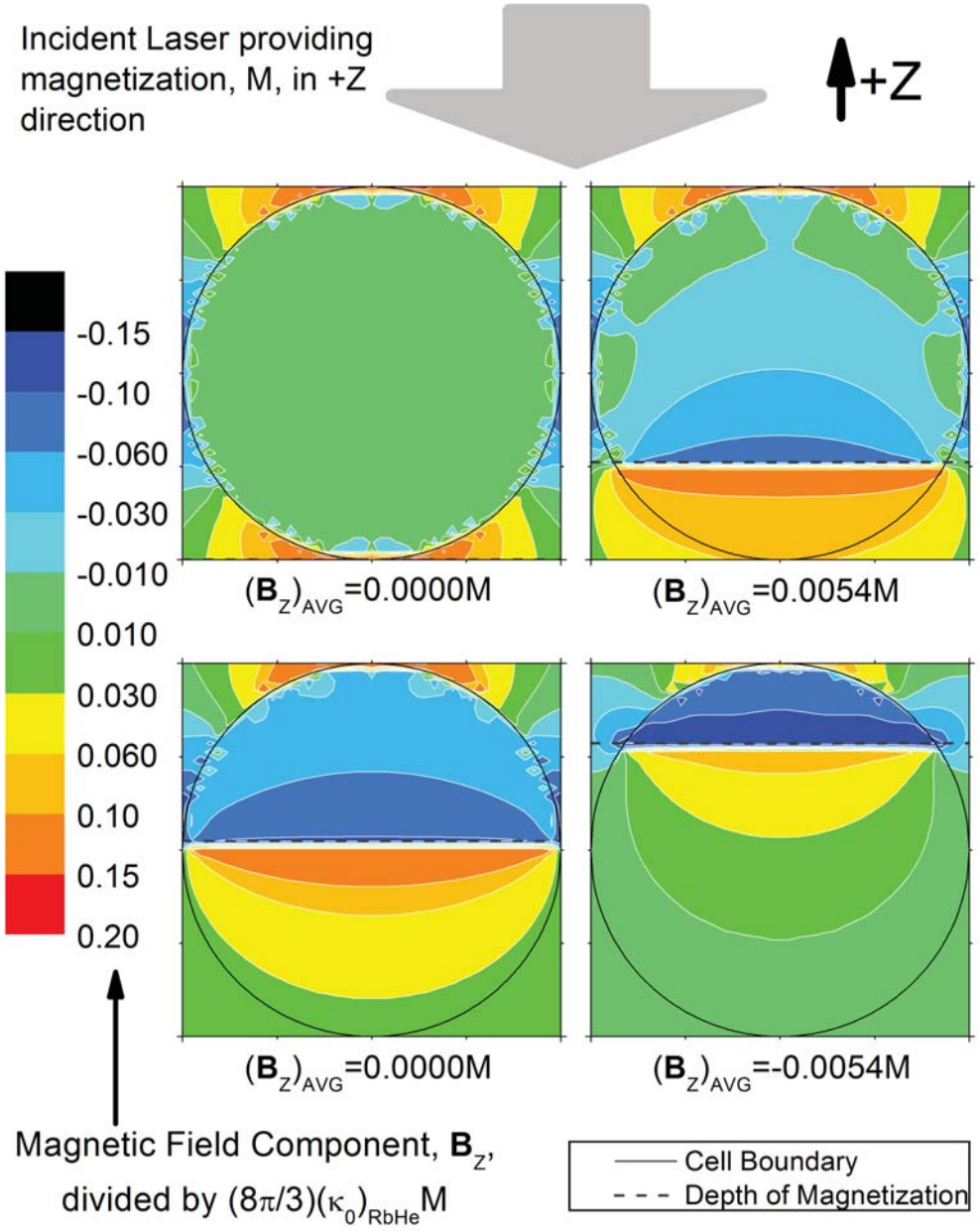

Figure 2.13. Numerical integration of Equation 2.6. All figures are Y-Z slices down the middle of sphere with each showing the through-space field for different depths of magnetization. The colors show the direction and magnitude of B_z only. B_y is not zero throughout this slice, however B_x and B_y both average to zero over the sphere and only the contribution to B_z is the quantity of interest. $(B_z)_{AVG}$ is the average over the entire sphere, not just the slice shown. Even the decidedly nonspherical magnetization distribution show a negligible effect when averaged over a sphere including local regions with 15% deviations from $\frac{8\pi}{3}(\kappa_0)_{\mathrm{RbHe}}$.

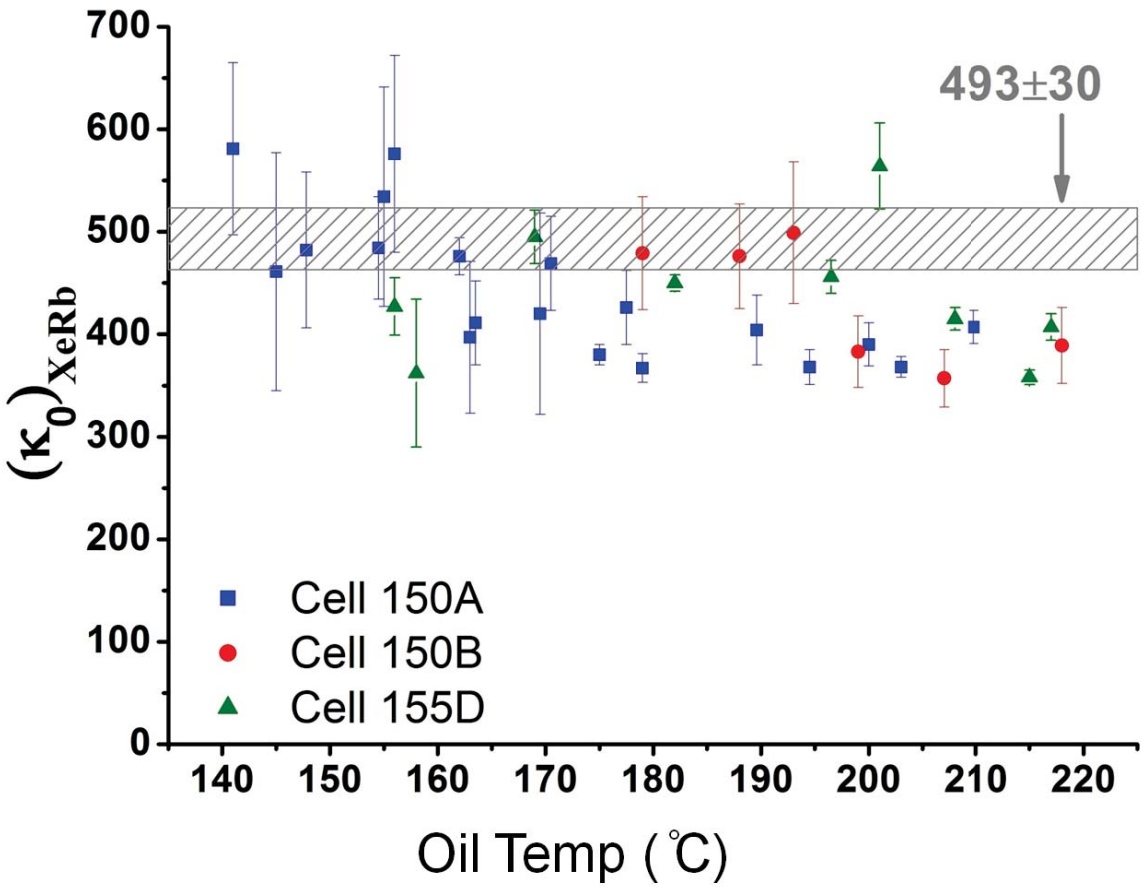

Figure 2.14. $(\kappa_0)_{\mathrm{RbXe}}$ vs. temperature for the high-[Xe] cells. The method used to generate the data points is the same method used in Figure 2.8, and the gray hashed box covers the same area on the graph as in Figure 2.8 as well. These high-[Xe] data are consistent with the low-[Xe] data up to about 175 °C where the ∼20% drop-off at the highest temperatures is not understood.

power. The ^{129}Xe spectrum changed dramatically under these conditions, but the shift ratio was unchanged within error. The anomalous high-[Xe] high-temperature data points were excluded from the main result because they are neither consistent from cell to cell nor consistent with a plausible theoretical temperature dependence (reference [59] calculates a zero or very weakly positive temperature dependence).

2.5.7 Molecular Considerations

Rb-Xe molecular formation can have an effect on ^{129}Xe frequency shifts. Recall the shift is due to a collisionally averaged field seen by the ^{129}Xe nucleus due to spin polarized Rb atoms. If during a collision the Rb electron spin is torqued appreciably (more than a

radian), the average field seen by the ^{129}Xe nucleus will be decreased. The effective field due to formation of Rb-Xe molecule is about 100 G [11] and this experiment was done at 20,000 G. Therefore, the molecular contribution to this experiment is zero for any gas pressure.

Reference [59] presents a very thorough discussion of the molecular contribution to the enhancement factor κ, and only the necessary highlights will be recounted here. The expressions for the alkali and noble-gas frequency shifts (Equations 2.3 and 2.2) contain the enhancement factors κ_{AX} and κ_{XA} respectively, and not the measured κ_0. κ_0 is just the enhancement due to binary collisions between Rb and Xe atoms. κ_{XA} is the complete enhancement factor and takes the form $\kappa_{XA} = (\kappa_0 - \kappa_1) + \epsilon_{XA}\kappa_1$ which includes the contribution from long lived molecules κ_1 and a suppression factor ϵ_{XA}. The reason for the separation of these two enhancement factors is simply to account for the two regimes where calculation is possible: the high-pressure regime defined by κ_0 where, during a collision, the alkali electron-spin evolution angle about the molecular angular momentum is small (much less than a radian), and the low pressure regime defined by a $\kappa_0 - \kappa_1$ where the alkali-spin is torqued significantly during a molecular collision. The suppression factor ϵ_{XA} can vary between 0 and 1, and is a convenient way to treat the intermediate regime when the system is transitioning from a frequency enhancement described by $\kappa_0 - \kappa_1$ to only κ_0.

If the experiment were done at low field (comparable to the molecular field) the frequency enhancement would then depend on the cell pressure relative to the "characteristic pressure." The characteristic pressure is the gas pressure at which the Rb-Xe molecular lifetime is such that the Rb electron spin will, on average, precess by a radian about the molecular angular momentum [59, 74]. Characteristic pressures depend on what types of atoms are forming and breaking up Rb-Xe van der Waals molecules, but all are ∼300 Torr [74]. For reference, when a cell pressure is half of the characteristic pressure, the enhancement factor κ_{XA} is within 1% of κ_0.

2.6 Conclusions

This chapter describes in detail our successful measurement of $(\kappa_0)_{\mathrm{RbXe}}$. This measurement will allow for ^{129}Xe polarization measurements to be done inside of optical pumping cells potentially providing more insight into the physics of spin-exchange between Rb and ^{129}Xe. This additional insight will allow for much more precise optimization of the output ^{129}Xe polarization from modern flow-through polarizers.

Several experimental facts relevant to practical SEOP were also observed. At high magnetic fields, the Rb D_1, $\sigma-$ and $\sigma+$ energies are shifted in energy by a non-negligible amount when using solid-state diode arrays. A 20 °C temperature gradient across ∼1 centimeter was measured when heating the cell with forced air. The ^{129}Xe magnetization does not mirror the Rb magnetization under any of the experimental conditions in this measurement.

Lastly, the results for $(\kappa_0)_{\mathrm{RbXe}}$ from the high-[Xe] cells are very intriguing and no plausible explanation has been put forward at this point. Further experimentation, possibly at lower magnetic fields, is necessary to find an explanation for these data.

CHAPTER 3

^{129}Xe POLARIMETRY USING THE SHIFT OF ^{87}Rb HYPERFINE TRANSITION FREQUENCIES

Many applications of hyperpolarized gas rely on rapid, continuous production of polarized ^{129}Xe [36, 67, 75] where the current state-of-the-art technology is flow-through polarizers [61, 57, 23]. This technology has the ability to provide several (1-10) liters per hour of hyperpolarized ^{129}Xe when the ^{129}Xe is a small percentage (1-3%) of the total gas density. However, all the current designs seem unable increase the ^{129}Xe polarization beyond ∼40% (under reasonable running conditions) for reasons that are not completely understood. A detailed analysis of the ^{129}Xe polarization inside the optical pumping region under different conditions would greatly improve our understanding of the underlying physics and experimental realities of flow-through polarizers.

The previous chapter described the method by which a successful calibration of $(\kappa_0)_{\mathrm{RbXe}}$ was done. This chapter focuses on using $(\kappa_0)_{\mathrm{RbXe}}$ to measure the ^{129}Xe polarization by monitoring the ^{87}Rb hyperfine electron paramagnetic resonance (EPR) frequency while actively optically pumping. A Rb EPR frequency counting apparatus was developed on the Utah flow-through polarizer that fell short of a definitive ^{129}Xe polarization measurement, but produced several interesting and unexpected results. The data collected, while still preliminary, point towards the possibility of probing fundamental atomic physics and is an essential first step for future ^{129}Xe polarimetry measurements.

3.1 Introduction

As stated in Chapter 2 (Equation 2.3) the alkali-metal EPR frequency in the presence of noble-gas is given by the following:

$$\Delta\left|\nu_A\right| = \frac{1}{h}\frac{\mu_B\left|g_s\right|}{(2I+1)}\frac{8\pi}{3}\frac{\mu_K}{K}\kappa_{AX}[X]\langle K_z\rangle. \tag{3.1}$$

This gas-phase shift of the alkali metal EPR frequency is caused by a Fermi-contact interaction between the alkali valence electron and noble gas nucleus experienced during many rapid collisions that result in an average additional magnetic field experienced by the alkali valence electron. For a given noble-gas magnetization, $\frac{\mu_K}{K}[X]\langle K_z\rangle$, the scale of the shift is determined by κ_{AX} and the size of the Rb gyromagnetic ratio, $\frac{1}{h}\frac{\mu_B|g_s|}{(2I+1)}$.

Everything is known in Equation 3.1 except the noble gas magnetization. Therefore, with knowledge of the noble gas density, which is typically known in most optical pumping experiments, and with an accurate measurement of the alkali EPR frequency, the polarization of the noble gas $\frac{\langle K_z\rangle}{K}$ can be determined.

Estimating the size of the alkali EPR shift is instructive for understanding the difficulty of this measurement. Equation 3.1 can be rewritten in terms of ^{129}Xe quantities to be

$$\Delta\left|\nu_{\mathrm{Rb}}\right| = \frac{4}{3}\frac{\mu_{\mathtt{B}} g_{\mathtt{s}}}{(2I+1)}\gamma_{\mathrm{Xe}} K\left(\kappa_0\right)_{\mathrm{RbXe}}[\mathrm{Xe}]\left|P_{Xe}\right|. \tag{3.2}$$

where $I = 3/2$ for ^{87}Rb, $\mu_B = 9.274\times10^{-21}\frac{\mathrm{erg}}{\mathrm{G}}$, $\left(\kappa_0\right)_{\mathrm{RbXe}} = 493\pm31$, $\gamma_{\mathrm{Xe}} = 7393\frac{\mathrm{rad}}{\mathrm{s}\times\mathrm{G}}$, $g_{\mathtt{s}}$ ~2.002, K =1/2, $P_{Xe} = \frac{\langle K_Z\rangle}{K}$ is the polarization of the ^{129}Xe and can vary from 1 to -1, and [Xe] is the Xe gas number density. These values yield

$$\Delta\left|\nu_{^{87}\mathrm{Rb}}\right| \sim 80\mathrm{kHz}\times[\mathrm{Xe}]\times\left|P_{Xe}\right|, \tag{3.3}$$

where [Xe] is now the density of isotopically natural Xe in amagats. For typical optical pumping mixtures of lean Xe concentration (0.01-0.03 amagats), this yields a shift of ~1 kHz at 50% polarization. The ^{87}Rb EPR resonance is about 20 MHz at 30 G so, from the theoretical predictions, the magnetic field must be stable to one part in 10^5, or 300 μG. This is very challenging, but not impossible. For the reader's reference, a high-resolution NMR magnet and spectrometer can typically be stabilized to ~10 ppb, however apparatus of that type are typically at much higher fields (100,000 G) where 10 ppb is ~1 mG.

This experiment has a simple design: Monitor the Rb EPR frequency as function a of the Xe density in order to to back out the ^{129}Xe polarization. The remainder of this chapter will discuss in detail the Utah flow-through polarizer, some theory behind Rb hyperfine structure in a magnetic field, the EPR detection apparatus used, and results.

3.2 The Utah Flow-Through Polarizer

The Utah flow-through polarizer was initially designed and built by Geoff Schrank and resides in the Saam Labs at the University of Utah. My initial graduate work was helping

in a fairly thorough characterization (only lacking the *in situ* ^{129}Xe polarization) of the polarizer which was published in *Physical Reveiw A* [61] and Geoffry Schrank's thesis [60]. In this dissertation I will discuss only the details necessary to understand the work presented. A comprehensive discussion of the flow-through polarizer can be found in the thesis of G. Schrank [60].

The idea behind a flow-through polarizer is to generate a continuous gas stream that is free of alkali metal and contains hyperpolarized ^{129}Xe. This is accomplished by flowing a gas stream containing ^{129}Xe through a polarized alkali-metal vapor that is kept spatially contained by large temperature gradients and gravity. The alkali vapor is highly polarized by continuous optical pumping with circularly polarized D_1 light (see Section 1.1.2), and as the gas flows through the polarized alkali vapor the ^{129}Xe becomes polarized and then remains polarized as it flows into cooler parts of the system where the alkali metal sticks to the glass was leaving an alkali-free gas stream. In addition the optical pumping cell is long ($\sim$1 m) which helps mitigate localized heating by the pumping laser. Localized heating can cause undesirable pockets of very high Rb number density which can cause significant laser attenuation and create regions of unpolarized Rb that will hinder the capability of the device to output maximum ^{129}Xe polarization.

The important experimental features of the polarizer relevant to the measurement of the Rb EPR frequency are: (1) The relative gas composition and total pressure inside the optical pumping cell can be controlled precisely. Mass flow controllers (1.5% full-scale) admit a precise (1.5% full-scale) flow to the input of the optical pumping cell and a pressure regulator (Bellofram T77 506) backed by a vacuum pump controls the pressure inside the optical pumping cell. In addition, a high precision ($\pm$0.01 psi) pressure gauge (Ashcroft) was installed at the optical pumping cell inlet to monitor the pressure inside the cell where the EPR measurements were done. (2) The Xe can easily be cycled into and out of the gas stream which enables comparing the Rb frequency with and without Xe inside the cell. This Xe cycling should have no time-transient effect on the pressure or flow rate as the Xe is a very small fraction of the total gas composition. (3) The optical pumping laser is tunable in frequency about the Rb D_1 resonance, and the power incident on the optical pumping cell can be adjusted, as well (0-38 W). (4) The oven, where the cell is heated, has two windows that run along the optical pumping cell to allow a probe laser to pass through the cell and out the other side transverse to the main magnetic field. (5) The main magnetic field provided by the four hoops is $\sim$27 G. Figure 3.1 shows a schematic of the design as

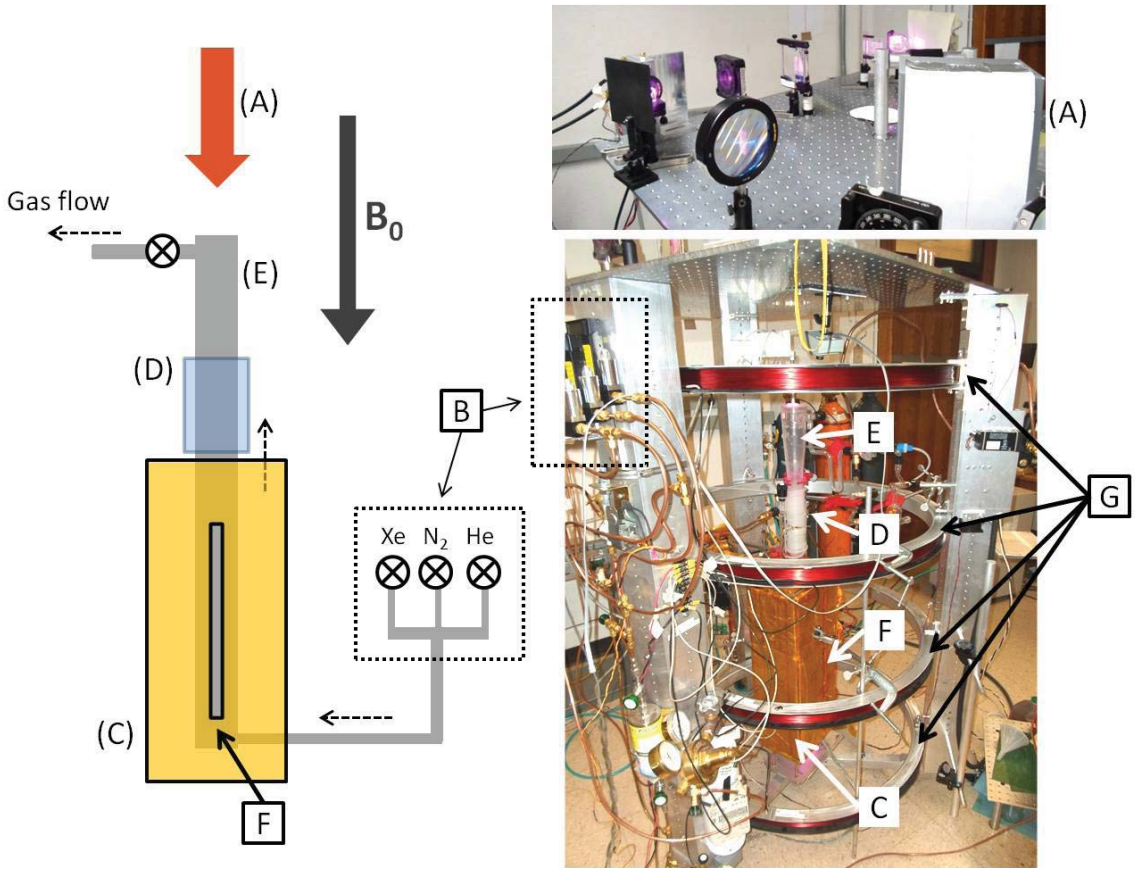

Figure 3.1. Schematic and photograph of the Utah flow-through polarizer. (A) DILAS 50 watt continuous wave 795 nm diode array narrowed with an external Littrow cavity. The laser is circularly polarized, shaped, and then aimed through the pumping cell from the top of the polarizer. (B) Mass-flow controllers (AALBorg) that control the volume flow of a specific gas at room temperature to 1.5% full-scale (C) Forced air oven to drive Rb into vapor phase. This oven is capable of temperatures exceeding 200 °C, but typical running temperatures range from 100-140 °C (D) Water jacket at 16 °C to aid in removing the Rb quickly out of the gas stream and keeping it contained in the oven (E) Cell 156. ∼1 meter long, 4.5 cm diameter optical pumping cell containing ∼1 gram Rb of natural isotopic abundance. (F) 1 cm glass window in oven to admit the probe laser transverse to the main magnetic field and monitor the precession frequency of the Rb atoms. (G) The static magnetic field $\mathbf{B_0}$ is supplied by four, 1 m diameter, 200 turn coils with each adjacent pair satisfying the Helmholtz condition.

well as a picture of the actual polarizer.

3.3 ^{87}Rb in a Magnetic Field

Since the Rb atom will experience, on average, a small additional magnetic field from repeated collisions with polarized ^{129}Xe, the energy of the Rb hyperfine sublevel transitions will change and can be used to measure a small change in magnetic field. The hyperfine sublevel transitions are also experimentally convenient because at ∼30 G, they are distinct and accessible with radio frequency photons.

The calculation of the hyperfine energy levels of an alkali atom in a magnetic field can be done from first principles. The Hamiltonian describing a Rb atom in a magnetic field is

$$\mathcal{H} = \mathcal{H}_e + A_{(SpinOrbit)}\mathbf{L}\cdot\mathbf{S} + A_{(Hyperfine)}\mathbf{I}\cdot\mathbf{J} - \vec{\mu}_I\cdot\mathbf{B} - \vec{\mu}_J\cdot\mathbf{B} \tag{3.4}$$

where $\mathcal{H}_e$ contains all interactions that do not involve spin, $\mathbf{L}$ and $\mathbf{S}$ are the valence electron orbital and spin angular momentum respectively, $\mathbf{J} = \mathbf{L} + \mathbf{S}$, $\mathbf{I}$ is the nuclear spin (^{87}Rb I=3/2, ^{85}Rb I=5/2), and $\mathbf{B}$ is the external magnetic field. If one ignores non-spin dependent interactions and considers the ground state where L=0 and J=1/2 ($5S_{1/2}$ for Rb) then this Hamiltonian can be diagonalized analytically as a function of magnetic field for arbitrary nuclear spin I. This was done in 1931 by G. Breit and I. I. Rabi [13] and the eigenenergies are

$$\frac{E}{h} = -\frac{\nu_{\mathrm{HF}}}{2(2I+1)} \pm \frac{\nu_{\mathrm{HF}}}{2}\left(1 + \frac{2m_{\mathrm{F}}}{I+1/2}\left(\frac{g_s\mu_{\mathrm{B}}}{h\nu_{\mathrm{HF}}}\mathbf{B}\right) + \left(\frac{g_s\mu_{\mathrm{B}}}{h\nu_{\mathrm{HF}}}\mathbf{B}\right)^2\right)^{1/2}, \tag{3.5}$$

where h is Plank's constant, μ_{B} is the Bohr magneton, ν_{HF} is the zero-field hyperfine splitting in Hz, I is the nuclear spin, $g_s \sim 2$, $\mathbf{B}$ is the external magnetic field, m_{F} is the azimuthal quantum number of the atomic angular momentum $\mathbf{F} = \mathbf{J}+\mathbf{I}$, and ± distinguishes between the $F = I + 1/2$ and $F = I - 1/2$ hyperfine manifolds. $\mathbf{F}$ provides good quantum numbers when the applied magnetic field is much less than the hyperfine field (∼1 kG for ^{87}Rb). At much higher fields (>5 kG), product states with quantum numbers m_{I} and m_{J} are the eigenstates that diagonalize Equation 3.4. Figure 3.2 shows a plot of Equation 3.5 as a function of field for ^{87}Rb.

The hyperfine states are denoted by $\langle \mathrm{F}, m_{\mathrm{F}}\rangle$ and the transition between different hyperfine states (denoted hyperfine sublevel transitions) can be written $\langle \mathrm{F}, m_{\mathrm{F}}\rangle \leftrightarrow \langle \mathrm{F}, m_{\mathrm{F}} \pm 1\rangle$. However, this can become cumbersome and the notation convention adopted by almost all of the SEOP literature uses $\bar{m}$, a, and b which are defined in the following way:

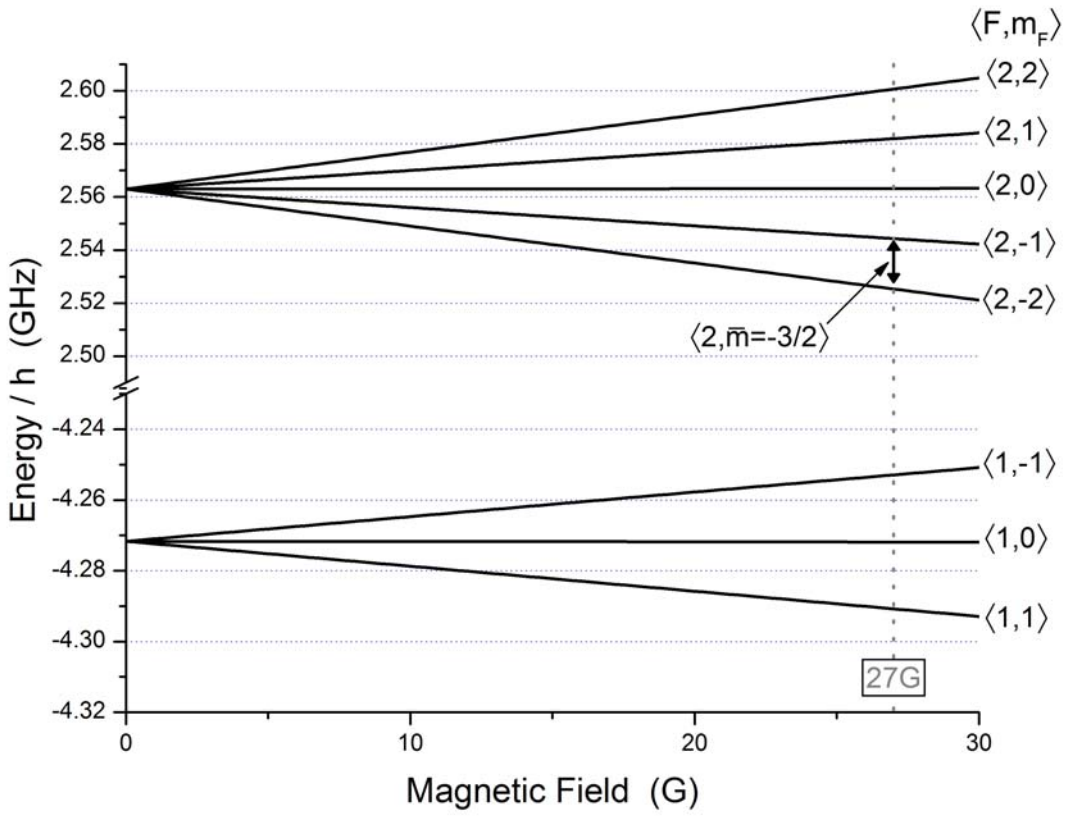

Figure 3.2. ^{87}Rb $5S_{1/2}$ hyperfine structure as a function of field. Each line represents a different hyperfine state denoted by $m_{\rm F}$ with the upper manifold being $F = 2$ and the lower manifold being $F = 1$. The gray dashed line is 27 Gauss where almost all frequency shift data were taken. At 27 Gauss the $\langle \mathrm{F}{=}2, \bar{m} = -\frac{3}{2} \rangle$ transition is $\sim$19 MHz which is easily accessible with lab-built and inexpensive RF equipment. The experiment is to monitor one of the hyperfine transitions and try to detect the small change in energy associated with collisions with polarized ^{129}Xe. The energies in this diagram are all visibly linear, however, when the applied magnetic field is on order of the hyperfine field, the energy levels begin to distort appreciably and become decidedly nonlinear.

$$\bar{m} = m_{\rm F} - 1/2 \tag{3.6}$$

$$\hbar\omega_{f,\bar{m}} = E_{f,m_{\rm F}} - E_{f,m_{\rm F}-1} \tag{3.7}$$

$$f = a = I + 1/2 \tag{3.8}$$

$$f = b = I - 1/2. \tag{3.9}$$

For example, the $\langle 2, 1 \rangle \leftrightarrow \langle 2, 0 \rangle$ transition will be denoted by $\langle 2,\ \frac{1}{2} \rangle$ and edge transitions in the $f = a = I + 1/2$ manifold are $\bar{m} = \pm I$. Edge transitions refer to sublevel transitions that correspond to transitions between the states denoted by $m_{\rm F} = \pm$F and the immediate

adjacent m_{F} state.

The hyperfine sublevel energies computed from Equation 3.5 have a nonlinear dependence on the external field, whereas Equation 3.2 is linear with no dependence on the hyperfine structure. This is because Equation 3.2 is valid only in the regime where the hyperfine states are degenerate (<1 G) and the factor $\frac{1}{h}\frac{\mu_B|g_s|}{(2I+1)}$ is the gyromagnetic ratio for all hyperfine sublevel transitions. The ground-state hyperfine sublevel transition energies can be found for an arbitrary magnetic field by taking the difference between two adjacent m_{F} levels in equation 3.5. However, the experimental magnetic field is ∼30 G, and consequently, the math can be substantially simplified by keeping only the terms linear in $\mathbf{B}$ and expanding the square root to second order in $\left(\frac{g_s\mu_{\mathrm{B}}}{h\nu_{\mathrm{HF}}}\mathbf{B}\right)$. Differentiating the transition energy with respect to magnetic field and multiplying by the ^{129}Xe magnetization results in the alkali EPR shift due to collisions with polarized ^{129}Xe for a specific sublevel transition when the applied magnetic field is much less than the Rb hyperfine field (see Appendix D). Thus, the expression correct to second order in magnetic field for the Rb EPR shift at low magnetic field is

$$\Delta\nu_{\mathrm{Rb}} = \frac{4}{3}\frac{\mu_{\mathrm{B}}g_{\mathrm{s}}}{(2I+1)}\gamma_{\mathrm{Xe}}K\left(\kappa_0\right)_{\mathrm{RbXe}}[\mathrm{Xe}]P_{Xe}\left(1 \pm \frac{4I}{(2I+1)}\frac{\mu_{\mathrm{B}}g_{\mathrm{s}}}{h\nu_{\mathrm{HF}}}\mathbf{B_0}\right). \tag{3.10}$$

As written, Equation 3.10 only applies to the $F = a$ edge-transitions ($+$:$\langle 2, -\frac{3}{2}\rangle$ and $-$:$\langle 2, \frac{3}{2}\rangle$ for ^{87}Rb). Equation 3.10 has been written in terms of the edge transitions because the process of optical pumping continuously adds angular momentum to the alkali vapor; depending on the helicity of light, the Rb atoms accumulate in either the $\langle a, \pm(I+1/2)\rangle$ states. With this accumulation, the EPR signal from the edge transitions dominates the spectrum and provides the peak used to monitor the EPR frequency. Equation 3.10 is identical to Equation 3.2 with a small correction that is 1.7% for ^{87}Rb at 27 G and depends on the strength of the hyperfine field relative to the applied field.

Up to this point, only ^{87}Rb has been discussed. We have neglected the other naturally occurring isotope, ^{85}Rb. $\eta_{87} = .2783$ and $\eta_{85} = .7217$ (NIST) are the naturally occurring isotopic fractions of Rb and consequently the signal from the precessing magnetization will be ∼2.5 times bigger for ^{85}Rb than ^{87}Rb. However, the signal of interest is not the magnitude of the precessing magnetization, but the *frequency* of precession. Since ^{87}Rb has a larger gyromagnetic ratio, for a unit change in applied magnetic field, ^{87}Rb will exhibit a bigger shift than ^{85}Rb.

3.4 Steady State Excitation of Rb Hyperfine Transitions While Optically Pumping

All the other experiments described in this dissertation are pulsed NMR experiments where the goal is to rotate the spins into the transverse plane as quickly as possible and monitor the transverse magnetization via induced voltage in a coil surrounding the sample. In contrast, the experiment here aims to maintain a coherent precession of ^{87}Rb atoms with continuous-wave (CW) RF excitation of hyperfine sublevel transitions and use optical detection to monitor the precession.

As described in Section 1.2.2, the Zeeman splitting of a spin in a static magnetic field can be excited by a transverse oscillating magnetic field at the Larmor frequency. This excitation will torque the spin, and it will precess around the magnetic field resulting from the vector sum of of the static magnetic field, $\mathbf{B_0}$, and the oscillating transverse field, $\mathbf{B_1}$. In the rotating frame when exactly on resonance, the spin simply rotates around the X or Y direction moving between +Z and -Z at the Rabi precession frequency. If the longitudinal relaxation rate $1/\mathrm{T}_1$ is on order of the Rabi frequency, the competition between $\mathbf{B_1}$ rotating the spin off of Z and relaxation mechanisms pushing it back will result in the spin residing at a specific angle with respect to Z. This coherent steady state precessing magnetization will have a component in the transverse direction that rotates at the Larmor frequency and can be described by the Bloch equations.

The classically derived phenomenological Bloch equations, while in general not a completely accurate model of a spin system, provide the correct description for a polarized vapor of ^{87}Rb atoms under steady state RF excitation and various relaxation mechanisms. The rotating frame solutions to the Bloch equations in the limit of a small $\mathbf{B_1}$ field are [64]

$$\begin{aligned} M_X &\sim B_1 \frac{(\omega_0 - \omega)}{\gamma^2 + (\omega_0 - \omega)^2} \\ M_Y &\sim B_1 \frac{\gamma}{\gamma^2 + (\omega_0 - \omega)}, \end{aligned} \tag{3.11}$$

where M is the magnetization, B_1 is the amplitude of the oscillating magnetic field in the X direction, ω_0 is the center of the resonance, ω is the excitation frequency, and γ is T_2-relaxation that defines the width of the resonance. The absorptive (M_Y) and dispersive (M_X) peaks are only 90° out of phase and experimentally either one can be selected. For this reason only the absorptive shape will be discussed. When calculated from first principles using the evolution of the density matrix, the exact solution for the expectation value of

the transverse spin in a 100% polarized Rb vapor under weak-RF excitation takes the same form as M_Y in Equation 3.11. This calculation was published in [2] and takes the form

$$\langle \mathbf{S} \rangle = \frac{g_s \mu_B}{2(2I+1)\hbar} \mathbf{B_1} \frac{\gamma_{a,I}}{(\omega_{a,I} - \omega)^2 + \gamma_{a,I}^2}, \tag{3.12}$$

where $\langle \mathbf{S} \rangle$ is the expectation value of the alkali electron spin, I is the nuclear spin, $\omega_{a,I}$ is the center frequency of the hyperfine sublevel transition defined by $\langle a, I \rangle$, ω is the excitation frequency, and $\gamma_{a,I}$ is the relaxation rate of the resonating hyperfine sublevel. In this case I can be used to denote the hyperfine sublevel transition because Equation 3.12 has been written for edge transitions as the Rb vapor is assumed to be 100% polarized. In reality, the Rb is never 100% polarized and a full treatment can be found in reference [6] for an expression of $\langle \mathbf{S} \rangle$ for arbitrary Rb polarization where the other hyperfine peaks will contribute to the overall spectrum. However, that level of sophistication is not necessary for this discussion.

The linewidths of the hyperfine sublevel transitions are integral to the accuracy of this measurement, because, for a given signal-to-noise ratio, the width of the hyperfine sublevel transition controls the precision of the determination of the peak frequency. The linewidths, without shimming the magnetic field, are dominated by magnetic field inhomogeneities and can render the hyperfine peaks indistinguishable in some cases. The magnetic field was shimmed with a neodymium permanent magnet suspended with a clamp next to the oven. To do this, the hyperfine spectrum was viewed on an oscilloscope while moving the magnet around until the peaks were as narrow as possible, and then the magnet was fixed in place. The advantages of using a permanent magnet for shimming are two-fold. It is simple, and the magnetic field produced by a permanent magnet is very stable.

In absence of magnetic field inhomogeneities, the linewidth for a given hyperfine sublevel transition is determined by the resonance damping rate $\gamma_{f,\bar{m}}$ and is given by [6]

$$\begin{aligned} \gamma_{f\bar{m}} = &\left(\frac{1}{T_{ex}} + \frac{1}{T_{SD}} + R\right)\left(\frac{3[I]^2 + 1 - 4\bar{m}^2}{4[I]^2}\right) - \left(\frac{P}{T_{ex}} + Rs_z\right)\frac{\bar{m}}{[I]}(-1)^{a-f} \\ &+ \left(\frac{1}{T_{FD}} - \frac{\eta \mathcal{Q}_{\bar{m}}}{T_{ex}}\right)\frac{(2f+1)^2 - 4\bar{m}^2}{4[I]^2} \end{aligned} \tag{3.13}$$

where $a = I + 1/2$, $f = I \pm 1/2$, $[I] = 2I + 1$, R is the optical pumping rate where the Rb is being sampled, s_z is the mean photon spin of the pumping laser ($\sim \pm 1$), $\frac{1}{T_{SD}}$ is the S-damping rate, $\frac{1}{T_{FD}}$ is the F-damping rate, $\frac{1}{T_{ex}}$ is the alkali-alkali spin-destruction rate, η is the isotopic fraction of the Rb being excited, $\mathcal{Q}_{\bar{m}}$ depends on the polarization of the

Rb and is the probability that the azimuthal quantum number of the Rb nuclear spin is $\bar{m}$. Each of these relaxation processes and their relevance to this experiment will be discussed in the following paragraphs.

The local optical pumping rate R is given by [71]

$$R = \int_0^\infty \psi(\nu)\sigma_R(\nu)\,\mathrm{d}\nu. \tag{3.14}$$

where $\sigma_R(\nu)$ is the Rb absorption profile, and $\psi(\nu)$ is the incident photon flux defined by the output spectrum of the pumping laser. Numeric estimations of Equation 3.14 range from 10 Hz to 100 kHz [60] depending on the experimental conditions, and consequently this relaxation process can play a major role in the hyperfine sublevel transition linewidths.

$\frac{1}{T_{ex}}$ is alkali-alkali spin destruction rate and will not contribute significantly to the linewidths in this experiment. The gas composition in this experiment was roughly 50% N_2 and 50% He at ∼675 Torr, and at these pressures, the collisional Rb relaxation is dominated by buffer gas collisions [34].

$\frac{1}{T_{FD}}$ is the F-damping rate from interactions that only mix states in a single hyperfine manifold, i.e., $\Delta f = 0$. These type of interactions arise from alkali-buffer gas collisions that are long compared to the hyperfine period, namely Rb-Xe van der Waals molecules formed by three body collisions at low pressures (5-10 Torr). Rb-Xe van der Waals molecules typically live for 10^{-8} seconds [11]. These lifetimes are two orders of magnitude longer than the the hyperfine period in Rb (∼10^{-10} seconds), which means the alkali metal electron can recouple to the nucleus during the lifetime of the collision. The consequence of this recoupling is the two f manifolds cannot mix, and only $\Delta f = 0$ transitions are allowed. The third body is necessary to carry away some of the energy allowing the molecule to form; this process is rare. In reference [59], the maximum value of the fraction of Xe bound in molecules at the deepest part of the van der Waal's potential was calculated to be 13%. The *fraction* of Rb-Xe molecules will not increase with an increase in third body gas pressure, however the *lifetime* of the collisions will decrease as $1/p$, where p is third body gas pressure. At high enough gas pressures (200-300 Torr [74]), all of the collisions become sudden with respect to the hyperfine period, and $\frac{1}{T_{FD}}$ no longer contributes to the hyperfine transition linewidth.

$\frac{1}{T_{SD}}$ is the S-damping rate from interactions which are much faster than the hyperfine period and can mix the hyperfine manifolds during a collisions, i.e. $\Delta f = \pm 1$. At the gas pressures in our experiment (∼675 Torr), this relaxation will dominate over F-damping. In

terms of the Rb electron spin state, the main difference between S- and F-damping is the amount the electron is torqued about the internuclear axis during collisions. During an S-damping collision, the Rb precesses much less than a radian about the molecular angular momentum and the electron will undergo a "random walk" around the Bloch sphere where each collision can be considered a step. In contrast, during an F-damping collision the electron precesses many times about the internuclear axis and is consequently completely randomized after every collision.

Equations 3.13 and 3.12 are calculated under the assumption that the hyperfine populations of the Rb atoms in the optical pumping cell are well defined by a spin-temperature.

$$\rho = \frac{e^{\beta F_z}}{\mathcal{Z}} \tag{3.15}$$

where ρ is the density matrix, $\mathcal{Z}$ is the partition function, and β is the spin-temperature parameter. The spin temperature condition will prevail as long as all of the interactions that the Rb atoms undergo are sudden with respect to the hyperfine period [2]. Once again, for the pressures in our cell, this is always the case.

Neglecting $\frac{1}{T_{FD}}$ and $\frac{1}{T_{ex}}$, the damping rates under weak-CW excitation of the $f = a$ edge states for ^{87}Rb are

$$\begin{aligned} \gamma_{a,\frac{3}{2}} &= .625\frac{1}{T_{SD}} + .25R \\ \gamma_{a,-\frac{3}{2}} &= .625\frac{1}{T_{SD}} + R \end{aligned} \tag{3.16}$$

Unfortunately, no quantitative study of the hyperfine sublevel transition linewidths could have been done since the apparatus in this experiment was designed to sweep/modulate frequency, not field. In theory, this does not matter, but the phase shifter used has a frequency dependent phase-shift that makes quantitative interpretation of the spectra very difficult. Section 3.7.5 has a discussion of spectra acquired during the experiment that depends on both the optical pumping rate and the S-damping rate.

3.5 Alkali Spin Precession Detected via Transverse Faraday Rotation

The Faraday effect is a well-known phenomenon in which the plane of polarization of linearly polarized light is rotated when traveling through a material along an applied magnetic field. For alkali vapor in a magnetic field, Faraday rotation has been extensively

studied and used to measure both alkali number density and polarization [35, 4, 73, 41, 70]. The angle by which the linear polarization rotates due to scattering off of ^{87}Rb atoms is [4]

$$\theta = \frac{[^{87}\mathrm{Rb}]le^2}{6m_e c}\left(\frac{1}{\Delta_{3/2}} - \frac{1}{\Delta_{1/2}}\right)P \tag{3.17}$$

where $[^{87}\mathrm{Rb}]$ is the ^{87}Rb number density, l is path length through through the ^{87}Rb vapor, e and m_e are the electron charge and mass, respectively, P is the ^{87}Rb polarization, and $\Delta_{3/2}$ and $\Delta_{1/2}$ are the differences between the frequency of the linearly polarized light and the D_2 and D_1 resonances, respectively.

In this experiment, the magnetic field remains fixed and the frequency of the excitation is either swept or modulated. As the excitation frequency approaches a hyperfine sublevel transition, the ^{87}Rb atoms will begin to precess about the main magnetic field at the excitation frequency (see Section 3.4). Equation 3.17 has been derived for a longitudinal experiment, however the behavior of the transverse signal can be understood by considering the polarization P to be oscillating at the excitation frequency. The closer the excitation gets to the center of the resonance the larger the amplitude of P will become, and the amplitude of the rotation angle oscillation will increase. The amplitude of the rotation angle oscillation is the signal used to map both the ^{87}Rb hyperfine spectrum and lock to the peak of a resonance.

3.6 ^{87}Rb EPR Detection Apparatus

The electronics that are necessary to detect and accurately measure the ^{87}Rb precession frequency are fairly extensive, and designing, building, implementing, and optimizing the apparatus required many months of effort. This section is a broad overview of the apparatus (Figures 3.3 and 3.4) and the principles of operation. Appendix E contains a complete description as well as pictures and schematics of all the equipment. The equipment described in this section and Appendix E was built on or around the flow-through polarizer described in Section 3.2.

As described previously, the goal of this experiment is to monitor the frequency of a ^{87}Rb hyperfine sublevel transition as a function of ^{129}Xe density. To monitor the ^{87}Rb EPR frequency, a classic locking scheme where a derivative signal is generated from an absorptive peak and is then used as an error signal to adjust the equipment. A CW alternating magnetic field ($\mathbf{B_1}$) at a ^{87}Rb hyperfine transition frequency ($\sim$20 MHz) was applied to the optical pumping cell transverse to the static applied magnetic field ($\mathbf{B_0}$).

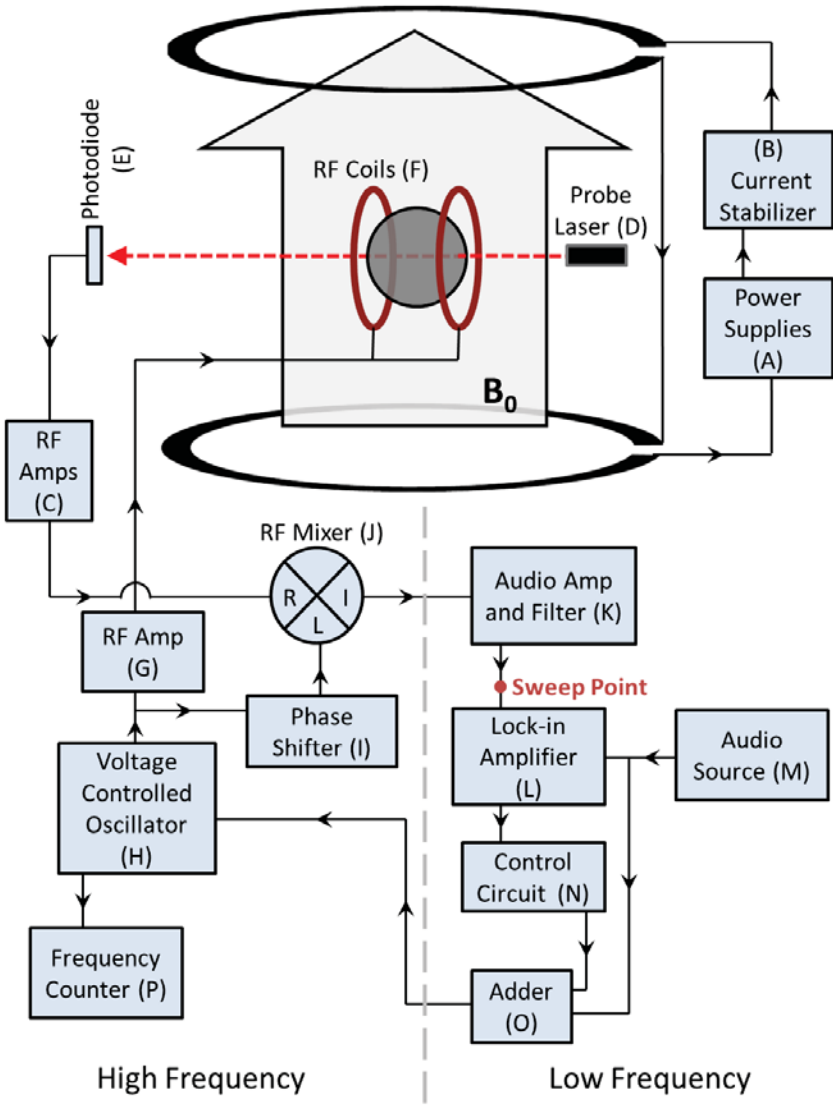

Figure 3.3. Design of electronics to measure a ^{87}Rb hyperfine transition frequency. The schematic is broadly divided into two parts, high and low frequency. The high-frequency ($\sim$20 MHz) provides RF (H,G) to the coils (F) to excite the ^{87}Rb, amplifies the signal (C) from the photodiode (E), and mixes (J) the signal with reference RF (I) to demodulate down to audio frequencies. The low-frequency ($\sim$500 Hz) section amplifies and filters (K) the signal from the mixer (J), feeds this signal into a lock-in (L) referenced to the RF modulation frequency (M) which generates a derivative signal, processes the derivative signal with an analog proportional and integral control circuit (N), and then adds (O) the control voltage to a modulation voltage (M) to be fed back into the VCO. This negative feedback system forces the VCO to output a RF frequency that makes the output voltage of the lock-in (L) zero which corresponds to the zero crossing of the derivative signal or identically the peak of the absorptive signal. The point labeled "sweep point" is where an oscilloscope can be plugged in (instead of the lock-in) with the VCO set to sweep through the hyperfine resonances to generate a hyperfine spectrum (see Figure 3.5).

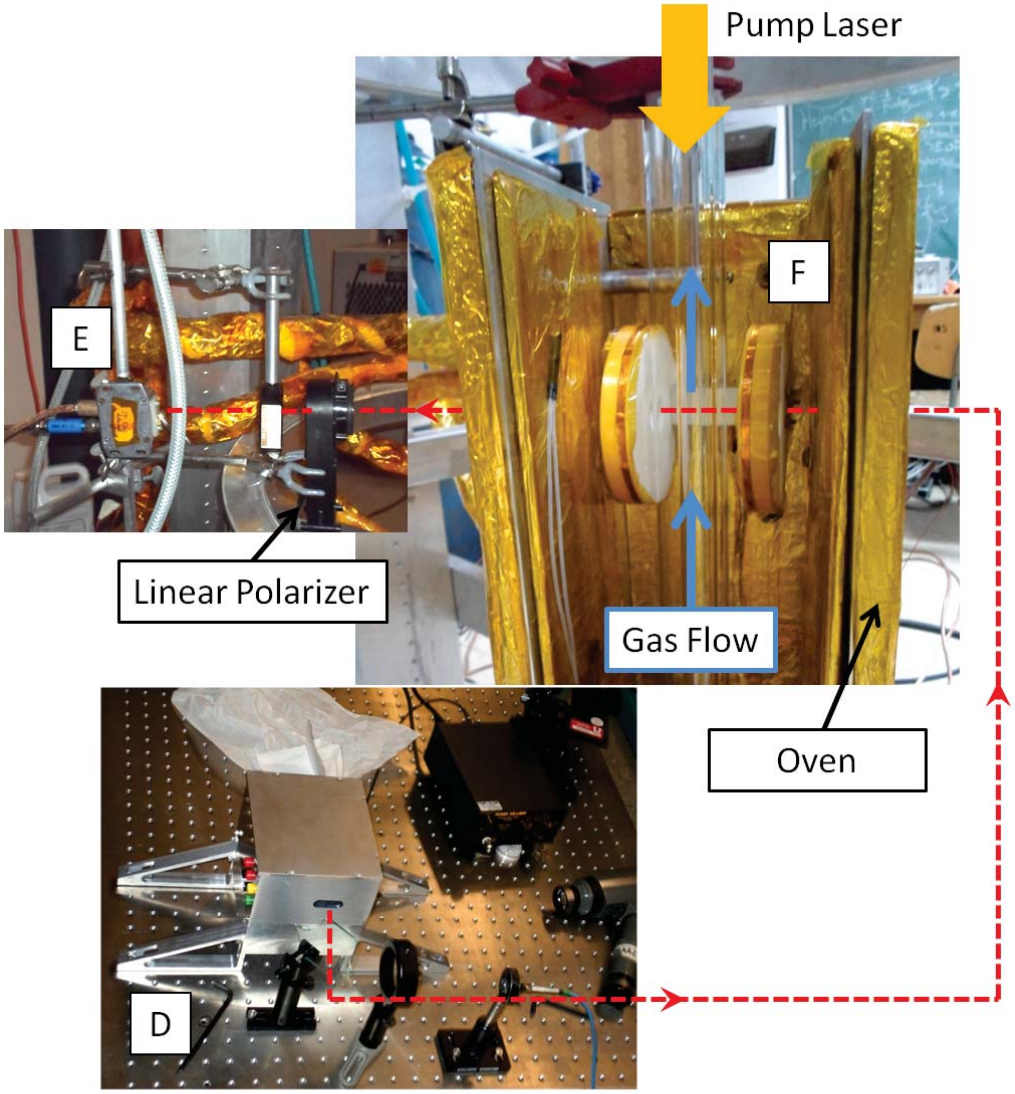

Figure 3.4. Photograph of the inside of the oven on the polarizer where the RF coils (F) excite the ^{87}Rb. The labels are the same as in Table 3.1 and Figure 3.3. The probe laser (D) passes through a hole drilled in the RF coil support, transits the optical pumping cell, passes through a linear polarizer at 45° relative to the polarization of the probe laser, and finally impinges on the photo-diode (E). The aluminum housing in the picture of the probe laser contains both the diode and the diffraction grating to narrow the laser. In addition, the housing helps keep the diode temperature fluctuations low. The region where the probe laser passes through the RF coils and the cell is about 10 centimeters below the top of the oven when it is sealed.

Table 3.1. Components of the EPR frequency counting apparatus.

Label in Figure 3.3	Component and description
A	3 HP6267B DC power supplies in series
B	Home-built current stabilizer
C	RF preamplifiers MiteQ (M/N AU-1467-100KHZ-BNC) followed by a Mini-Circuits ZFL-500
D	Sanyo DL-7140-201S narrow to ∼.1 nm FWMH with an external cavity and detuned ∼1 nm off the D_2 resonance
E	Edmund Optic 54-520 2 nanosecond rise-time photodiode powered by five 9V batteries in series
F	Home-built resonance coils tuned from ∼18-22 MHz
G	Passive variable attenuator followed by RF Amplifier (ZHL-32A)
H	Frequency synthesizer with Voltage Controlled Oscillator input (BK4040A); Note: This thing is a total piece of junk.
I	RF phase shifter (JSPHS-26) followed by RF amplifier (ZFL-500HLN)
J	RF Mixer (ZAD-1-1)
K	Textronix AM502
L	PAR 186A Synchro-Het 5Hz-100kHz
M	Wavetek 1 MHz Function Generator
N	Home-built proportional and integral control circuit
O	Home-built inverting summing junction using an OP27
P	Agilent 53220A to read the output frequency of the VCO as a function of time

This RF $\mathbf{B_1}$ will drive resonant ^{87}Rb atoms into the transverse plane, as described in Section 3.4, resulting in an oscillating voltage at a photo-diode with the same frequency as the excitation. The photo-diode voltage is amplified and demodulated to audio frequency by mixing it with a reference at the excitation frequency. To make the voltage-controlled oscillator (VCO) output a frequency that follows the peak of a transition, the frequency of $\mathbf{B_1}$ was modulated at ∼500 Hz with a modulation amplitude of ∼1.2 kHz. When at a resonance, this modulation of the $\mathbf{B_1}$ RF frequency, when fed into a lock-in amplifier, generates a derivative signal from an absorptive peak. In turn, the derivative signal can be

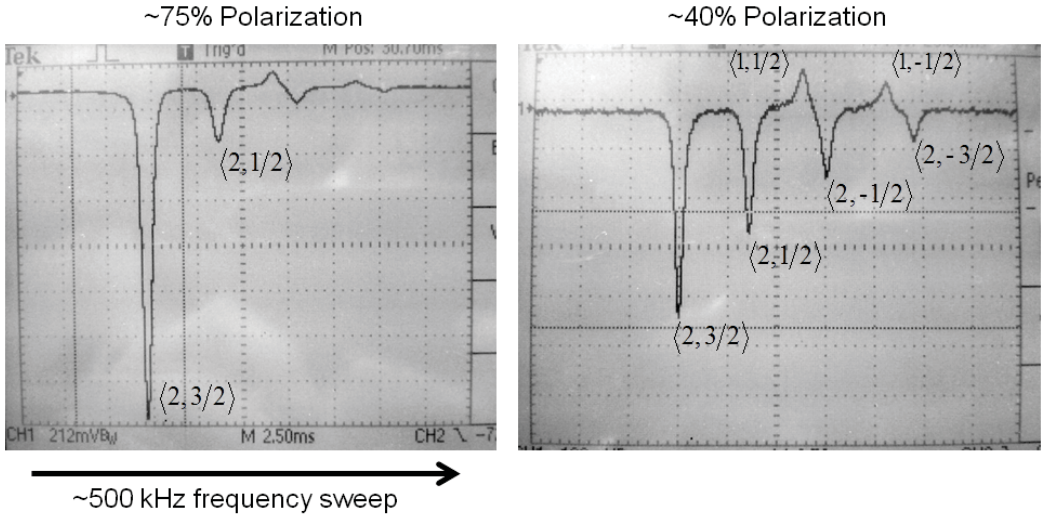

Figure 3.5. ^{87}Rb hyperfine sublevel transition spectra acquired on an oscilloscope using the high frequency electronics and the VCO set to sweep frequency. The transitions are denoted by the $\langle \mathrm{F}, \bar{m} \rangle$ notation described in Section 3.4 and have been identified by computing the transition frequencies from Equation 3.5. Two different polarizations, 75% on the left and 40% on the right, are shown to illustrate the accumulation of spin in the edge states while optically pumping and to verify the correct assumption of a spin-temperature distribution in the two hyperfine manifolds. Each peak was fit to a Lorentzian and the polarization was estimated from the ratio of the area under the $\langle 2,\ 3/2 \rangle$ transition to the area under the $\langle 2,\ 1/2 \rangle$ transition. This procedure to find the polarization is described in reference [6]

used as an error signal to be fed back into the VCO to force the VCO to follow the hyperfine transition frequency. The frequency of the VCO output is then recorded as a function of time on a frequency counter. Figure 3.3 shows a schematic of the electronics designed to do this, and Table 3.1 is a list of the actual components. A complete description of how the locking scheme works is given in Appendix E.

As shown in Figure 3.3 the electronics consist of high and low frequency components. The high-frequency components provide the excitation RF and demodulate the RF signal down to audio frequency. The low-frequency components generate the audio oscillation of the excitation frequency and prepare the error signal to be fed back into the VCO. When using only the high-frequency section with the VCO set to sweep through a range of frequencies, a hyperfine spectrum can be generated by plugging in an oscilloscope to the point label "Sweep Point" in Figure 3.3. All spectra presented in this chapter were acquired in this manner, and two sample oscilloscope traces are shown in Figure 3.5. When using the low-frequency locking equipment, a spectrum cannot be acquired, however the VCO will follow the frequency of a peak to a very high precision (see Section 3.6.1). With proper

filtering and control circuit gain, the noise reduction on the measured frequency was limited by the VCO randomly jumping in frequency by ∼1 kHz, the width of the resonance being measured, and magnetic field noise (which was largely eliminated, see Section 3.6.1).

3.6.1 Simple and Inexpensive High-Current Stabilization with an Inductive Load

As stated in Section 3.1, the applied magnetic field providing the quantization axis for the ^{87}Rb atoms must be stable to better than 300 μG. After successful construction, testing, and optimization of all the other equipment, stabilizing the magnetic field caused much consternation for many months. Early ^{87}Rb EPR frequency measurements showed field fluctuations as large as 1 part in 1000 that were determined to be from current fluctuations in the hoops providing the main magnetic field. Several power supplies were tried in both current and voltage control mode without success. Even an expensive Varian electromagnet power supply designed to run stable current into loads with inductances 100 times the inductance of the polarizer hoops showed similar variation to basic DC power supplies. An attempt was made at stabilizing the current in the polarizer by running the electromagnet and polarizer in series and then using the proton NMR resonance in the electromagnet to stabilize the field in the electromagnet with the hope that the current running through both the magnet and polarizer would be stable. This was also unsuccessful. A magnetometer limited only by the stability of a frequency reference would be the ideal way to stabilize the field, but insufficient time was available to construct a secondary optical pumping setup and frequency measurement apparatus and install it in the polarizer. Commercial magnetometer options were also explored, but they tended to be for low field (<1 G).

A simple and elegant idea suggested by Mark Conradi at Washington University was found to be successful in stabilizing the current from the power supplies. His idea employed a comparator circuit to compare the voltage drop across a shunt resistor to a very stable voltage reference. Figure 3.6 shows the electrical schematic. A power supply, high power FET transistor, and low resistance shunt resistor are placed in series with the polarizer hoops, and the voltage drop across the shunt resistor is measured. This voltage drop is compared to a stable voltage reference and the difference is used to adjust the gate voltage of the FET. By adjusting the gate voltage, the current through the transistor will change, thus changing the voltage drop across the shunt resistor and the current through the hoops.

The limitations on the stability of this design are due to temperature fluctuations of various components and the noise level of the power source of the operational amplifier

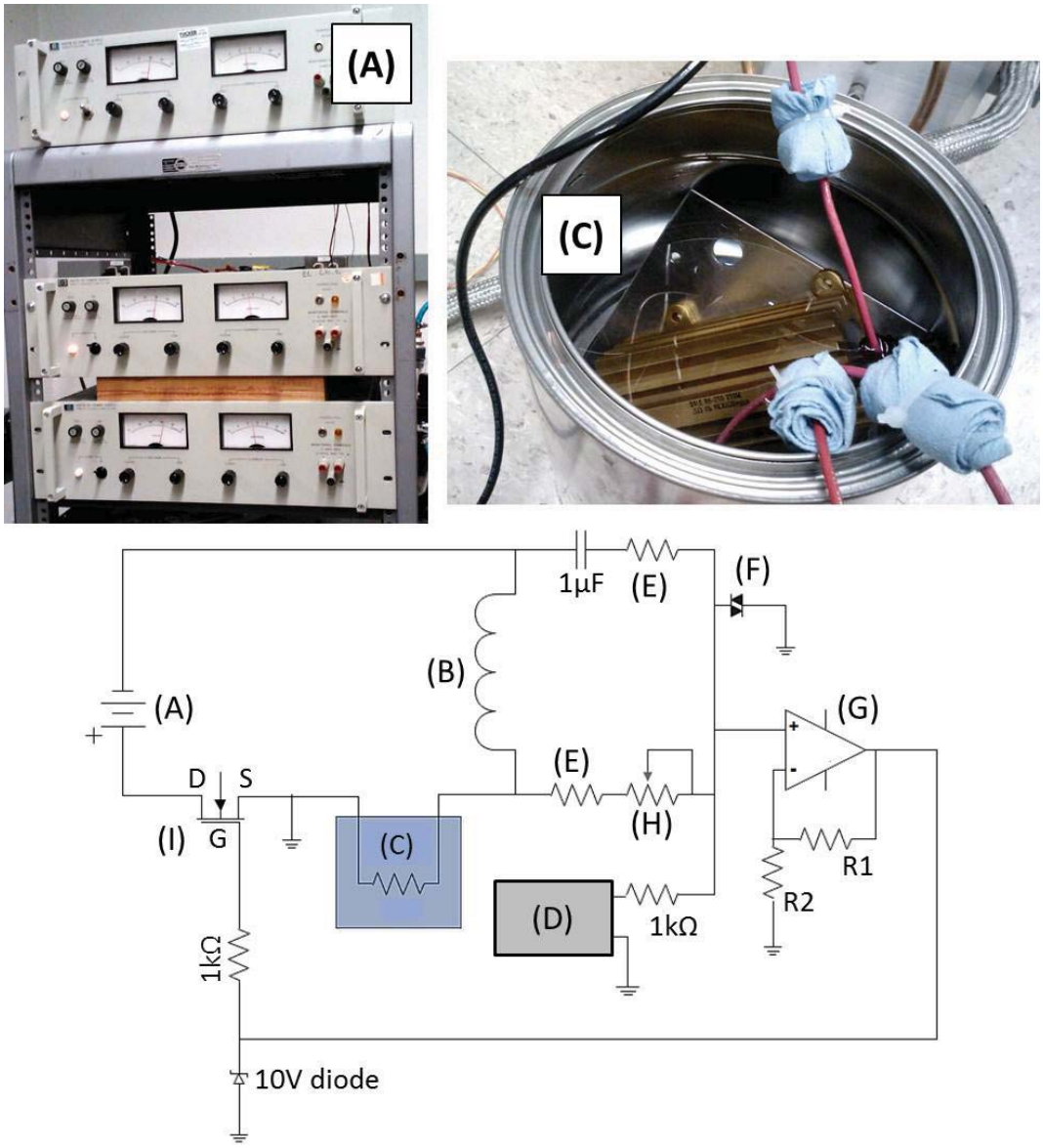

Figure 3.6. Circuit design to regulate the current through an inductive load powered by a DC power supply (A) in voltage control mode. The current control comes from subtracting the voltage drop across the .5Ω shunt resistor (C) from the voltage reference (D) and then using the difference to control the gate voltage of the FET transistor (I). The upper branch with the capacitor is for damping any oscillation from the inductor reacting to a rapid changes in current. This circuit stabilized the current in the hoops to 10 ppm. **(A)** Three HP 6267B DC power supplies in series running about 95 V and 5 Amps **(B)** Hoops of the polarizer **(C)** Paint can filled with mineral oil to keep the .5 Ω shunt resistor (Vishay-Dale 250W, .5 Ω, 100 ppm/°C) from changing temperature **(D)** Voltage (MAX6341) reference with a 1 ppm/°C temperature coefficient **(E)** 500 Ω, 20 ppm/°C, 3 Watt resistor **(F)** Crossed diodes to protect the Op-Amp **(G)** OP27 **(H)** Vishay Accutrim 1240 (0-500 Ω, 10 ppm/°C) used to adjust the voltage drop across the shunt resistor **(I)** High power FET transistor (IRL2910PbF) mounted to a heat sink with a fan.

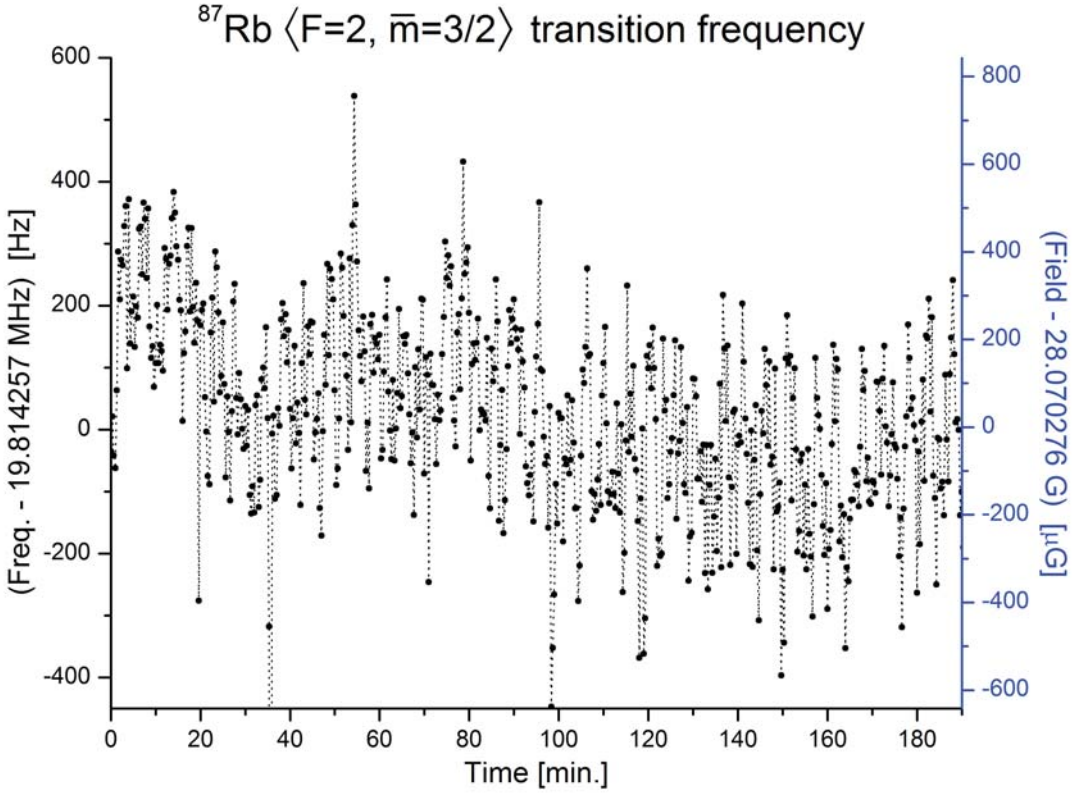

Figure 3.7. ^{87}Rb $\langle F = 2, \bar{m} = 3/2\rangle$ hyperfine transition frequency as a function of time. Each point is the frequency averaged over the previous 20 seconds. The very slow drifts are probably components in the control circuitry changing temperature. The "fast" noise could be a combination of the VCO ouput frequency jumping or drifting, magnetic field fluctuations from other sources in the building, or residual noise from the current regulating circuit. Regardless, the magnetic field with the current regulating circuit is stable enough to measure an ∼600 Hz shift reliably. Polarizer settings: 40 W Pump laser power incident on cell; Oven temperature = 130 °C; Cell pressure = 16.3 psi; Flow Rate = 250 He, 250 N_2, 0 Xe standard cubic centimeters per minute (sccm).

(op-amp). The shunt resistor must have a stable resistance value regardless of the current going through it. This was achieved by placing the shunt resistor in a paint can full of mineral oil (Figure 3.6). The high precision variable resistor and voltage reference must also not change with temperature, and both of these components were chosen carefully to have low temperature coefficients. Various ±15 V power supplies were found to carry too much noise to the op-amp. The noise caused massive fluctuations in the gate voltage that were too big for the circuit to correct. The gate voltage would then drop to zero, periodically shutting off the FET (and the magnetic field since the current drops to zero) for a few milliseconds. To alleviate this problem, the circuit was powered by 12 V batteries.

With the circuit running as expected, the current was stable for hours with ∼350 μG (275 Hz) RMS noise. Figure 3.7 shows the frequency of a ^{87}Rb hyperfine sublevel transition as a function of time for over 3 hours. All of the components of this circuit cost about $200 and can stabilize the current from a DC power supply better than any internal circuitry provided with power supplies in the Saam labs, including several that cost thousands of dollars and one designed to power inductive loads.

3.7 Data and Discussion

Given a stable magnetic field and frequency locking electronics that accurately lock to the peak of a resonance, the ^{87}Rb hyperfine frequency could be observed as a function of [Xe] using the precise control of the mass-flow-controller. This was done several times with the Rb in both the high and low energy states. Representative data are shown in Figure 3.8.

Recall the goal of this experiment is to measure ^{129}Xe polarization with the use of the ^{87}Rb EPR frequency shift. However when adding Xe to the optical pumping cell, many effects exist that can manifest in the form of a ^{87}Rb freuqency shift and greatly complicate the interpretation of the data. Data in Figure 3.8 show four Xe cycles, two cycles while monitoring the $\bar{m} = \frac{3}{2}$ and two cycles while monitoring the $\bar{m} = \frac{-3}{2}$ transition. At first glance, the data are exactly as expected and the shift corresponds to a physically plausible and reasonable ^{129}Xe polarization of ∼60%. However, the physical reason for this frequency shift cannot be due only to collisional interactions with polarized ^{129}Xe for the following reasons.

1. The frequency shift is in the opposite direction when considering whether the collisionally averaged additional magnetic field from polarized ^{129}Xe will add or subtract from the static magnetic field. When pumping into the $\bar{m} = -3/2$ ($\langle 2, -2\rangle \leftrightarrow \langle 2, -1\rangle$) hyperfine transition, the ^{87}Rb vapor is being pumped into the $m_{\mathrm{F}} = -2$ state. The ^{87}Rb electron and ^{129}Xe nucleus both have a negative gyromagnetic ratio, meaning that their magnetic moments are anti-parallel to their spins. If the ^{87}Rb spin is aligned anti-parallel to the applied magnetic field then by spin-exchange so is the ^{129}Xe nuclear spin which results in the ^{129}Xe *moment* aligned parallel with the magnetic field (low energy state). Since the ^{129}Xe moment is aligned with the field when it collides with a ^{87}Rb atom it should *add* a small amount of field to whatever the ^{87}Rb sees. In the data shown in 3.8 the frequency shifts down, not up.

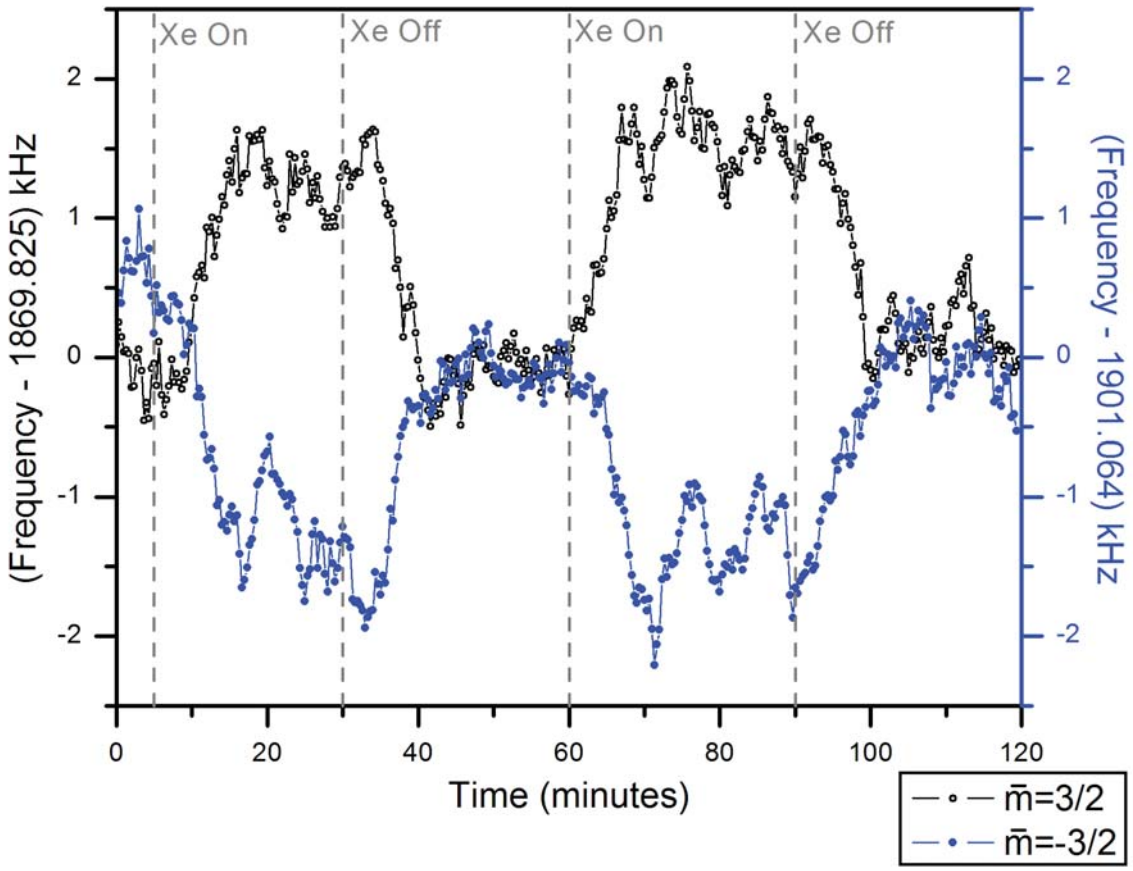

Figure 3.8. ^{87}Rb hyperfine sublevel transition frequency as a function of time when cycling Xe into and out of the gas stream. Each point is the frequency averaged over the previous 20 seconds. The labels of "Xe On" and "Xe Off" indicate the state of the Xe mass-flow controller switch. The shift direction is opposite what is expected given the ^{87}Rb electron and ^{129}Xe nucleus both have negative gyromagnetic ratios. If this shift were due to collisions between ^{87}Rb and polarized ^{129}Xe, the ^{129}Xe polarization would be ∼60%. Polarizer settings: 28.5 W pump-laser power incident on the cell; 110 °C oven temperature; 16.01 psi cell pressure; (370 He, 370 N_2, 0 or 19.3 Xe) sccm flow rate.

A possible explanation for this discrepancy is that a mistake was made when assigning hyperfine sublevel transitions to specific peaks. Identification was done with Equation 3.5 and verified with the literature [6]. This is a highly improbable explanation. It is also worth noting that, to the best of my knowledge, nowhere in the published literature has a measurement been reported where the the state of the Rb population and the polarization direction of the ^{129}Xe were measured independently. The apparatus in this experiment has the capability to directly test both the helicity of the pumping light and the polarization direction of the ^{129}Xe; however, due to time constraints this

measurement was not done.

2. In an experiment almost identical to the one shown in Figure 3.8 a ∼3 kHz negative shift was measured when monitoring the $\bar{m} = -3/2$ frequency during a Xe cycle. The shift direction is the same as the data in Figure 3.8; however, a 3 kHz shift would correspond to an unphysical ∼110% ^{129}Xe polarization.

The first thought might be the measurement of $(\kappa_0)_{\mathrm{RbXe}}$ has a systematic error it it. The output ^{129}Xe polarization of the the polarizer has been measured by thermal NMR reference and solid ^{129}Xe second moment analysis, and both methods indicate the ^{129}Xe polarization is ∼25%. For a shift of 3 kHz to represent a physically meaningful ^{129}Xe polarization, $(\kappa_0)_{\mathrm{RbXe}}$ would have to be about 125. This is not plausible given the frequency shifts presented in Chapter 2. However, the Rb EPR frequency may shift for other plausible reasons discussed in the following sections.

3.7.1 Light Shifts

One of the first experimental observations in 1961 made while optical pumping was the shift of the $\Delta F = \pm 1$, $\Delta m_{\mathbf{F}} = 0$ ground state transition frequency (usually dubbed the 0-0 hf transition) of an alkali vapor as a function of the pumping laser power [3]. Detailed theoretical explanations attribute this effect to "real transitions" [7] and "virtual transitions" [47].

Light shifts due to "real transitions," as the name implies, are shifts due to excitations of the alkali metal atom caused by absorption of a resonance photon. A detailed mathematical description of this effect can be found in reference [2], however it can also be easily pictured with a semiclassical description. Consider an ensemble of Rb atoms that are being excited by resonant RF. This resonant RF is generating a coherent precession where both the electron and nuclear spin are precessing due to a strong hyperfine interaction. If during this precession a resonant photon excites the electron the nuclear spin ceases to evolve any further and when the electron relaxes back to the ground state and some of the original coherence is regenerated, it will always be retarded in phase relative to the Rb atoms that were not excited [2]. The result is light shifts due to "real transitions" are always negative.

Light shifts due to "virtual transitions" result from the AC-Stark shift. The incoming optical pumping light can, of course, be modeled as an oscillating electric field that will in turn oscillate the valence electron of the alkali atom. Since a given transition has a specific oscillator strength, the light shift due to virtual transitions will have a frequency dependence

and a calculation of this frequency dependence was presented in reference [47]. Using data extraction software, the graph of the calculation in [47] of the light shift for ^{87}Rb has been replotted in Figure 3.9. The AC-Stark shift of the Zeeman resonances can be computed as a small additional magnetic field in the Z-direction and is expressed as δH in Figure 3.9. Note that our pumping laser has a width of ∼140 GHz and consequently exceeds the frequency range in Figure 3.9 by several orders of magnitude. This means that changes in overall pump laser *intensity* will not appreciably change the effective magnetic field due to virtual transitions. However, changes in pump laser *frequency* can possibly change the effective magnetic and shift the energy of the hyperfine sublevel transitions.

Testing the effects of light shifts in our optical pumping cell is simple. The ^{87}Rb hyperfine frequency can be monitored while changing the pumping laser power and tuning. Figure 3.10 shows data demonstrating light shifts. As expected for higher laser power, the frequency decreases and is attributed to real transitions. Less expected is the dependency on laser tuning. When detuning the laser either above or below to the D_1 resonance, the penetration depth into the alkali vapor should increase as the photon absorption cross-section will decrease. In turn, this can increase the optical pumping rate at the point in the cell being probed (∼10 cm deep) and should push the EPR frequency to lower values. However, what we see in the data is one side of the D_1 resonance shifts the frequency down, while the other side shifts the frequency up. Unfortunately detuning the laser in this experiment was done by monitoring the fluorescence of the Rb vapor on an IR camera, and not on a spectrometer. Consequently, data indicating what EPR frequency corresponds to which side of the D_1 resonance are not available. However, the fact that the response to detuning is asymmetric is proof that the frequency of the pumping laser, even though its width is 3 orders of magnitude larger than the detuning at which this effect occurs, has an effect on the ^{87}Rb EPR frequency. This is most likely caused by virtual transitions, or the AC-stark effect.

Understanding light shifts is important to understanding possible systematics in a noble gas polarimetry experiment. However, simply eliminating them would be ideal. Light shifts due to the virtual transitions are easily avoided - simply do not tune the laser during a measurement. Light shifts due to real transitions are not so trivial. The photon absorption rate at any point in the cell depends on the photon flux and absorption cross-section. The photon flux is determined by the attenuation of the laser light higher up in the cell. This attenuation is dependent on both the polarization of the light, which should not

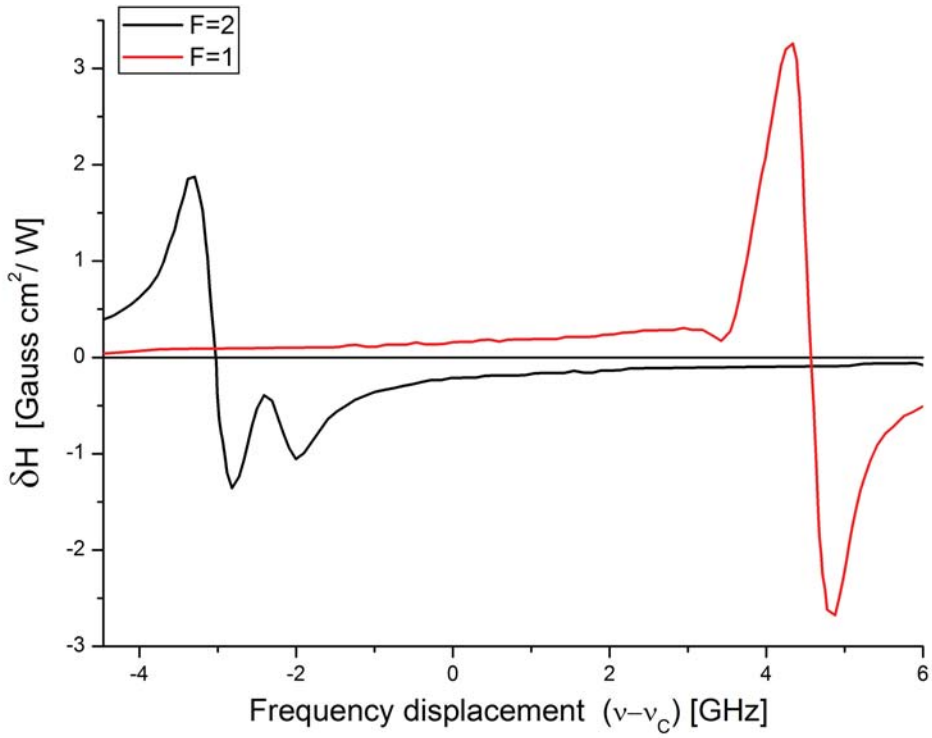

Figure 3.9. Plot of the additional effective magnetic field from the AC-Stark effect from reference [47]. This plot is for ^{87}Rb atom pumped by 794.7 nm D_1 light and the two ground-state hyperfine levels F=1 and F=2 in red and black respectively. ν_c is the center frequency of the D1 transition. Changing the optical pumping power can have a dramatic effect when pumping with intense, spectrally narrow, laser light. However, the width of the optical pumping laser in this experiment is ∼140 GHz, and virtual transitions will have little effect when changing the power. The pumping laser is also frequency tunable, and if the tuning is such that the product of these curves and the pumping laser spectrum change, then a frequency shift can occur.

change during an experiment, and the polarization of the Rb vapor, which strongly depends on the presence of Xe in the gas stream and other relaxation processes. The absorption cross-section is determined by the shape of the D_1 resonance. Therefore, as Xe enters the optical pumping cell, the Rb relaxation rate goes up and the light will not penetrate as deeply into the cell. This will decrease the photon flux and shift the ^{87}Rb EPR frequency up. To avoid this effect experimentally, two things were done. First the temperature of the oven was lowered to 100 °C which reduces the alkali number density and as a consequence increases the penetration depth of the laser. Second, the power on the laser was lowered until the ^{87}Rb EPR frequency no longer changed. The reason for lowering the power is the presence of Xe in the cell will only decrease the photon flux (due to increased Rb relaxation). If a power has been selected such that the frequency does not change with a further decrease

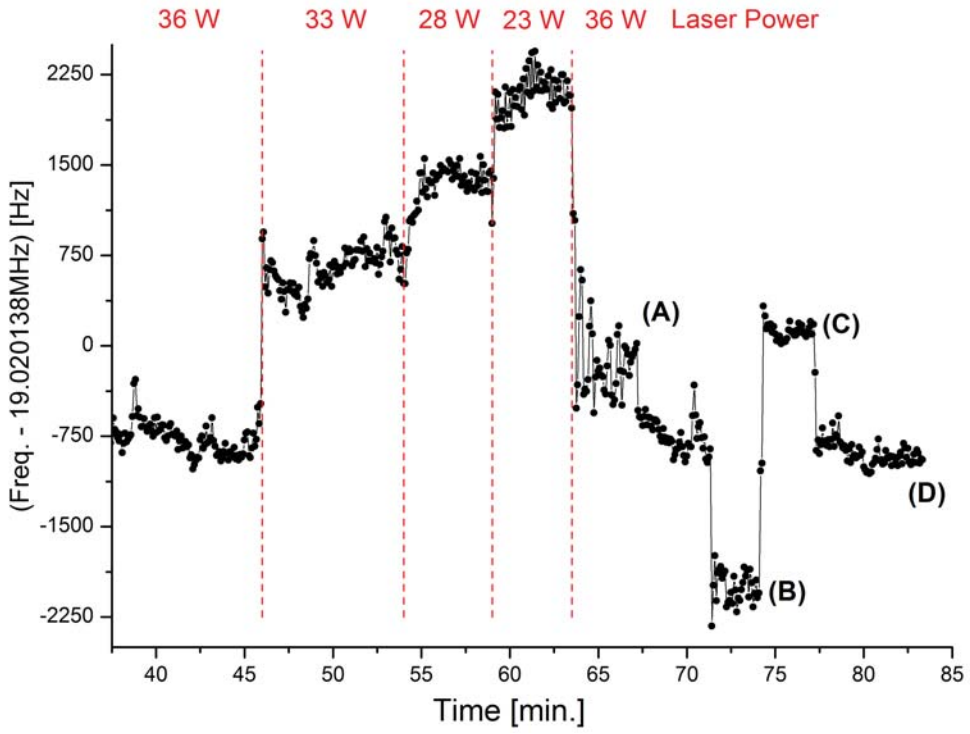

Figure 3.10. Plot of the ^{87}Rb $\langle F = 2, \bar{m} = -3/2\rangle$ hyperfine sublevel transition frequency as a function of time while changing the pump laser characteristics. Polarizer settings: (500 He, 400 N_2, 0 Xe) sccm, 14.3 psi, 130 °C. The red numbers across the top are the power of the pumping laser in watts that is incident on the optical pumping cell and the red vertical lines indicate where this power was changed. **(A)** large fluctuations because the laser temperature was oscillating due to the rapid change from 23 to 36 W. Temperature oscillations will make the intensity at the narrowed frequencies fluctuate. **(B)** Tuned the laser off of "visual" resonance. Visual resonance is the frequency of the laser at which the optical pumping cell has maximum fluorescence (monitored with an infrared camera) **(C)** Tuned off visual resonance to the other side (with respect to **(B)**) of the D_1 resonance. **(D)** Tuned back to visual resonance. The changes in frequency when changing the laser power are most likely caused by real transitions. The changes in frequency when tuning the laser frequency are most likely virtual transitions (AC-Stark shift) since the frequency did not shift the same direction on each side of the D_1 resonance.

in power, then it is safe to assume that addition of Xe will not affect the light shift.

The data in Figure 3.8 were acquired under the conditions explained above to remove any effect of the Xe on the light shift. Therefore the unanticipated shift behavior cannot be due to light shifts and must be explained by something else. While conclusive evidence of the cause of the shift was not found, two more possible explanations are presented in the following Sections, 3.7.2 and 3.7.3.

3.7.2 Alkali-Alkali Spin Exchange

In reference [32], the theory of rapid alkali-alkali spin exchange effecting the frequency and linewidths of alkali magnetic resonances is discussed in detail. Spin-exchange between alkali atoms conserves the total spin of the colliding pair and, therefore, does not decrease the polarization of the vapor. However, if the spin-exchange rate is comparable to differences in the ground state Larmor frequencies then, in a process identical to chemical exchange discussed in Section 2.5.2, the hyperfine frequencies can begin to average together and shift in frequency. Since this frequency shift depends on the Larmor frequencies at higher fields the effect will be diminished. In reference [54] the shift was estimated to be 1500 kHz at 180 °C and 100% Rb polarization. Using the same equation to estimate the shift under our conditions (100 °C, 100% Rb polarization) yields 18 Hz, which is well outside of the sensitivity of this experiment.

3.7.3 Hyperfine Resonance Shift Due to Collisions With Buffer Gas

During a collision between a Rb atom and a buffer gas, the valence electron wave function is disturbed and can consequently change the probability of the alkali electron to be at the alkali nucleus; this will affect the strength of the internuclear hyperfine coupling $\alpha(R)\mathbf{I}\cdot\mathbf{S}$. This change in coupling was first observed in reference [3] and explained in more detail in references [21] and [30]. It is important to note that the collisional process that can effect the hyperfine coupling is also responsible for the frequency shift that is premise for the experiment in this chapter. The difference being that the ballistic disturbance of the valence electron cloud will shift the hyperfine splitting regardless of the polarization of the buffer gas. However, if the noble gas is highly polarized, repeated collisions between the noble-gas and Rb will result in the Rb electron experiencing a small extra magnetic field in addition to whatever disturbance to the wave function is caused by the collision.

The data shown in reference [3] are for a ^{133}Cs vapor, but nevertheless show a very strong dependence of the zero-field hyperfine splitting as a function of gas pressure for different gases. For Xe, the shift is about -2.4 kHz/Torr and for He the shift is about 1.6 kHz/Torr. The reason for the difference between the Xe and He can be understood by the types of potentials governing the collisional dynamics. A He atom has very little polarizability and can be pictured as a hard ping-pong ball that "pushes" the alkali valence electron back towards the alkali nucleus thus enhancing the hyperfine interaction and increasing hyperfine splitting. Xe is the exact opposite. Xe-alkali molecules have an attractive van der Waals

potential with a well depth on order of kT [72], and Xe is highly polarizable. The attractive potential can dramatically increase the interaction time through molecular collisions, and the polarizability makes it much easier for the alkali valence electron to penetrate the Xe electron cloud and be pulled away from the alkali nucleus. These two effects will reduce the hyperfine interaction and decrease the hyperfine splitting. In the data shown in Figure 3.8, the Xe pressure was about 20 Torr, which would correspond to a shift of about -60 kHz. This is a significant overestimate given what the data show but several caveats may exists. First, the measurement in reference [3] was for ^{133}Cs, and the effect will be diminished in Rb. Second, the measured shifts in reference [3] are for the zero field hyperfine splitting frequency (ΔF=$\pm$1 at zero field). What this means for the hyperfine sublevel transitions at a nonzero field is unclear as no literature on the subject could be found. Nevertheless since the gas pressure has a strong effect on the ΔF=$\pm$1 magnetic resonance it could affect the ΔF=0, $m_{\mathrm{F}}\pm$1 transitions as well.

An estimation of the size of the effect on the sublevel transitions frequencies can be done using Equation 3.5. Instead of differentiating the difference between two m_{F} levels with respect to field, the difference can be differentiated with respect to the zero-field hyperfine splitting. The result is not negligible, but small. A 60kHz shift in the zero-field hyperfine splitting will be <10% of the shift due to a 3 mG change in field. However, the data strongly suggest that collisional shifts are not a major contributer: the difference in shift between the $\bar{m} = 3/2$ and $\bar{m} = -3/2$ is clearly dependent on the polarization state of the Xe and the shifts are symmetric. If collisional shifts played a significant role then there would be some offset that is independent of the polarization of the Xe.

3.7.4 Attempts at Destroying the ^{129}Xe and ^{131}Xe Polarization via NMR

Another way to deduce the shift caused by interactions that depend on the polarization of Xe would be to purposefully destroy the Xe polarization while watching the ^{87}Rb EPR frequency. To this end, a Litz wire Helmholtz pair (25x12 turns) with a separation of $\sim$5 cm was constructed and placed inside the RF excitation coils. Recall, the magnetic field in this experiment is $\sim$27 G, and Xe NMR resonances at this field are 9.4 kHz for ^{131}Xe and 31.7 kHz for ^{129}Xe. At these audio frequencies, tuning the coils is not necessary and oscillating magnetic fields as large as 1 G could be generated with direct output from a Stanford Research Systems frequency synthesizer. Pulsed NMR gated with an Aires (Tecmag) NMR spectrometer was also used.

The attempt at destroying the Xe polarization yielded inconclusive results. While the audio NMR was transmitting into the cell, shifts in the ^{87}Rb EPR resonance were observed that depended on the audio frequency and oscillating field strength. The frequency shifts were not always reproducible, which indicated a possible phase dependence of the audio frequencies with respect to some parameter not considered. Continuous wave NMR induced the most dramatic EPR shifts, but pulsed NMR showed strange effects such as the EPR frequency oscillating by more than 1 kHz with a period that depended on the time between pulses.

These results are not entirely unexpected because the magnetic fields required to nutate nuclear spins 90° in a reasonable time period (say less than 10 ms) are a non-negligible fraction of the static field at 27 G. 10 kHz is very slow compared to all the relevant atomic frequencies in the system. By transmitting a 0.5-1 G oscillating magnetic field into the sample, a complicated time-dependent effective field for the ^{87}Rb to precess about will be generated, significantly complicating the ^{87}Rb hyperfine resonance measurement.

3.7.5 Hyperfine Transition Linewidths During Frequency Shift Measurements

Lastly, the ^{87}Rb hyperfine sublevel transition linewidths under polarizer conditions similar to the data shown in Figure 3.8 will be discussed. As explained in Section 3.4, the width of the sublevel transitions will be dominated by S-damping and local optical pumping rate. Both of these effects are apparent in the spectra shown in Figure 3.11.

The linewidths behave as expected. The $\langle F = 2, \bar{m} = -3/2 \rangle$ transition visibly narrows with less pumping laser power (lower optical pumping rate) and broadens under the addition of Xe (faster S-damping). An unexpected result was the addition of Xe did not appreciably change the Rb polarization. In unpublished data from the experiment presented in reference [61] ^{85}Rb hyperfine transitions were observed to narrow under addition of Xe into the cell under certain conditions. The reason for this difference in behavior is the Xe was typically a much lower fraction of the gas composition in reference [61], resulting in the linewidths almost always being determined by the optical pumping rate.

3.8 Conclusions

At the time of writing, this chapter presents the first known attempt at ^{129}Xe polarimetry inside an optical pumping cell without the use of an NMR reference. The theories of generating coherent precessing ^{87}Rb spins colliding with polarized ^{129}Xe and detection using

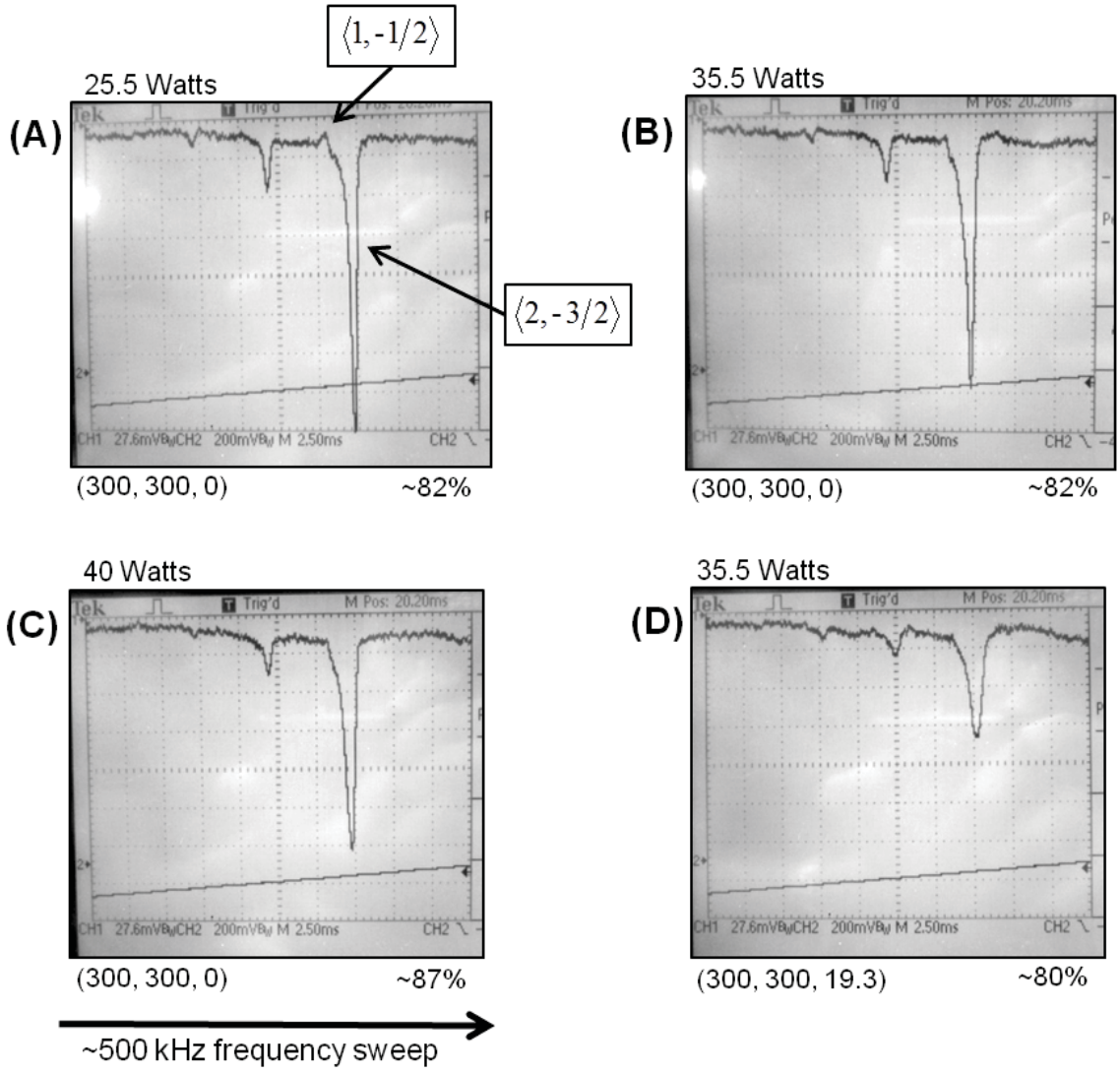

Figure 3.11. ^{87}Rb hyperfine sublevel transition spectra under different pump laser powers and Xe gas densities. All of the spectra have a 500 kHz sweep window with a central frequency of ∼19 MHz. The transitions are denoted in (A) with the $\langle F, \bar{m}\rangle$ notation. The numbers in parentheses below each spectrum are the flow rates of (He, N_2, Xe) in sccm with the pressure inside the cell at 15.8 psi. The polarization estimates should be used as a qualitative guide only, because the data were extracted from the photographs with data extraction software, and the $\langle 2, -3/2\rangle$ transition is heavily shaped because of filters in the system. The background is indicative of RF pickup on the signal line from the photo-diode. Note that the peaks broaden as expected at higher pumping laser power because the optical pumping rate increases with pumping laser power. At 40 W (C) the $\langle 2, -3/2\rangle$ resonance is so broad, the $\langle 1, -1/2\rangle$ transition is covered. In (D), with Xe present in the cell the linewidth increases due to more rapid S-damping relaxation from collisions with Xe.

transverse Faraday rotation were discussed along with the necessary equipment and some initial experimental results that demonstrate a frequency shift in direct contradiction to theoretical predictions. With respect to the ^{129}Xe polarization, the results were inconclusive due to unanticipated difficulties identifying the ^{87}Rb hyperfine sublevel resonance frequency behavior under various optical pumping conditions. However, progress was made in understanding the effects that optical-pumping laser power, alkai-alkali spin-exchange, and buffer gas collisions could have on the ^{87}Rb sublevel Zeeman transition frequencies. In addition, the hyperfine sublevel transition linewidths were discussed along with supporting data. The frequency counting apparatus potentially has the precision to accurately map the frequency dependent light shift with a more spectrally narrow pump laser and the hyperfine sublevel transition linewdiths have the possibility to provide insight into the Rb S-damping rates for various gas mixtures. Future versions of this experiment should use a triple demodulation scheme with two identical VCO's for improved signal to noise, a magnetometer to stabilize the field, and careful, systematic studies of the ^{87}Rb EPR frequency under various conditions to more clearly to delineate the effects discussed.

CHAPTER 4

MEASUREMENTS OF FROZEN ^{129}Xe T_1 RELAXATION

Chapter 3 presented a prototype for an apparatus to measure the ^{129}Xe polarization inside an optical pumping cell along with supporting data. A method to accurately measure the ^{129}Xe polarization has the potential to be a powerful tool for optimizing flow-through polarizers in order to obtain the highest possible ^{129}Xe polarizations. However, the question of how to effectively separate the Xe from other buffer gases without losing an appreciable amount of ^{129}Xe polarization is still open. The method used in all current flow-through polarizers is cryogenic separation. Cryogenic separation is accomplished by flowing the gas-stream from the polarizer outlet through a condenser that is immersed in liquid nitrogen (LN_2). The Xe freezes to the walls and forms crystallites, while the He and N_2 are evacuated with a vacuum pump into to atmosphere. The factor limiting the amount of polarized ^{129}Xe that can be accumulated in the solid phase is the longitudinal relaxation time T_1. Thus, Understanding the physics of this relaxation process is important when designing cryogenic separation systems.

The Saam Lab has made the most reproducible and precise measurements of frozen ^{129}Xe T_1 relaxation times to date leading to the discovery of a difference in T_1 between Xe "ice" and "snow". This dissertation contains a short review of previous work, the apparatus and methods used int he Utah experiment, and preliminary results.

4.1 Introduction

The longitudinal relaxation of ^{129}Xe in a crystalline Xe lattice has been extensively studied. In 1990, Cates *et al.* [16] published the first experiments in which measurement were made of ^{129}Xe relaxation in frozen Xe. Extraordinarily, the results yielded a T_1 relaxation time at 77 K of only ∼2.5 hours instead of the predicted time of weeks to months. The exceptionally long predicted relaxation time is rooted in the Debye temperature of Xe, which is ∼55 K [42]. At 77 K and 2 Tesla, only a very small fraction of the phonon

spectrum is available to modulate the magnetic dipole-dipole interaction at the ^{129}Xe Larmor frequency [51]. The much more rapid relaxation times reported in reference [16] were immediately hypothesized to be caused by the spin-rotation interaction [28]

$$\mathcal{H}_{sr} = \gamma_I \mathbf{I} \cdot \mathbf{N}. \tag{4.1}$$

In Equation 4.1 γ_I is the coupling strength, $\mathbf{I}$ is the nuclear spin of the ^{129}Xe, and $\mathbf{N}$ is the relative angular momentum between a pair of neighboring atoms. If the relative angular momentum $\mathbf{N}$ is mediated by a two-phonon scattering event instead of one, then only the difference between the two phonon frequencies has to fall in the linewidth of the ^{129}Xe NMR resonance to induce spin flips. Consequently, two-phonon scattering includes much more of the phonon spectrum that is capable of modulating the angular momentum $\mathbf{N}$ close to the ^{129}Xe Larmor frequency. Mediation of the spin-rotation interaction by two-phonons has been dubbed the "Raman spin-phonon" scattering process.

The theory of the Raman spin-phonon scattering process relaxing frozen ^{129}Xe is explained in detail in reference [27] and has been verified in solid Xe experimentally by measuring ^{129}Xe relaxation as a function of temperature from 50-160 K [42]. However, the theory and experimental results in the aforementioned references have several caveats. The theory assumes a face-centered cubic (FCC) lattice of solid single-crystal Xe containing a large number of coherent units cells compared to the interatomic spacing. The reported experimental results at 77 K and 0.18 Tesla exhibit a 27% variation (116 to 159 minutes) in the measured T_1 times. Furthermore, all of the measured relaxation times [42] are *slower* than what the Raman spin-phonon theory predicts, indicating that either the fundamental assumptions or the parameters used are incorrect.

The data in this chapter, in addition to being the longest relaxation rates to date, demonstrate a vast improvement over the reproducibility of the results in [42] and show, for the first time, a difference in the longitudinal relaxation rate that depends on how the Xe sample is prepared. If a gas stream containing a low partial-pressure of Xe ($\sim$1%) is passed through glassware at 77 K, the Xe will freeze and stick to the wall, and the other gases will continue unimpeded. The remaining solid Xe that is stuck to the container walls is white to the human eye. The accepted lore among researchers who work with Xe is the white appearance is caused by Xe forming a polycrystalline sample where each crystallite is on the order of microns in size. This freezing of low partial-pressure Xe directly out of a gas stream is what will be referred to as Xe "snow" throughout this chapter. The accumulated

Xe snow can be warmed up past the Xe melting point to form a liquid and then refrozen to form Xe "ice". Xe ice is clear to the human eye. No theory has been developed to explain the difference in ^{129}Xe relaxation times between ice and snow at this time, but the observed difference is a reasonable explanation for the variation seen in all previous solid ^{129}Xe relaxation studies.

4.2 Apparatus

The precision and reproducibility of the measurements presented in this chapter stem from the reliability of the ^{129}Xe NMR probe that was constructed as part of this dissertation to freeze Xe from the output of the flow-through polarizer (Section 3.2). The ^{129}Xe T_1 measurements typically lasted for 8+ hours, and consequently the NMR probe had to be completely stable over the entire course of the measurement regardless of temperature. In addition, in order to make Xe ice reliably, the Xe needed to be warmed and cooled in a controlled manner where both the Xe temperature and the ^{129}Xe NMR spectra could be monitored continuously.

The design of the probe is most efficiently explained with diagrams and pictures (Figures 4.1 and 4.2). However the concepts used to ensure the needed stability and functionality will briefly be described here.

Flowing LN_2 into the bore of a superconducting magnet for over 8 hours will eventually cool the magnet bore. As a consequence of this cooling, any noncryogenic capacitors inside the magnet core will change their capacitance, which can affect the frequency response of the NMR probe. In addition, the hoses and connections to the cryostat had a tendency to shake and shrink as they cooled off and froze. To address these issues, a custom Pyrex cryostat was designed that had a thick vacuum on two of three sides, and a rigid brass holder was constructed to hold the cryostat in place. The LN_2 flowed to the cryostat in a stainless-steel vacuum transfer tube from a pressurized LN_2 dewar. The combination of the vacuum sealed cryostat and vacuum transfer tube kept the brass holder above 0 °C throughout the measurements. Keeping the brass holder relatively warm has two important experimental reasons. First, brass has a relatively high thermal conductivity, and if the brass gets cold, it conducts heat away from the cryostat and reduces the LN_2 cooling capacity. Second, and more importantly, the capacitors that tune the NMR probe are mounted in an aluminum box that was attached to the brass holder for rigidity. While the vacuum transfer line and cryostat did an excellent job keeping the brass holder and capacitors from

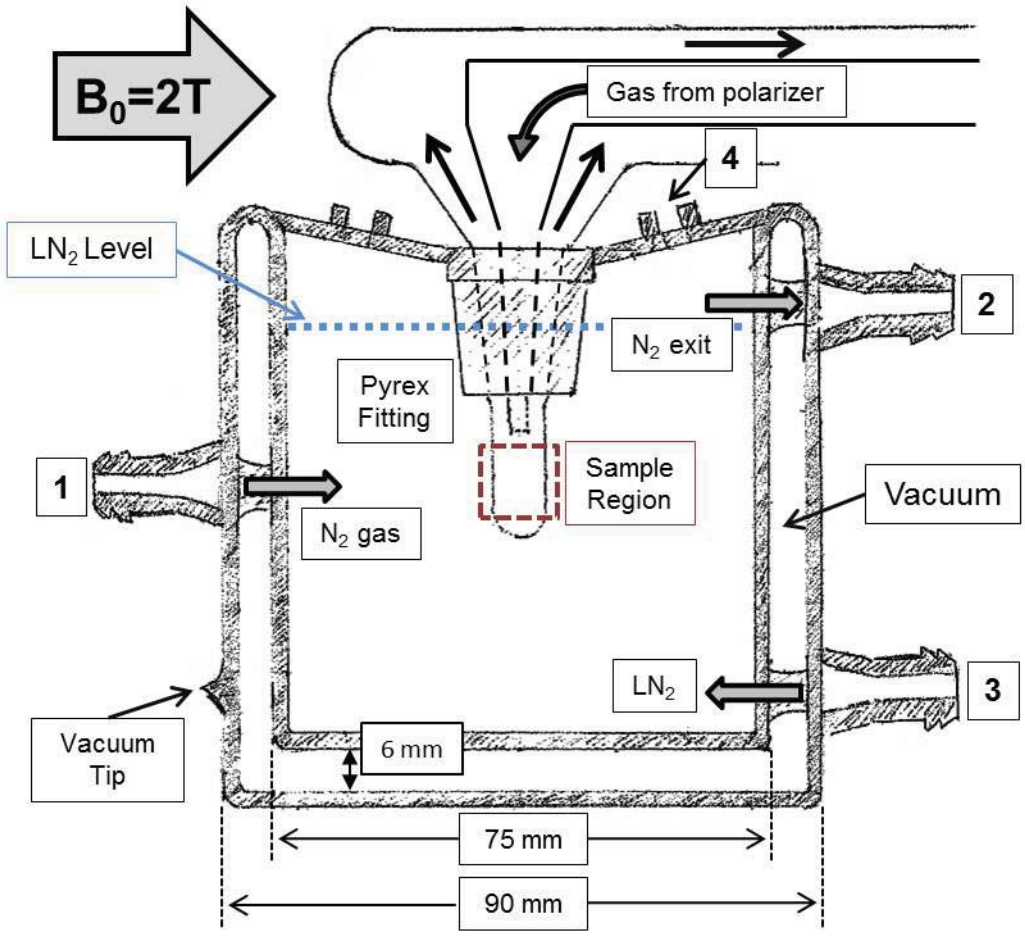

Figure 4.1. Schematic of the Pyrex condenser/cryostat used to measured frozen ^{129}Xe T_1 relaxation times. The basic concept is to flow gas from the flow-through polarizer into a condenser that is married with a Pyrex fitting to a cryostat containing LN_2. The tip of the condenser (i.e., the sample region) is where the gas flow first comes into contact with the outer walls of the condenser which are held at 77 K with a steady flow of LN_2 in the cryostat. Xe will freeze to the outer walls of the condenser while the other buffer gases (He and N_2) continue back to the vacuum pump on the polarizer. The cryostat is a cylindrical vacuum jacket with three Pyrex hose barbs (**1**-**3**) that have connections through the vacuum into the cryostat. The vacuum is closed at the top of the cryostat where a circular piece of Pyrex connects to the fitting where the condenser is attached. Two holes were made (**4**) to admit the wires for the NMR coil and resistive thermal device (RTD) into the interior of the cryostat. **1** was connected to a bottle of N_2 gas and was used to warm the sample when preparing Xe ice. The LN_2 was admitted through **3** with the intent that the cryostat had to fill up before any LN_2 could escape out of **2**, thus ensuring the sample region was completely immersed in LN_2. The NMR coil was wrapped around the condenser tip and then both the RTD and NMR coil were epoxied to the sample region.

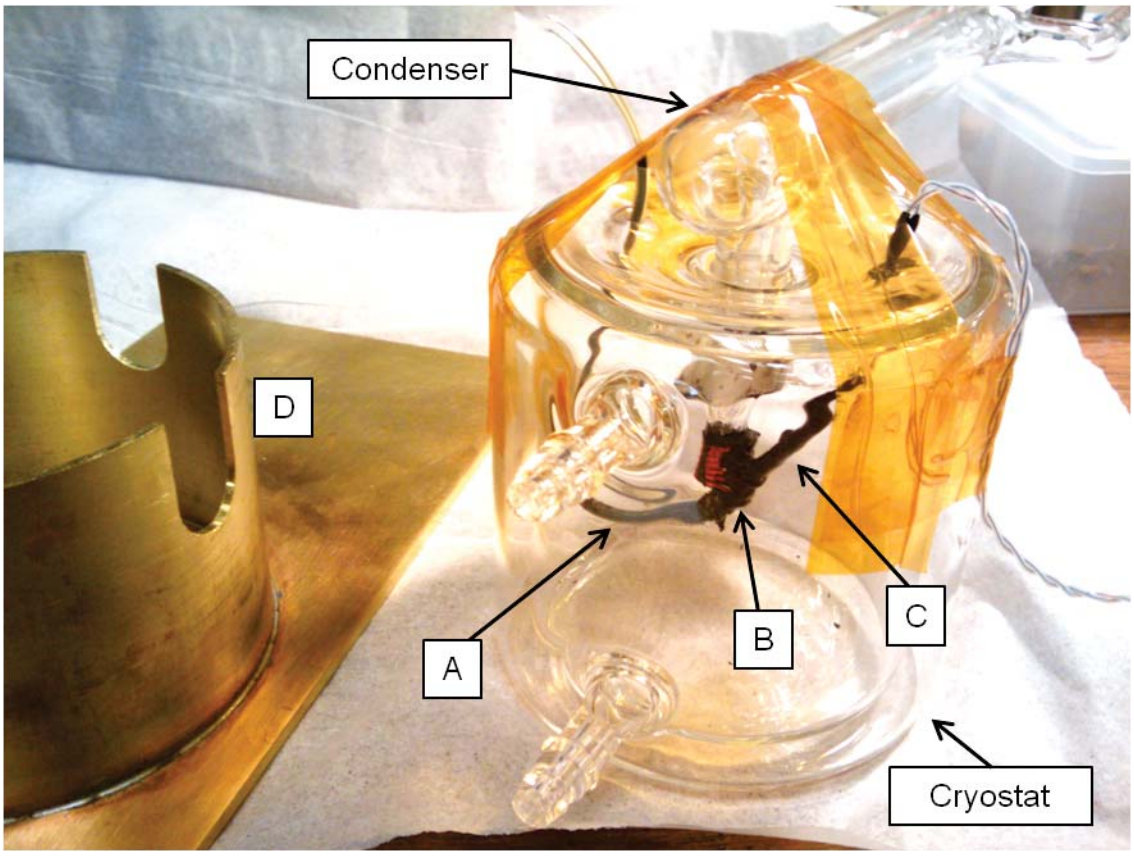

Figure 4.2. Photograph of the cryostat/condenser shown schematically in Figure 4.1. (A) and (C) are pointing to the wires leading to the NMR coil and RTD (Omega) respectively. (B) is the sample region where the NMR coil (red wires) is wrapped around the condenser tip and the RTD is fixed in place with cryogenic epoxy (black substance). (D) is the brass housing constructed to fix the cryostat in place inside the magnet and minimize motion from the numerous hoses that have to be attached to the condenser and cryostat.

getting too cold, extra precaution was taken by putting the LN_2 inlet and outlet on the opposite side of the cryostat relative to the capacitors, and room-temperature air was blown constantly into the aluminum box housing the capacitors.

The condenser and cryostat were designed in such a way as to allow the freezing of Xe out of a gas stream and then provide rapid (0.5-2 minutes) warming and cooling of a frozen Xe sample. The condenser and cryostat are separate pieces of equipment but were married in such a way that the outer walls of the tip of the condenser were in contact with the LN_2 held by the cryostat (Figure 4.1). The LN_2 in the cryostat was provided by continuous flow from a pressurized LN_2 dewar, and a second input into the cryostat could provide warm N_2 gas that was used to melt the Xe.

The gas stream containing hyperpolarzied ^{129}Xe was from the Utah flow-through polarizer and, in all results presented in this chapter, the pressure inside the condenser and polarizer was always ∼1 psi above atmospheric pressure with the relative gas concentrations of 66.2% fir He, 33.2% for N_2, and .007% for Xe (all of natural isotopic abundance).

The entire condenser/cryostat/brass holder was placed inside of a 2 Tesla horizontal bore superconducting magnet (same magnet as in Chapter 2) and the probe was connected to an Apollo (Tecmag) NMR console. Both a 50Ω resistive probe and a capacitively tuned probe (Figure 1.3) were used to monitor the ^{129}Xe magnetization. The tuned probe has a narrow frequency response when compared to the 50Ω probe, and consequently, only very small flip angles ($< 1°$) are necessary to observe signal decay over two orders of magnitude with a good signal-to-noise ratio. However, the capacitive coupling makes a tuned probe very susceptible to temperature fluctuations. A 50Ω probe is much less susceptible to temperature fluctuations as the frequency response width is very broad (∼3 MHz). However, the sensitivity is much lower, and larger flip angles (2°-8°) had to be used in order to produce large enough signal to observe a signal decay over two orders of magnitude. When using larger flip angles, measured T_1 times were corrected for RF loss after a flip angle calibration was done.

4.3 Method Used to Generate Xe Snow or Ice

The procedure used to freeze hyperpolarized ^{129}Xe into the condenser in order to manipulate the state (ice or snow) of the frozen Xe and measure the subsequent longitudinal relaxation time was as follows.

(1) Start the buffer gases flowing through the condenser from the polarizer (without Xe) at a pressure greater than atmosphere to minimize oxygen leakage into the sample. (2) Fill the cryostat with LN_2 and check the tuning of the probe if a tuned probe is being used. (3) Once the sample region is cold, start a pulse sequence with small flip angles to observe the accumulation of ^{129}Xe in the sample region, and then turn on the Xe flow. (4) Accumulate Xe until the precessing ^{129}Xe magnetization saturates the spectrometer's analog-to-digital converter (ADC), which typically took 10-15 minutes. In addition to saturating the ADC, a 15' minute accumulation is needed to collect enough Xe to ensure liquid formation. (5) Turn off the gas flow from the polarizer and seal the condenser with the Teflon valves located at the entrance to the magnet. (6) If the decay of Xe snow is begin measured, being the T_1 pulse sequence (low-angle flip and acquire every 10 minutes). (7) If the decay of Xe ice is

being measured, begin a pulse sequence with low-angle flips every 2 seconds, and introduce warm N_2 gas into the cryostat without turning off the LN_2 flow. (8) Continue flowing warm high-pressure N_2 gas into the cryostat and monitor the ^{129}Xe spectrum until all the ^{129}Xe is liquid. (9) Turn off the warm N_2 gas, and allow the LN_2 to refill the cryostat. See Figure 4.3 for ^{129}Xe spectra acquired during a snow to ice conversion and Figure 4.4 for representative FIDs. (10) Begin a T_1 sequence once the RTD reads 77 K for several minutes.

This procedure was perfected over the course of five months, and at least four different versions of cryostat/condenser/probe were constructed before the robust and reliable system described in Section 4.2 was designed and built.

4.4 Data

The two well-known methods to perform T_1 measurements using pulsed NMR are saturation and inversion recovery. Both of these methods use the recovery of the magnetization *up* to thermal equilibrium from either zero spin-polarization or from an inversion of the initial thermal polarization. Using either of these methods for frozen ^{129}Xe would require prohibitively long experimental times as the T_1 time for ^{129}Xe at 77 K is $\sim$2.5 hours. Instead, this experiment starts with a hyperpolarized sample and the T_1 time is measured by using RF pulses with small flip angles to monitor the ^{129}Xe magnetization decay down to thermal equilibrium. It is important to note that T_1 mechanisms are products of the spin dynamics in the sample and have no dependence on the initial polarization state.

^{129}Xe T_1 relaxations were measured by pulsing the ^{129}Xe every ten minutes with a small flip angle and then saving the FID. The signal height of the FID at 150 μs after the completion of the RF pulse was recorded for each acquired FID and plotted as a function of time (Figure 4.5). This method is identical to integrating the Fourier transform, since the ^{129}Xe T_2 in frozen Xe is $\sim$2 ms, and the initial height of the FID is proportional to the area under the Fourier spectrum.

After extensive work to remove any systematic effects, ^{129}Xe relaxation measurements that are analogous to those shown in Figure 4.5 were done six times on natural isotopic abundance snow, four times on natural isotopic abundance ice, once on isotopically enriched (85.6% ^{129}Xe, 1.8% ^{131}Xe, balance Xe with I=0) snow, and once on enriched ice. Only two enriched runs were done because of the prohibitive cost of flowing enriched Xe through the polarizer. Table 4.1 summarizes the results from the natural abundance measurements.

When using a 50Ω probe, a flip angle calibration had to be done to correct the T_1 decay

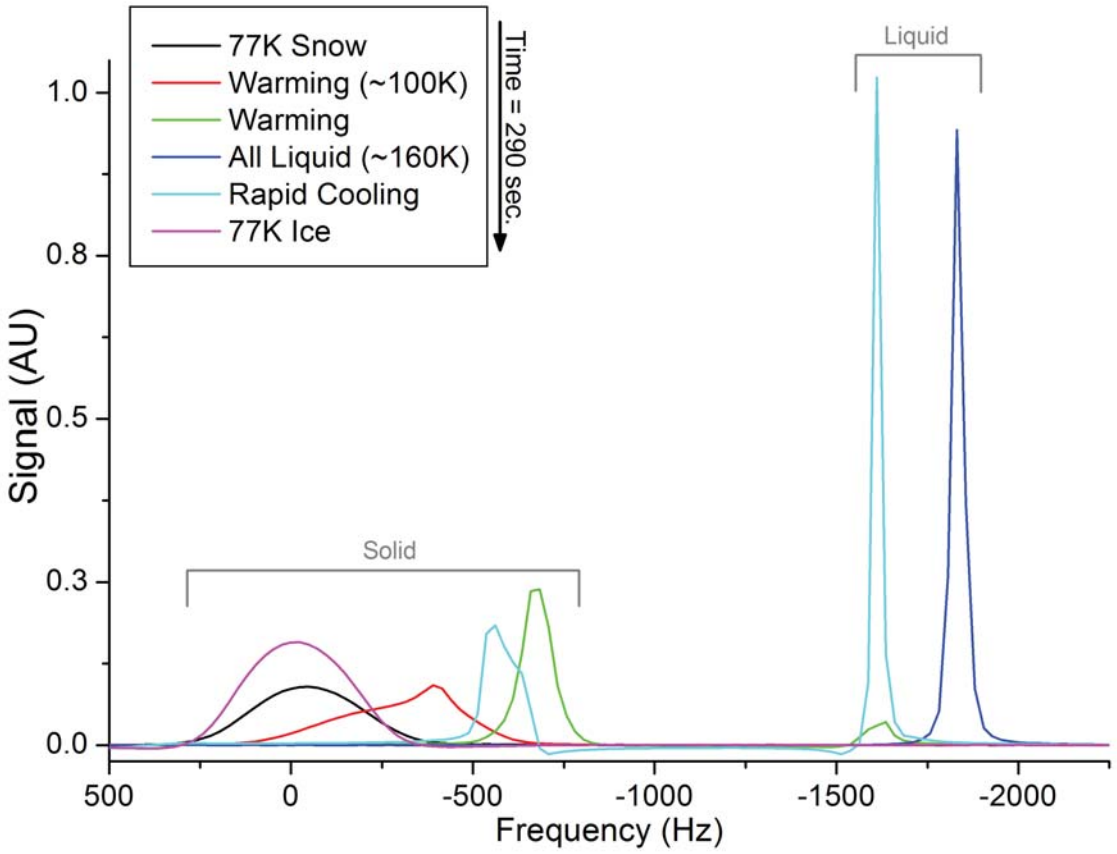

Figure 4.3. ^{129}Xe NMR spectra (0 Hz corresponds to 24.5 MHz RF frequency) acquired during the transition from accumulated snow, to liquid, and then to ice. The observation of the Xe state with ^{129}Xe NMR is the first of its kind and provides the necessary information to control what state the Xe is frozen in. To warm the sample, high-pressure room temperature N_2 gas is admitted into the cryostat. The temperature and ^{129}Xe NMR is monitored while blowing in the warm N_2 until the spectrum shows an all-liquid resonance. At this point, the warm N_2 is quickly cut off and the cryostat refills with LN_2 in less than a minute. Note that if the sample is warmed past the boiling point, a gas resonance appears at about -8000 Hz.

for magnetization loss caused by exciting the sample with each pulse (RF loss). Before the start of a T_1 measurement using a 50Ω probe, a series of 10-20 FIDs were acquired in rapid succession (∼10 ms apart). The FID height was plotted against the pulse number and a least squares fit to the function $f(n) = A(\cos\theta)^{n-1}$ was done. In the fitting function, θ is the flip angle, A is an amplitude, and n is the pulse number. The standard error from the fit was used as the error of the flip angle when correcting the T_1 measurements. Correction was done by dividing the T_1 signal by $(\cos\theta)^{n-1}$ where n is the pulse number of the T_1 measurement. The error on each point of the T_1 measurement must also be adjusted when correcting for RF loss, and this was done with standard error propagation using a Taylor

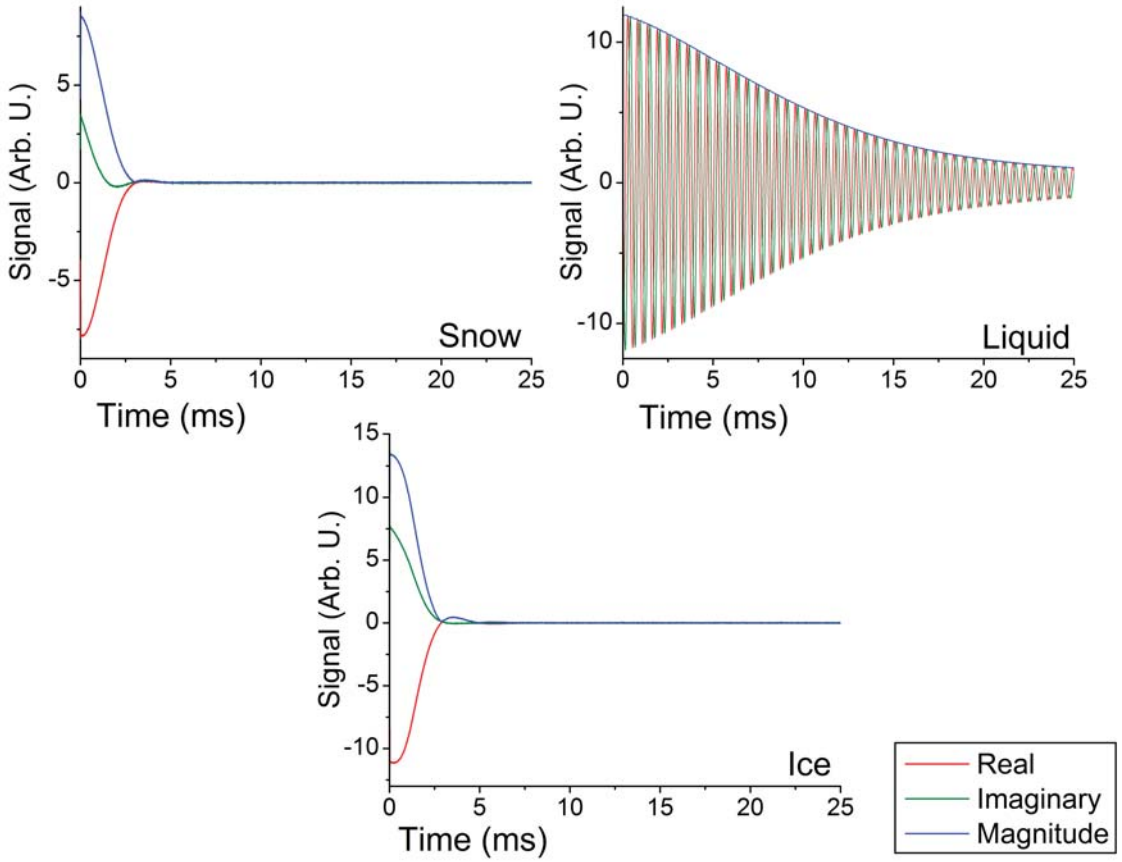

Figure 4.4. ^{129}Xe FIDs acquired during the transition from accumulated snow, to liquid, and then to ice. Note the substantial lengthening of the liquid T_2 due to motional narrowing. The increase in signal strength from snow to ice is from Xe melting and falling into the tip of the condenser where the NMR coil is. T_1 decay measurements were done by recording the value of the FID's magnitude signal at 100 μs every 10 minutes.

expansion. Experimental proof that the correction for RF loss was done correctly can be found in the T_1 results with the tuned probe ($< 1^\circ$ flip angle), which are within error of those acquired with a 50Ω probe.

4.5 Discussion

The Raman spin-phonon scattering process briefly described in Section 4.1 has been hypothesized to cause the relaxation of ^{129}Xe in Xe crystallites. Strong evidence that is in support of this theory correct was found when the ^{129}Xe relaxation times were measured as a function of temperature [42]. However, this theory alone cannot explain the difference between the snow and ice relaxation times.

Xe snow is white to the eye, and a simple order of magnitude argument (visible light is

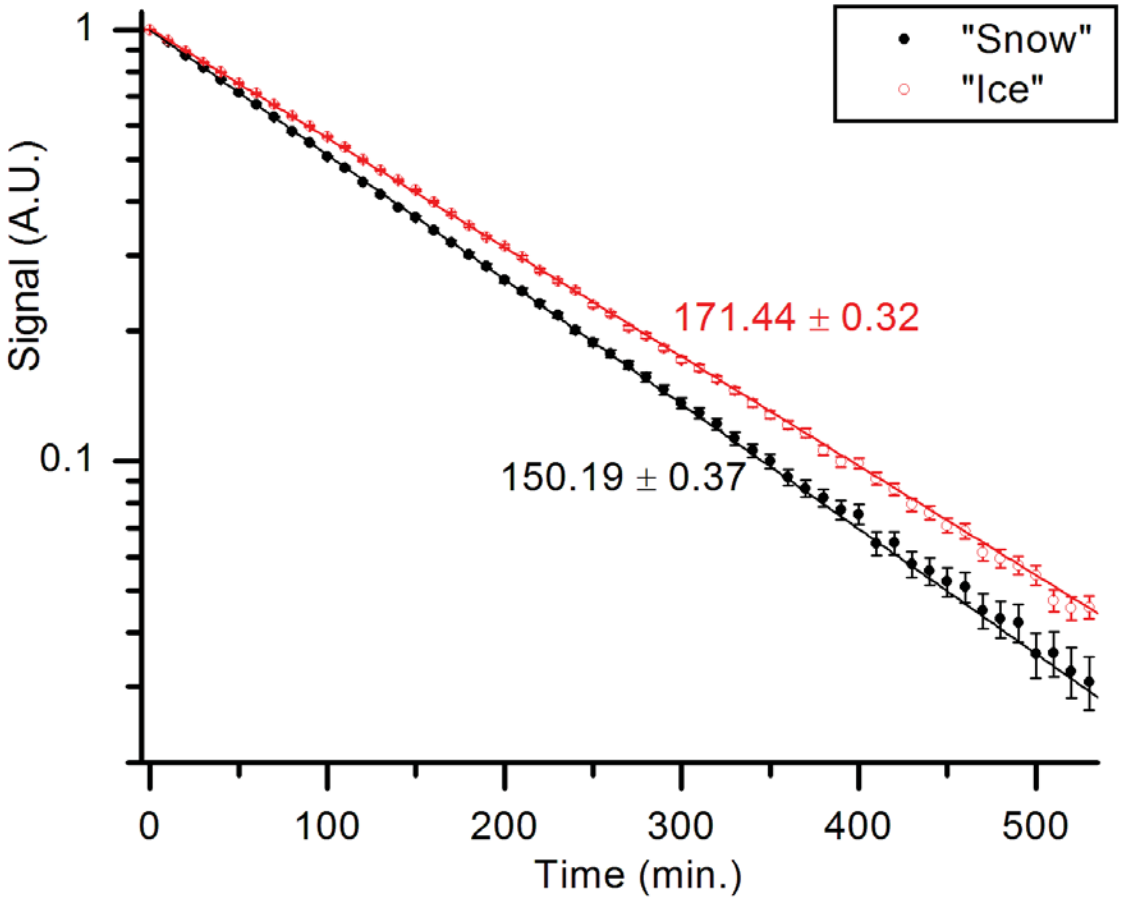

Figure 4.5. Example of two ^{129}Xe T_1 decay measurement which demonstrates the difference between Xe frozen as snow or ice. The y-axis represents the height of the FID decay envelope 150 μs after the completion of the RF pulse. The error bars are calculated from the RMS noise of the time domain signal and the uncertainty from a least squares fit when measuring the flip angle to account for RF losses. The signal decay is least squares fit to the function $f(t) = e^{-t/T_1}$ and the quoted error is the standard error from the fit. The method of producing snow and ice is explained in Section 4.3, and the reproducibility of the measured difference is demonstrated in Table 4.1.

about 400 nm) says that a single crystallite must be on order of 10 microns across to reflect white light [33]. Xe ice will most certainly have bigger crystallites unless the freezing method creates an amorphous Xe "glass" which is highly unlikely. The lattice constant of Xe has been measured to be 6.2023 Å at 75 K [62]. The four orders of magnitude difference between the crystallite size and lattice constant means for any given Xe atom in a *perfect* crystal, the lattice is essentially infinite and any phonon-driven process should be well described by bulk phonon modes. That is, even if the crystallite size in ice increases by an order of magnitude with respect to that of snow, the phonon spectrum should not change.

Table 4.1. T_1 results of ^{129}Xe in natural abundance Xe at 77 K. Each measurement is a completely new accumulation of frozen Xe from the polarizer. The stated errors are from least squares fits. The repeatability of these measurements is unprecedented, and the difference between ice and snow, while not understood at this point, is a possible explanation for variability in all previously published results.

Date	Probe Type	Flip Angle (deg.)	Xe State	T_1 time (min.)
5/19/2011	50Ω	6.91±0.14	snow	150.19±0.37
5/19/2011	50Ω	6.91±0.14	snow	149.80±0.40
5/19/2011	50Ω	6.27±0.07	snow	149.30±0.40
5/06/2011	50Ω	8.96±0.05	snow	148.61±0.42
4/27/2011	Tuned	NA	snow	148.47±0.08
5/02/2011	Tuned	NA	snow	150.79±0.43
5/23/2011	50Ω	2.67±0.19	ice	171.44±0.32
5/24/2011	50Ω	3.11±0.30	ice	172.02±0.31
4/28/2011	Tuned	NA	ice	169.93±0.25
5/09/2011	Tuned	NA	ice	168.16±0.16

Two enriched T_1 measurements were done with the goal of testing if the difference in relaxation rates could be caused by either the dipole-dipole effect between ^{129}Xe or cross-relaxation with ^{131}Xe rapidly relaxing at crystallite edges. The result was the enriched snow had bi-exponential behavior with one time constant at ∼100 minutes and the other ∼160 minutes. The bend in the relaxation curve is late in the data acquisition and the exact value of 160 minutes is not very precise. This result remains inconclusive as a small leak was later found to possibly be present in the condenser seals during the measurement. If any paramagnetic impurities (such as atmospheric O_2) are present in the Xe lattice, the relaxation rate should be approximately linear in ^{129}Xe concentration [16]. We indeed see a decrease of the snow relaxation time from ∼150 minutes in natural snow to ∼100 minutes in enriched snow. This is not linear in ^{129}Xe concentration. However, the O_2 would be able to interact only with the surface of the Xe crystallites and not appreciably affect the bulk relaxation.

A follow-up experiment that was conducted by Mark Limes purposely introduced air into a Xe snow sample during a T_1 measurement. The result was that the T_1 relaxation time dropped precipitously for about 30 minutes and then the relaxation time leveled off at 155 minutes and stayed constant until the end of the measurement. The same experiment was done on ice with no effect. This is strong evidence that O_2 can relax the surface of frozen Xe and cannot penetrate the bulk. The ice showed no effect because the interaction

region is only on top of the sample, whereas snow has a much greater surface area. Another conclusion that can be drawn from this experiment is that the snow T_1 results presented in this chapter are likely tainted by a very slow leak in the condenser. If a slow leak was present during the measurements, O_2 could leak in and slowly decrease the polarization of the ^{129}Xe at the surface of the crystallites. However, the difference between the surface and bulk relaxation rates might simply have been too small to observe any effect in an 8.3 hour experiment. The combination of the two very similar rates would result in a single slightly faster decay time (the difference between 150 and 155 minutes corresponds to a T_1 time of $\sim$3 days). However, the ice data presented would be unaffected by an O_2 leak, because the evidence indicates no diffusion of O_2 into the bulk crystalline Xe.

When considering explanations for the measured difference between snow and ice the following facts must be considered. O_2 in the sample region that affects the snow T_1 measurements has been experimentally ruled out. ^{129}Xe relaxation times due to dipole-dipole modulated by single phonons is predicted to be months; however, the results from the presented enriched data are inconclusive. Cross-relaxation with ^{131}Xe can be neglected above 500 G [28] and data in this chapter were acquired at 20,000 G.

A possible explanation for the T_1 difference is the existence of "mosaic spread" in the Xe crystal. Mosaic spread is a measure of the offset in position from unit-cell to unit-cell, but, the offset is not large enough to form a grain boundary. The mosaic spread of a crystal is known the be a function of the freezing rate [40, 68]. No literature was found on the mosaicity of noble gas van der Waals solids. However it is a reasonable expectation that upon freezing directly out of gas, the quality of crystal will be different from a rapidly frozen liquid, and as a consequence, the phonon spectrum could possibly change.

Another possible explanation could be the Debye temperature is different for ice and snow, which is also intricately tied to crystal formation.

4.6 Conclusions

The most reproducible and longest ^{129}Xe relaxation time at 77 K have been presented in this chapter as well as an unexplained difference in the ^{129}Xe relaxation rate when the Xe is frozen as "snow" or "ice". Future directions for this experiment should include measurements of ^{129}Xe T_1 in snow and ice as a function of temperature, neutron scattering to determine the actual crystal structure when frozen as snow or ice, and a method to reliably control the freezing rate.

CHAPTER 5

CHARACTERIZATION OF ENGINEERED CAVITIES IN PANCREATIC TRYPSIN INHIBITOR BY NMR-DETECTED XE BINDING

5.1 Introduction

The close packing of their interiors is one of the hallmarks of folded globular proteins. As first noted by Richards[53] and Finney[26], the density of atoms in folded proteins is close to that observed in crystals of small organic molecules, leading to a view of proteins as being solid-like. On the other hand, distinct cavities are not rare in folded proteins and can have significant energetic effects. Amino acid replacements that either increase or decrease the volumes of buried residues frequently destabilize protein native states, but in a few cases stability has been increased by filling interior voids.

One probe that has been used to identify and characterize protein cavities is xenon (Xe), which has been found to bind to specific sites in a variety of proteins. The noble gas is electrically neutral but highly polarizable, and has a size that is comparable to that of the smaller cavities typically found in proteins: The van der Waals radius of Xe is 2.2 Å, giving it a volume (45 $Å^3$) that is approximately equal to that of two methyl groups [53]. Xe binding to proteins as been detected by both solution NMR methods and X-ray crystallography, and the introduction of Xe into protein crystals has been used as an isomorphous replacement for crystallographic structure determination. However, only a few Xe-binding sites have been fully characterized thus far, and little is known about the factors that determine the relative affinities of Xe for different sites.

In the present study, NMR has been used to characterize the binding of Xe to cavities engineered in bovine pancreatic trypsin inhibitor (BPTI, Figure 5.1) by the replacement of tyrosine or phenylalanine with smaller residues. BPTI inhibits trypsin and other serine proteases and has been used as a model protein for biochemical and biophysical studies for

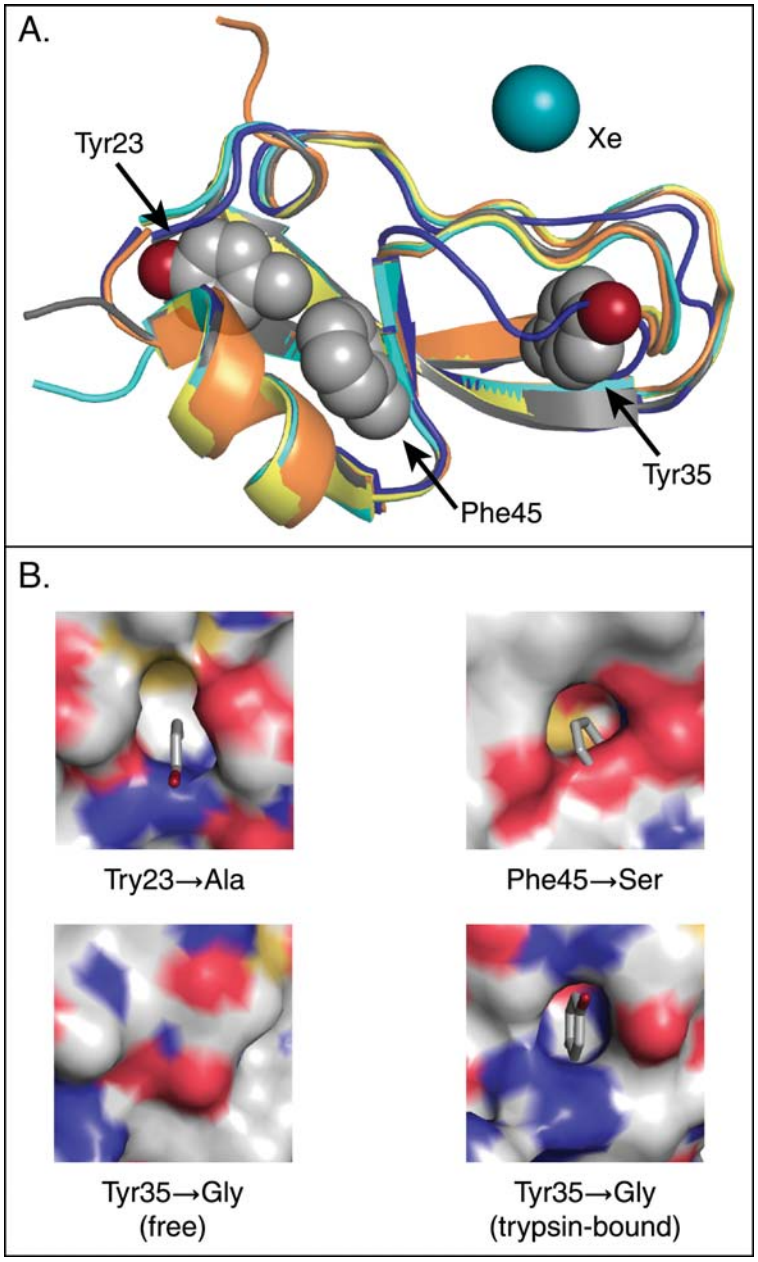

Figure 5.1. Structure of wild-type BPTI and three-cavity forming variants. (A) Ribbon diagrams of wild-type BPTI (Protein Data Bank entry 4PTI, gray ribbon with the side chains of Tyr23, Tyr35 and Phe45 shown as space-filling spheres), and the variants: Y23A (1BPT, yellow), F45A (1FAN, cyan) and Y35G. The free form of Y35G (8PTI) is colored blue and the trypsin bound form (2FTM) is orange. A sphere of radius 2.2 Å is shown on the same scale to represent the volume occupied by a Xe atom. (B) Surface representations of the replacement sites in the mutant proteins, with the wild-type side chains shown as sticks. The figure for the F45S variant is based on a model built from the F45A crystal structure.

more than four decades. The inhibitor binds tightly to the active sites of its target proteases with minimal structural change and is extremely resistant to hydrolysis. Due in part to the presence of three disulfide bonds, the native structure is unusually stable and tolerant of a variety of amino-acid replacements, making it particularly suitable for mutational studies.

The three sites examined here are all buried in the folded structure, as illustrated in Figure 5.1A, but previous crystallographic and NMR studies have shown that the protein responds quite differently to replacements at the different sites. In panel B of Figure 5.1, the local structures of the mutant proteins are illustrated with a surface representation to highlight the cavities, while the wild-type residues are shown as sticks. For two of the sites, Tyr23 and Phe45, replacement with Ala causes minimal perturbation of the structure and the formation of a water-filled cavity, as revealed by X-ray crystallography. (The structure shown in Figure 5.1B for the F45S variant used here is a model based on the crystal structure of the F45A protein.) In contrast, ^{15}N NMR relaxation measurements have shown that replacement of Tyr35 with smaller residues (Gly, Ala or Leu) leads to increased flexibility of the surrounding loop segments, which form the trypsin binding site (the right-hand end of the molecule as oriented in Figure 5.1A). An X-ray crystal structure of the Y35G variant displays remarkably large structural changes when compared with the wild-type structure, with some backbone atoms displaced by as much as 6 Å. These rearrangements allow the chain to fill the cavity that would otherwise be formed by the replacement. When Y35G BPTI binds to trypsin, however, the inhibitor takes on a conformation nearly identical to that of the wild-type protein, with a solvent-accessible cavity at the site of the replacement. It is not known to what extent the wild-type like structure, with its pronounced cavity, is populated when the Y35G protein is free in solution.

To probe the cavities described above, two types of NMR studies were carried out. In the first, binding was detected by changes in the chemical shift of ^{129}Xe, using hyperpolarized ^{129}Xe. These experiments were facilitated by a newly-developed apparatus for preparing hyperpolarized ^{129}Xe by spin-exchange optical pumping [61] and a special flow cell to equilibrate the protein solution with the gas. These studies demonstrated significant binding of Xe to the Y23A and F45A variants, but not to Y35G BPTI, indicating that the cavity observed when the Y35G protein is bound to trypsin is not present in a large fraction of molecules in the free state. In the second set of experiments, Y23A BPTI was uniformly labeled with ^{15}N, and heteronculear ^{15}N-^{1}H spectroscopy was used to identify and characterize the Xe-binding site. These studies indicate that the Y23A substitution generates a distinct

Xe-binding site. Comparison with published results for other proteins indicates that the Y23A site has a relatively low affinity for Xe, but that the ^{129}Xe chemical-shift change upon binding is among the largest observed to date.

5.2 Hyperpolarized ^{129}Xe NMR

5.2.1 Overview of Spin-Exchange Optical Pumping

The noble gas Xe has been found to bind to cavities in a variety of different proteins, typically with binding constants of 10 to 100 M^{-1}. Because Xe possesses a highly polarizable electron cloud, the chemical shift of ^{129}Xe is particularly sensitive to its surrounding environment, making NMR spectroscopy with this isotope an excellent probe of protein cavities. The sensitivity of ^{129}Xe NMR can be greatly enhanced by hyperpolarization through the process of of spin-exchange optical pumping (SEOP) [72]. The sensitivity of a given nucleus in magnetic resonance experiments is directly proportional to the polarization P, which, for the case of spin-1/2 nuclei such as ^{129}Xe, is given by

$$P = \frac{N_\uparrow - N_\downarrow}{N_\uparrow + N_\downarrow}, \tag{5.1}$$

where $N_{\uparrow/\downarrow}$ is the number of ^{129}Xe atoms having their nuclear spin in the "up/down" eigenstate with respect to the direction of the applied magnetic field denoted by $\mathbf{B}_0$. In thermal equilibrium at absolute temperature T, the polarization is given by $P = \mu B_0/k_B T$, where k_B is the Boltzmann constant and μ is the nuclear magnetic moment. Even in the largest laboratory magnetic fields, P is typically $\leq 10^{-4}$. Such low polarizations combined with low gas densities make conventional NMR with gases prohibitively insensitive. SEOP can enhance the polarization by five to six orders of magnitude, more than compensating for the low gas density and making NMR experiments with these gases feasible.

The SEOP process involves a two-step transfer of spin-angular momentum, first from circularly polarized resonant laser light to the electrons of Rb atoms, and then from the Rb electrons collisionally to the ^{129}Xe nuclei. The laser light is typically incident on a glass cell containing a macroscopic amount of Rb metal, Xe gas (^{129}Xe is 26% abundant in natural Xe), and other buffer gases that enhance the efficiency of SEOP. A small applied magnetic field (typically 30 G) provides a quantization axis for the spins. The relevant spin-transfer rates in the Rb-^{129}Xe system are such that polarized ^{129}Xe is most efficiently produced in a flow-through system, shown schematically in Figure 5.2a and fully described in reference [61]. A lean xenon gas mixture consisting mostly of nitrogen and helium flows

for 1-2 minutes through a long ($\approx$ 1 m) narrow glass cell and then flows out of the polarizer with $P_{\mathrm{Xe}} = 10 - 20\%$.

5.2.2 ^{129}Xe Delivery System

In the present studies, the gas mixture containing hyperpolarized ^{129}Xe was conducted through teflon tubing directly to the bore of the NMR magnet, where the tubing was connected to a hollow-fiber flow cell which (Figure 5.2b). The flow cell, similar to that described by Baumer *et al.* [9], delivered the gas through a bundle of microporous-membrane tubes immersed into the aqueous protein solution, without shaking or bubbling and resulting in a steady-state Xe concentration of $\approx$100 μM.

The hollow-fiber flow cell has two key features: The porous tubes are hydrophobic and the gas flowing through them can diffuse into the surrounding liquid without bubbling. The hydrophobicity prevents the protein solution from penetrating into the interior of the tubes and disrupting the gas flow. Inhibiting gas bubbling in the solution is essential for maintaining a narrow, dissolved ^{129}Xe resonance as the susceptibility difference between the liquid and gas bubble will upset the static magnetic field homogeneity and stability. Both 5 and 10 mm diameter versions of the modified NMR tube were constructed. The 5 mm tube enabled the use of higher protein concentrations and also resulted in narrower resonance peaks.

5.2.3 ^{129}Xe NMR Results

Using the apparatus described in Sections 5.2.1 and 5.2.2, ^{129}Xe NMR spectra were recorded for wild-type BPTI and the three single-replacement variants described in the Introduction and Figure 5.1. Spectra of solutions in solutions containing 0.14 to 6.3 mM wild-type BPTI are shown in Figure 5.3. Increasing protein concentrations resulted in down-field chemical-shift changes, indicating decreased shielding of the nucleus, but no change in peak shape or width. This pattern is consistent with fast exchange of the ^{129}Xe between different chemical environments, as has been observed in all previously-published studies of this type.

The measured chemical-shift changes for the BPTI variants are plotted as a function of protein concentration in Figure 5.4. Panel a of the figure represents measurements with all four proteins using the 10 mm diameter tube and protein concentrations up to 0.5 mM. Substantially larger chemical shifts were observed, at a given protein concentration, for the F45S and Y23A variants than for either the wild-type or Y35G proteins, suggesting

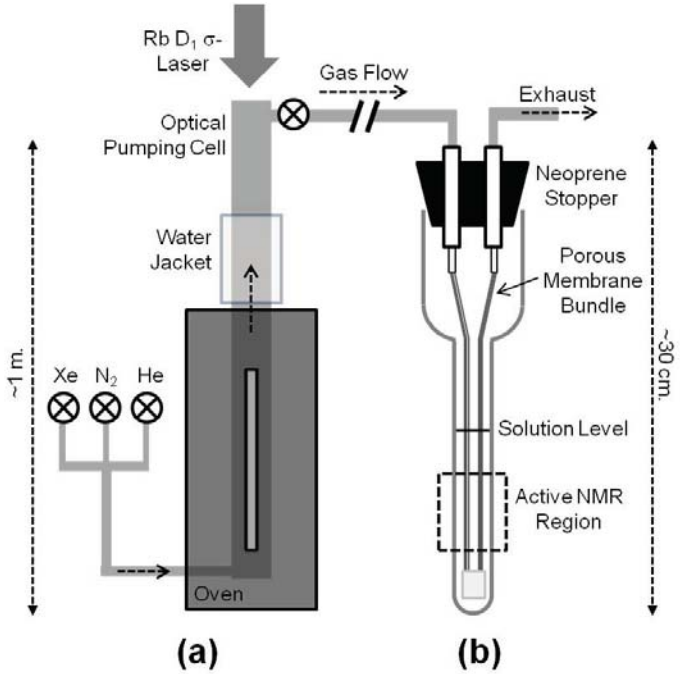

Figure 5.2. Schematic of complete system to deliver hyperpolarized ^{129}Xe to a protein solution. **(a)** ^{129}Xe flow-through polarizer. The adjustable gas mixture, lean in Xe, flows upward through the meter-long cell while the laser light propagates downward. The lower part of the cell is heated to create a sufficiently dense Rb vapor for optical pumping and spin exchange to occur. The water jacket helps to confine the Rb vapor to the lower half of the cell. The gas mixture, along with the now-hyperpolarized ^{129}Xe, exits out of the top of the pumping cell. **(b)** Hollow-fiber flow cell. The polarized Xe gas is carried in a teflon tube to the bore of the NMR magnet, where it flows throug a porous-membrane bundle contained in an NMR sample tube. Xe atoms diffuse through the micropores and into the aqueous solution, where their NMR frequency is chemically shifted by interactions with the dissolved protein.

that the F45S and Y23A proteins contained additional binding sites not present in the other two proteins. A second set of experiments were carried out using the 5 mm tube to measure chemical shift changes at higher concentrations of the wild-type and Y23A proteins (Figure 5.4b).

5.2.4 Interpreting the ^{129}Xe Chemical Shift as a Function of Protein Molarity

The chemical-shift changes were interpreted following the analysis of Rubin *et al.* [56], in which the observed resonance frequency is assumed to represent a population-weighted average of the shifts for ^{129}Xe in different chemical environments. The following theory will be explained in the context of the ^{129}Xe NMR frequency shift. However, the theory can

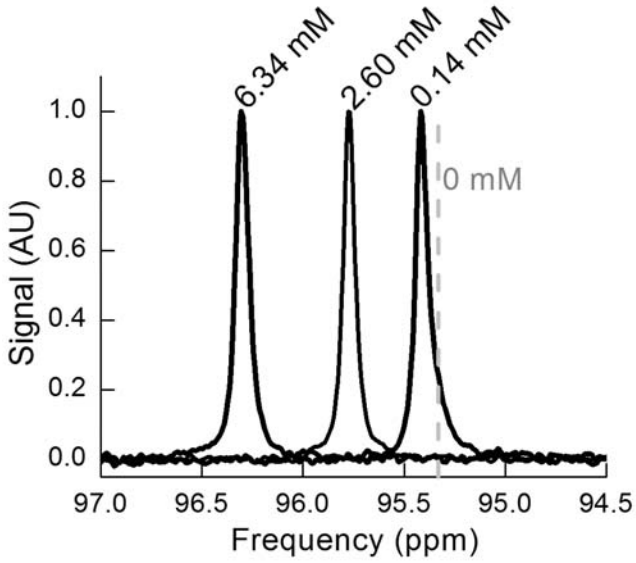

Figure 5.3. ^{129}Xe NMR spectra of hyperpolarized Xe in 25 mM phosphate buffer, pH 6.7, with the indicated concentrations of wild-type BPTI. The dashed line denotes the location of the ^{129}Xe resonance in buffer solution with no protein.

easily be reversed to explain the shift of the ^{1}H-^{15}N resonance frequency as a function of Xe concentration.

The observed ^{129}Xe chemical shift, δ_{obs} is given by:

$$\delta_{obs} = \delta_0 \frac{[\mathrm{Xe}_0]}{[\mathrm{Xe}_\mathrm{T}]} + \sum_i \delta_i \frac{[\mathrm{XeP}_i]}{[\mathrm{Xe}_\mathrm{T}]} \tag{5.2}$$

where Xe_0 is free Xe; $[\mathrm{Xe}]_\mathrm{T}$ is the total Xe concentration; XeP_i is Xe-protein complex i; δ_0 is the chemical shift of free Xe in buffer and δ_i is the chemical shift of Xe bound at site i. If the chemical shifts are expressed relative to that of free ^{129}Xe, this simplifies to:

$$\delta_{obs} = \sum_i \delta_i \frac{[\mathrm{XeP}_i]}{[\mathrm{Xe}_\mathrm{T}]} \tag{5.3}$$

For each binding site, the binding equilibrium expression is:

$$K_i = \frac{[\mathrm{XeP}_i]}{[\mathrm{Xe}_0][\mathrm{P}_i]} \tag{5.4}$$

where K_i is the binding constant and $[\mathrm{P}_i]$ is the concentration of protein molecules in which binding site i is unoccupied. The expression for δ_{obs} can then be written as:

$$\begin{aligned} \delta_{obs} &= \sum_i \delta_i \frac{K_i[\mathrm{Xe}_0][\mathrm{P}_i]}{[\mathrm{Xe}_\mathrm{T}]} \\ &= \frac{[\mathrm{Xe}_0]}{[\mathrm{Xe}]_T} \sum_i \delta_i K_i [\mathrm{P}_i] \end{aligned} \tag{5.5}$$

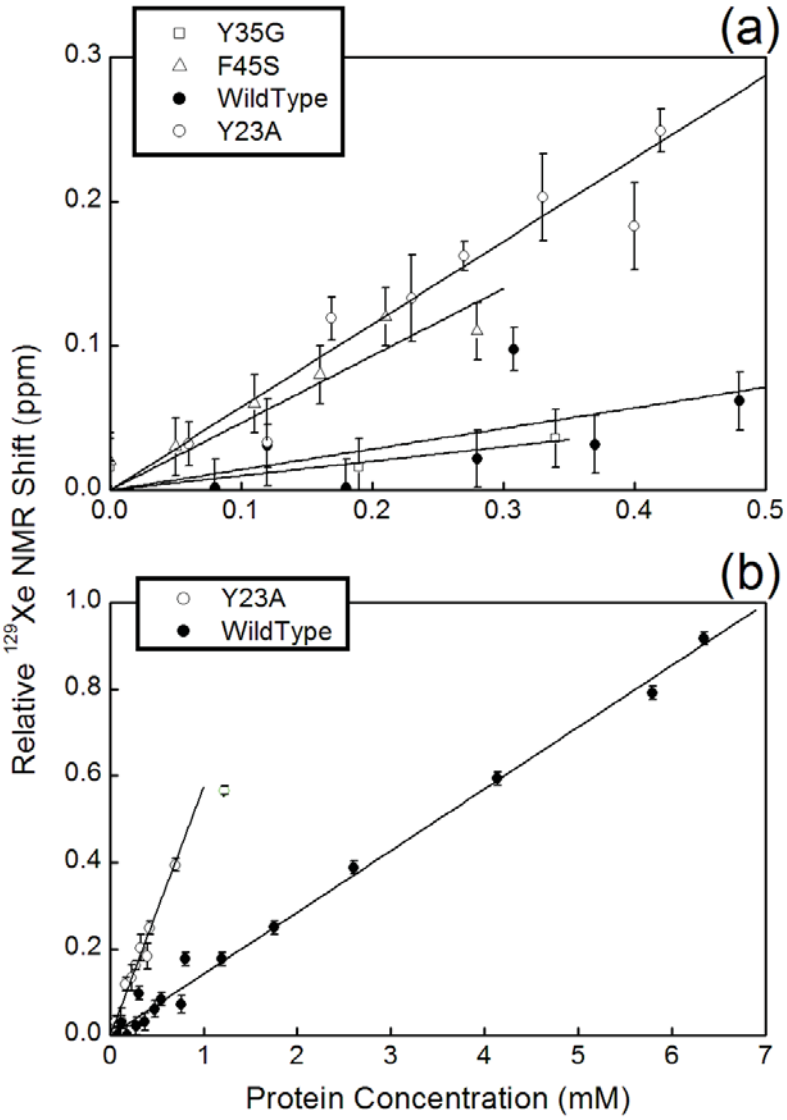

Figure 5.4. ^{129}Xe chemical shift vs protein concentration. (a) Chemical shifts at low concentrations of wild-type, Y23A, Y35G and F45S BPTI, using the 10 mm sample tube. (b) Chemical shifts in the presence of higher concentrations of Y23A and wild-type BPTI, measured using the 5 mm sample tube. Chemical shift changes are expressed relative to the ^{129}Xe resonance in buffer solution with no protein.

The total ^{129}Xe concentration is given by:

$$\begin{aligned}[\mathrm{Xe}]_T &= [\mathrm{Xe_0}] + \sum_i [\mathrm{XeP}_i] \\ &= [\mathrm{Xe_0}] + \sum_i K_i[\mathrm{Xe_0}][\mathrm{P}_i] \\ &= [\mathrm{Xe_0}]\left(1 + \sum_i K_i[\mathrm{P}_i]\right) \end{aligned} \tag{5.6}$$

Provided that the binding constants and protein concentration are sufficiently low that the sum $\sum_i K_i[\mathrm{P}_i]$ is much less than 1, then $[\mathrm{X_T}] \approx [\mathrm{Xe_0}]$. The total concentration of protein moleculecules, [P], can be expressed in terms of the concentrations of the open and filled forms of each of the binding sites (assuming nonoverlapping sites):

$$\begin{aligned}[\mathrm{P}] &= [\mathrm{P_i}] + [\mathrm{XeP_i}] \\ &= [\mathrm{P_i}](1 + K_i[\mathrm{Xe_0}]) \end{aligned} \tag{5.7}$$

If the product $K_i[\mathrm{Xe_0}]$ is much less than one for each binding site, then $[\mathrm{P}_i] \approx [\mathrm{P}]$. When both conditions are satisfied, the expression for δ_{obs} simplifies to:

$$\delta_{obs} = [\mathrm{P}] \sum_i \delta_i K_i \tag{5.8}$$

The slope of the linear plots of δ_{obs} versus [P], as in Figure 5.4, then represent the sum of the products $\delta_i K_i$ for all of the binding sites. The total slope is defined as α_T:

$$\alpha_T = \sum_i \delta_i K_i = \sum_i \alpha_i \tag{5.9}$$

where $\alpha_i = \delta_i K_i$.

For the mutant proteins, we assume that there is one additional specific site not present in the wild-type protein, for which $\alpha_s = \delta_s K_s$, and the total contribution from the sites also present in the wild-type protein can be written as α_{ns}. The value of α_s can then be calculated as the difference between α_T for the mutant and wild-type proteins:

$$\alpha_s = \alpha_{T,mut} - \alpha_{ns} \tag{5.10}$$

$$= \alpha_{T,mut} - \alpha_{T,wt} \tag{5.11}$$

5.2.5 Analysis of ^{129}Xe NMR Data

As shown in Figure 5.4, the observed chemical shifts displayed a linear relationship with protein concentration, consistent with the assumptions of the theory in Section 5.2.4. The observed slopes, α_T for the wild-type and mutant proteins are listed in Table 5.1, along with the calculated values of α_s for the mutants. For the wild-type protein, α_T was 0.15 ppm/mM. For the Y23A and F45S variants were significantly higher, leading to estimates of α_s of 0.56 and 0.47 ppm/mM, respectively, indicating the presence of additional binding sites not present in the wild-type protein. These values lie with in the range of those measured for several other protein cavities (0.2 to 1.5 ppm/mM), as listed in Table 5.2. On the other hand, there was no significant difference between α_T for the Y35G variant and that of the wild-type protein, suggesting that the cavity observed in the structure of this protein when bound to trypsin is not present in a majority of the free molecules.

In order to separate K_s and δ_s accurately, an estimate for K_s is needed that includes data from the saturation regime. In short, one species must be in concentrations excess of the K_d (roughly 100 M^{-1} for Xe-protein binding systems), which requires one species to exceed 10 mM. For protein solutions this is prohibitive, owing to the limits of solubility and bacterial expression. However, Xe has favorable solubility (4.3 mM/atm at 25 °C [49]), allowing us to reach Xe concentrations greater than 60 mM with relative ease within our technical limits. Consequently, we conducted experiments with protein as the observed species, allowing us to characterize saturation of binding, as well as the location of Xe binding sites through the use of heteronuclear experiments.

5.3 ^{1}H-^{15}N HSQC Under Varying Molarity of Dissolved Xe

^{1}H-^{15}N heteronuclear single quantum coherence (HSQC) was performed on uniformly labeled wild-type and Y23A BPTI different concentrations of Xe dissolved in the protein solution. The labeled protein was expressed by mutated *E. coli*. To achieve a molarity of Xe in solution that would appreciably effect the ^{1}H or ^{15}N resonance a high pressure NMR tube (Wilmad 513-7PVH-7) containing the protein sample was filled with a precise ($\pm$0.01 psi) pressure of naturally abundant Xe and allowed to sit for over 12 hours at room temperature before starting the HSQC.

Chemical shifts for Y23A backbone amides were established using typical sequential assignment methods. The combined chemical shift differences between wild-type and Y23A

Table 5.1. Table of ^{129}Xe NMR chemical shift results from data shown in Figure 5.4

Protein Variant	Max. Protein Conc. (mM)	α_T (ppm/mM)[c]	α_s (ppm/mM)[d]
Wild type[a]	0.8	0.15±0.02	NA
Wild type[b]	6.3	0.14±0.002	NA
Y23A[a]	0.4	0.56±0.05	0.41±0.07
Y23A[b]	0.7	0.58±0.02	0.44±0.02
Y35G[a]	0.34	0.10±0.07	-0.05±0.1
F45S[a]	0.28	0.47±.07	0.32±0.1

[a] Measurements made using the 10 mm diameter cell.
[b] Measurements made using the 5 mm diameter cell.
[c] Slope of ^{129}Xe chemical shift versus protein concentration.
[d] $\alpha_s = \alpha_{T,mut} - \alpha_{T,wt}$

are shown in Figure 5.5A, and were calculated as

$$\Delta\delta = \left[\Delta\delta_H^2 + \omega^2\Delta\delta_N^2\right]^{\frac{1}{2}} \tag{5.12}$$

where δ_H^2 and δ_N^2 are the ^{1}H and ^{15}N chemical shift differences, respectively, and $\omega = 0.101$ is the ratio of the ^{15}N to ^{1}H gyromagnetic ratio. Notably, four segments of the polypeptide proximal to the site of alteration show the most significant changes, whereas distal regions show little change. This is consistent with the crystal structure for Y23A, which shows little structural change relative to wild-type BPTI.

Xe binding experiments were performed on wild-type BPTI. As expected, Xe provokes minimal changes in wild-type BPTI chemical shifts with increasing concentration. At Xe concentrations of 68 mM, combined chemical shifts were no greater than 0.006 ppm for any given residue. The absence of a significant hydrophobic binding site reduces Xe interactions to nonspecific contact with the protein surface, consequently providing only transient changes to the chemical shifts lost to ensemble averaging. Based on the estimates for the binding constant in the ^{129}Xe experiments, we can conclude that wild-type BPTI contains no Xe binding sites of consequence.

For Y23A, substantial changes in the chemical shifts were observed with increasing Xenon pressure. Figure 5.5B shows the combined chemical shift differences for Y23A between 0 and 68 mM Xe. Four segments show significant changes, which map consistently to the same segments where changes were observed between wild-type and Y23A. Furthermore, mapping these changes to the crystal structure on a per residue basis (Figure 5.6) indicates

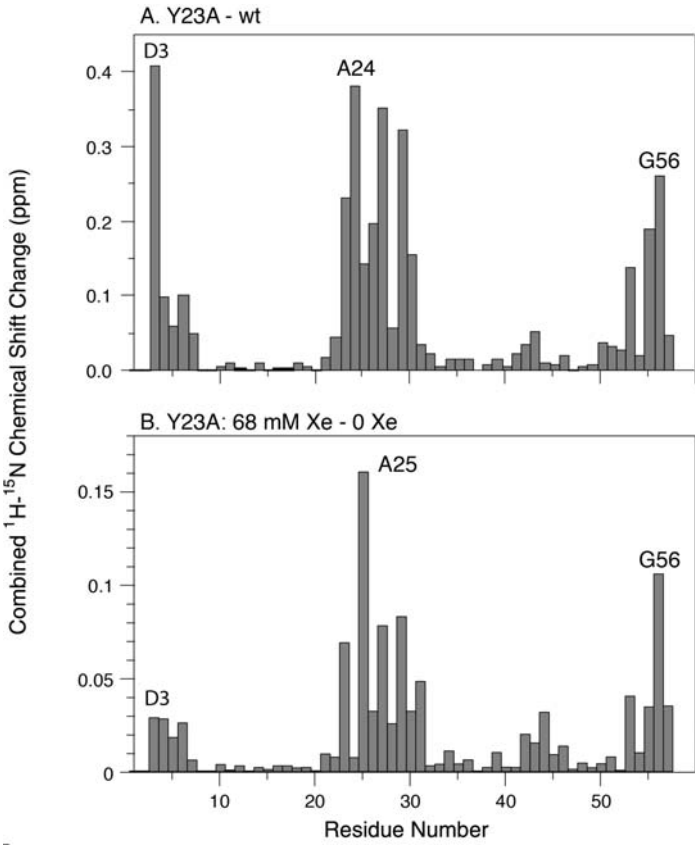

Figure 5.5. ^{1}H and ^{15}N amide chemical shift changes due to the Y23A substitution (A) and binding of Xe to Y23A BPTI (B). Chemical shifts were measured from ^{1}H-^{15}N HSQC spectra of wild-type BPTI and Y23A BPTI in the presence of 0 and 68 mM Xe. The combined ^{1}H-^{15}N chemical shift change was calculated from Eqn. 5.12.

that these segments surround the cavity created by the loss of the aromatic ring from tyrosine. Consequently, we can infer that specific binding of Xe occurs in the cavity created by the Y23A substitution.

To estimate the value of K_s, residues with a maximum chemical shift $\geq$0.03 ppm at 68 mM were fit to

$$\Delta\delta_{max} = \Delta\delta_{max} K_s \frac{[\mathrm{Xe_T}]}{1 + K_s[\mathrm{Xe_T}]} \tag{5.13}$$

where $\Delta\delta_{max}$ is the maximum chemical shift change when the binding site is fully occupied and the free Xe concentration is assumed to be equal to the total concentration. Sample fits are shown in Figure 5.7 for Phe4 (A) and Ala25 (B), with the fit values for K_s are shown in (C) for the respective ^{1}H and ^{15}N fits. The average value for K_s was calculated as 12$\pm$0.3 M^{-1}, weighting each term by the inverse of he squared standard errors, and

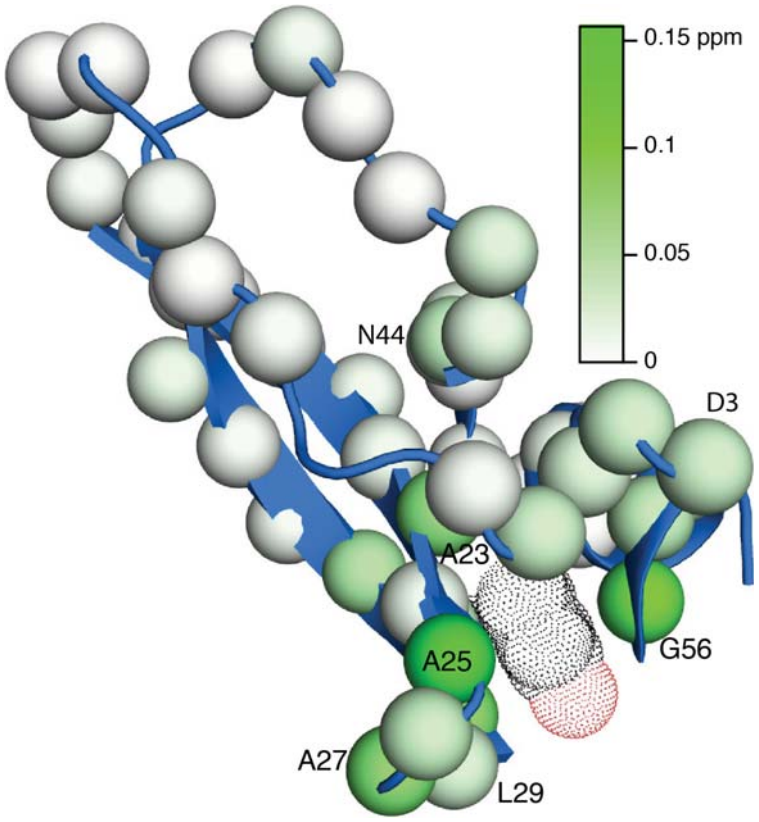

Figure 5.6. ^{1}H-^{15}N chemical shift changes due to Xe binding to Y23A BPTI mapped onto the protein crystal structure (1BPT). The backbone amide N atoms for which chemical shift data were obtained are shown as spheres with colors representing the combined chemical shifts, as indicated by the color scale. The dot surface represents the atoms of wild-type BPTI that are deleted in the Y25A mutant and were drawn from the coordinates of the wild-type structure (4PTI) after alignment with the Y23A structure.

excluding the ^{1}H derived K_s values for Asp3 and Gn31. Without weighting the average for K_s is $18\pm0.3\,\mathrm{M}^{-1}$. From the weighted average of K_s we can derive δ_s using the value of α_s derived from the ^{129}Xe NMR experiments to estimate the ^{129}Xe chemical shift change: $\delta_s = \alpha_s/K_s = 37 \pm 2\,\mathrm{ppm}$.

5.4 Discussion of Results

The results from combining the hyperpolarized ^{129}Xe NMR and ^{1}H-^{15}N HSQC results to yield the binding affinity K_s and ^{129}Xe chemical shift $\Delta\delta_{\mathrm{Xe}}$ are shown in Table 5.2 along with several other prior results for other proteins from the literature.

When compared on a per-site basis, the range of values for the binding constants and the maximum ^{129}Xe chemical shift change is relatively limited, about one order of magnitude

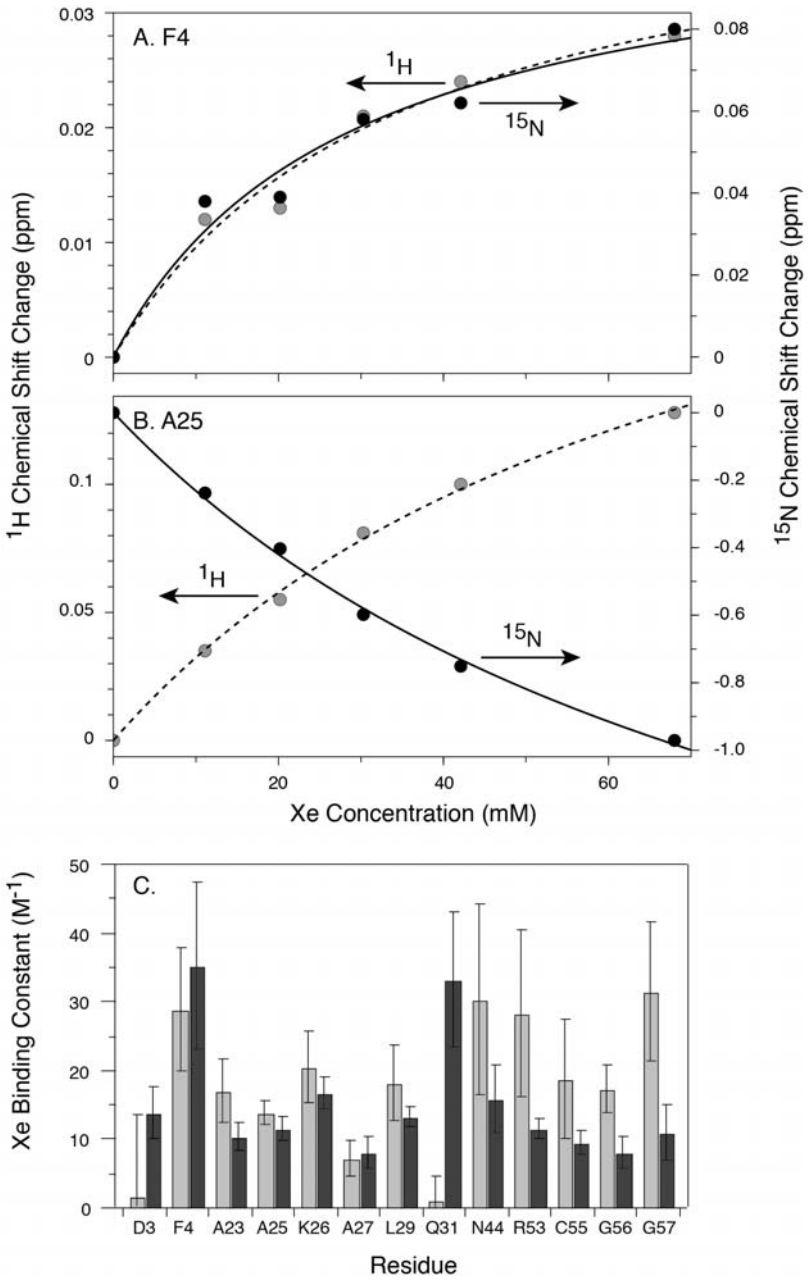

Figure 5.7. Binding isotherms for Xe binding to Y23A BPTI. In A and B, ^{1}H (light shaded symbols) and ^{15}N (dark shaded symbols) chemical shift differences for the backbone amide groups of Phe4 and Al25 are plotted as a function of total Xe concentration. The curves represent fits of the experimental data to Eqn. 5.13. (C) Estimated binding constants derived from ^{1}H (light shading) and ^{15}N (dark shading) chemical shift changes for the 13 backbone amide groups for which the combined chemical shift change was greater than 0.03 ppm. The error bars represent the standard errors derived from least-squares fitting.

Table 5.2. Table comparing ^{129}Xe binding sites in this work to prior publications

Protein	α_s (ppm/mM)	K_s (M^{-1})	$\Delta\delta_{Xe}$ (ppm)	Volume (Å^3)[a] 1.4 Å	2 Å	Ref
BPTI, Y23A	0.44±0.02	12.0 ± 0.3	37±2	85	46	
BPTI, F45S	0.3±0.1			75		
T4 lysozyme	2.0±0.1	60.0±0.2	32±2	51		[22]
T4 lysozyme, L99A[b]	0.3±0.2	90±40	3±4	146	49	[56]
T4 lysozyme, L99A[c]	1.5±0.2	50±10	30±10	45		[56]
RBP[d], L19A, open	0.5±0.3	70±30	7±3	113		[45]
RBP, L19A, closed	0.2±0.2	40±20	5±3	160		[45]
myoglobin, horse[e]	-1.2±0.1	125±9	-10±0.5	54		[44]
myoglobin, pig[e]	-0.6±0.2	75±20	-8±1	45		[20]

[a] Cavity volumes were calculated using the CAST algorithm[43, 25], with probe radii of 1.4 or 2 Å, as indicated. The absence of a volume for the 2 Å probe radius indicates that the cavity was not detected. The atomic coordinate files used are listed in Appendix F.
[b] (Site 1) L99A/L99A+benzene
[c] (Site 2) L99A+benzene/L99A+*n*-butylbenzene
[d] Ribose binding protein from *E. coli*
[e] Studies of horse and pig myoglobin used the met (Fe^{3+}) forms of the protein. In each study, overall values for K_s and $\Delta\delta_{Xe}$ were determined by fitting data for three experiments at different ^{129}Xe concentrations, and the values tabulated here are are error-weighted averages of the estimates from the three experiments. The values for $\Delta\delta_{Xe}$ have been divided by four to account for the four Xe-binding sites in myoglobin. The derived estimates of α_s also represent an average for the individual sites.

for each. The range of values for $\alpha_s = K_s\Delta\delta_s$ is even more limited, reflecting a tendency for large binding constants to be associated with smaller chemical shift changes.

When considering the results presented in this work compared to previously published work, it is important to consider the rigidity of the protein and the cavity size. To be self-consistent and provided a systematic comparison, we have calculated all of the cavity volumes presented in Table 5.2 with the Computed Atlas of Surface Topography of proteins (CAST) [25] algorithm.

The CAST algorithm use a "probe" atom with a given vdW radius. For almost all previously studied sites, cavities are typically not numerically-detectable unless a probe is used with a radius that is significantly smaller than the Xe vdW radius (2.2 Å); Typically, 1.4 Å is used in the computations. This does not coincide well with experimentally verified Xe binding and the discrepancy is generally explained by invoking flexibility of the protein

while in solution. The cavity in Y23A BPTI is one of the few sites that was able to accommodates a probe with a radius as large as 2.0 Å. This could indicate the Y23A site is quite rigid and just able to fit the Xe.

A rigid cavity with an opening that barely fits the Xe could also explain the low K_s and high $\Delta\delta_{\mathrm{Xe}}$ values for Y23A. An opening that barely admits a Xe atom will make it much harder for a Xe to bind, hence the low K_s. However, once the Xe atom is inside cavity the size and rigidity could potentially impose much more electron cloud deformation than a larger or less rigid cavity, hence the high $\Delta\delta_{\mathrm{Xe}}$. Previous studies have suggested an inverse correlation between cavity size and chemical shift change and the results from our CAST calculation seem consistent with that pattern.

5.5 Acknowledgements

This chapter is a draft of a paper to be submitted to Protein Science. The work contained within is not all my own and would not have been possible without the other authors. Geoff Schrank built the flow-through polarizer and worked with me on the initial hyperpolarized ^{129}Xe measurements. Albert Lund played a major role in synthesizing the proteins both for hyperpolarized ^{129}Xe NMR and ^{1}H-^{15}N HSQC measurements. He also identified the residues on the HSQC spectrum with additional 2D relaxation measurements. Brian Saam provided NMR and SEOP knowledge throughout. David Goldenberg provided biological insight and the equipment necessary to produce the proteins. He also is soley responsible for the CAST calculations and production of all the biological figures in this chapter.

APPENDIX A

CONSERVATION OF THE SPECTRAL CENTER OF MASS

This appendix is the proof that the spectral center of mass (COM) of a Fourier transformed FID is preserved after a time domain multiplication of an exponential

The definition of a convolution is

$$f(t) \otimes g(t) = \int_{-\infty}^{\infty} f(t-\alpha) \cdot g(\alpha)\, \mathrm{d}\alpha, \tag{A.1}$$

where $\otimes$ denotes a convolution.

Define the Fourier transform of functions f and g as $\mathcal{F}\{f\} = \mathrm{F}(\omega)$ and $\mathcal{F}\{g\} = \mathrm{G}(\omega)$, respectively. The convolution theorem says

$$\mathcal{F}\{f \cdot g\} = \mathrm{F}(\omega) \otimes \mathrm{G}(\omega). \tag{A.2}$$

Let f be the unprocessed FID and g be the exponential multiplication. The spectral center of mass is equal to

$$\mathrm{COM} = \frac{\int \omega \left(\mathrm{F}(\omega) \otimes \mathrm{G}(\omega)\right)\, d\omega}{\int \left(\mathrm{F}(\omega) \otimes \mathrm{G}(\omega)\right)\, d\omega}. \tag{A.3}$$

Substituting Equation A.1 into Equation A.3 yields

$$\mathrm{COM} = \frac{\int_{-\infty}^{\infty} \omega \left(\int_{-\infty}^{\infty} \mathrm{F}(\omega-\alpha) \cdot \mathrm{G}(\alpha)\, \mathrm{d}\alpha\right)\, \mathrm{d}\omega}{\int_{-\infty}^{\infty} \left(\int_{-\infty}^{\infty} \mathrm{F}(\omega-\alpha) \cdot \mathrm{G}(\alpha)\, \mathrm{d}\alpha\right)\, \mathrm{d}\omega}. \tag{A.4}$$

Reversing the order of integration of the numerator and substituting $\beta = \omega - \alpha$ throughout gives

$$\mathrm{COM} = \frac{\int_{-\infty}^{\infty} \mathrm{G}(\alpha) \left(\int_{-\infty}^{\infty} (\beta+\alpha)\mathrm{F}(\beta)\, \mathrm{d}\beta\right)\, \mathrm{d}\alpha}{\left(\int_{-\infty}^{\infty} \mathrm{G}(\alpha)\, \mathrm{d}\alpha\right)\left(\int_{-\infty}^{\infty} \mathrm{F}(\beta)\, \mathrm{d}\beta\right)} \tag{A.5}$$

$$= \frac{\left(\int_{-\infty}^{\infty} \mathrm{G}(\alpha)\, \mathrm{d}\alpha\right)\left(\int_{-\infty}^{\infty} \beta\mathrm{F}(\beta)\, \mathrm{d}\beta\right) + \left(\int_{-\infty}^{\infty} \alpha\mathrm{G}(\alpha)\, \mathrm{d}\alpha\right)\left(\int_{-\infty}^{\infty} \mathrm{F}(\beta)\, \mathrm{d}\beta\right)}{\left(\int_{-\infty}^{\infty} \mathrm{G}(\alpha)\, \mathrm{d}\alpha\right)\left(\int_{-\infty}^{\infty} \mathrm{F}(\beta)\, \mathrm{d}\beta\right)} \tag{A.6}$$

The function g multiplying the FID in the time domain is an exponential and the Fourier transform of an exponential is a Lorentzian. A Lorentzian is a symmetric function, and therefore $\left(\int_{-\infty}^{\infty} \alpha \mathrm{G}(\alpha)\,\mathrm{d}\alpha\right) = 0$. The spectral center of mass becomes

$$\mathrm{COM} = \frac{\int_{-\infty}^{\infty} \beta \mathrm{F}(\beta)\,\mathrm{d}\beta}{\int_{-\infty}^{\infty} \mathrm{F}(\beta)\,\mathrm{d}\beta}, \tag{A.7}$$

which is identical to the spectral center of mass before multiplying the FID by an exponential.

Given a function g that has a symmetric Fourier transform, the above argument is a proof that an FID can be multiplied by g and the spectral center of mass will be preserved.

APPENDIX B

NUMERIC INTEGRATION OF A SPHERICAL DISTRIBUTION OF DIPOLES

```
#include <string>
#include <iostream>
#include <fstream>
#include <math.h>
#include <time.h>

using namespace std;

//number of divisions in one dimension (choose odd to make the integration
    space symmetric around zero)
#define N 43

int main ()
{
  time_t  start, finish;
  double elapsed_time;

//File to output Magnetic field
  ofstream myfile;
  myfile.open("43pt_complete_33.txt");

// cylinder with uniform constant magnetization in z direction
  float M;

// Dimensions in cm (D is diameter and is equal to the length)
  float D=1; float R;
  R=D/2;

// Volume element and step size
  float step; float vol;
  step=D/(N-1);
  vol=step*step*step;

// Temporary Summation Variables for the integral
  float SumX; float SumY; float SumZ;

// Field (capitol) and source (lower) points
  float X; float Y; float Z;
  float x; float y; float z;
```

```
/* Variable to control the depth of magnetization;
must be inside array dimensions N;
The light approaches from higher numbers, i.e. a limit value of 5 means the
    back 5 slices of the sphere have a magnetic moment of zero;
*/
  float limit;
  limit=33;

// Array for Magnetic Field
  float BX[N][N][N]; float BY[N][N][N]; float BZ[N][N][N];

//Magnitude Variable
  float Mag;

  time( &start );
// Dipole Integration Loop
  cout << "Dipole Field Calculation" << endl;

  for (int i=0; i<N; i++){
    cout << i << " ";
   for (int j=0; j<N; j++){
     for (int k=0; k<N; k++){
      X=(i-(N-1)/2)*step;  // The (N-1)/2 is to place the origin at the center
           of the object
      Y=(j-(N-1)/2)*step;
      Z=(k-(N-1)/2)*step;
      SumX=0;
      SumY=0;
      SumZ=0;

      for(int l=0; l<N; l++){
        for (int m=0; m<N; m++){
         for (int n=0; n<N; n++){
         x=(l-(N-1)/2)*step;
         y=(m-(N-1)/2)*step;
         z=(n-(N-1)/2)*step;
         Mag=pow((float)(X-x)*(X-x)+(Y-y)*(Y-y)+(Z-z)*(Z-z),(float).5);
         if (R<(pow((float)x*x+y*y+z*z,(float).5))) M=0;
         else{
             if (n<limit) M=0; else M=1;
              }
         if (X==x && Y==y && Z==z) continue;
         else{
             SumX+=M*(3*(X-x)*(Z-z)/(pow(Mag,5)))*(vol);
             SumY+=M*(3*(Y-y)*(Z-z)/(pow(Mag,5)))*(vol);
             SumZ+=M*(3*(Z-z)*(Z-z)/(pow(Mag,5))-1/(pow(Mag,3)))*(vol);
              }
         }
        }
      }
     BX[i][j][k]=SumX;  BY[i][j][k]=SumY; BZ[i][j][k]=SumZ;\
     myfile << i << "\t" << j << "\t" << k << "\t" << BX[i][j][k] << "\t" <<
         BY[i][j][k] << "\t" << BZ[i][j][k] << endl;
     }
   }
  }
```

```
  cout << endl << "Field Average Sums" << endl;
  float count;
  count=0;
  SumX=0; SumY=0; SumZ=0;
  for(int i=0; i<N; i++){
   cout << i << " ";
   for(int j=1; j<N; j++){
      for(int k=1; k<N; k++){
         x=(i-(N-1)/2)*step;
         y=(j-(N-1)/2)*step;
         z=(k-(N-1)/2)*step;
            if (R<(pow((float)x*x+y*y+z*z,(float).5))) continue;
               else{
                  SumX=SumX + BX[i][j][k];
                  SumY=SumY + BY[i][j][k];
                  SumZ=SumZ + BZ[i][j][k];
                  count = count + 1;
                  }
      }
   }
  }

  time( &finish );
  elapsed_time = -1*(difftime(start, finish));

  cout << endl <<"Computation time for " << (N-1) << " divisions in one
      direction: " << elapsed_time << " seconds." << endl << endl <<
     "On Axis:" << endl <<
     "At the Center BZ is " << BZ[(N-1)/2][(N-1)/2][(N-1)/2] << endl <<
     "At the Front, BZ is " << BZ[(N-1)/2][(N-1)/2][N] << endl <<
     "At the Back, BZ is " << BZ[(N-1)/2][(N-1)/2][0] << endl<<
     "2 steps off axis in all directions: BX=" << BX[(N-1)/2+2][(N-1)/2+2][(N
         -1)/2+2] <<
     " BY=" << BY[(N-1)/2+2][(N-1)/2+2][(N-1)/2+2] << endl << endl <<
     "The average through-space-fields inside the sphere are:" << endl <<
     "X: " << SumX/count << endl <<
     "Y: " << SumY/count << endl <<
     "Z: " << SumZ/count << endl << endl;

// loop to check the shape of the object
  for (int k=0; k<5; k++){
   for(int j=0; j<N; j++){
      for(int i=0; i<N; i++){
      cout <<  MagTest[i][j][k] << MagTest[i][j][k] << MagTest[i][j][k];
      }
      cout << endl;
   }
   cout << endl << endl;
  }

  cout << endl;

  int u;
  cout << "Please enter an integer value to end the program: ";
  cin >> u;
  cout << "The value you entered is " << u;
```

```
    myfile.close();

    return 0;
}
```

APPENDIX C

CELL FABRICATION PROCESS

The cells used in the measurement of $(\kappa_0)_{\mathrm{RbXe}}$ were ≈7 millimeter ID pyrex spheres filled with various gas pressures. This appendix explains the process by which a relatively accurate amount of gases was put into the cells. Figure C.1 shows the gas-handling/vacuum system used to clean and fill the cells.

A Pyrex "manifold" with 4 cells was constructed by a glass blower and attached to the vacuum system. A manifold is a"T"-shaped piece of Pyrex tubing with a Large U-bend on one end. The U-bend is a kinetic trap to aid in keeping the Rb from getting into the vacuum system. The top of the "T" is called the "retort". After attaching the manifold to the vacuum system, the entire system (manifold and gas-handling) was checked for leaks with a helium spray and a residual gas analyzer (RGA). Then a Rb ampule was dropped into the retort and the top of the retort was sealed by melting the Pyrex.

Once the Rb ampule has been dropped into the retort and the retort sealed, the interior of the cells should never be exposed to air again. However, before adding in the desired gas composition the cells must be "cleaned." The cleaning was done by wrapping the entire manifold except the U-bend and retort in heat tape and heating the manifold to 130+ °C for several days (or until the pressure gauge on the Turbo pump reads its lowest value for 12 hours or so).

After the Cells had been cleaned, the Rb needed to be moved into the cells from the retort. This was accomplished by heating the manifold with torches at low heat. The heat drives the Rb off of the walls and because the manifold is still under vacuum the Rb moves easily to walls where the temperature is low enough to collect Rb.

With Rb in the cells, and the manifold cooled down, gas could be introduced into the cells. Xe was done first since it can be frozen into the cells with LN_2 and with the entire system at vacuum most of the Xe would easily make it to the cell immersed under LN_2 on reasonable time scales (few minutes). From the gas canister, a previously measured volume is filled with a specific amount of Xe that, when frozen and then expanded, corresponds to

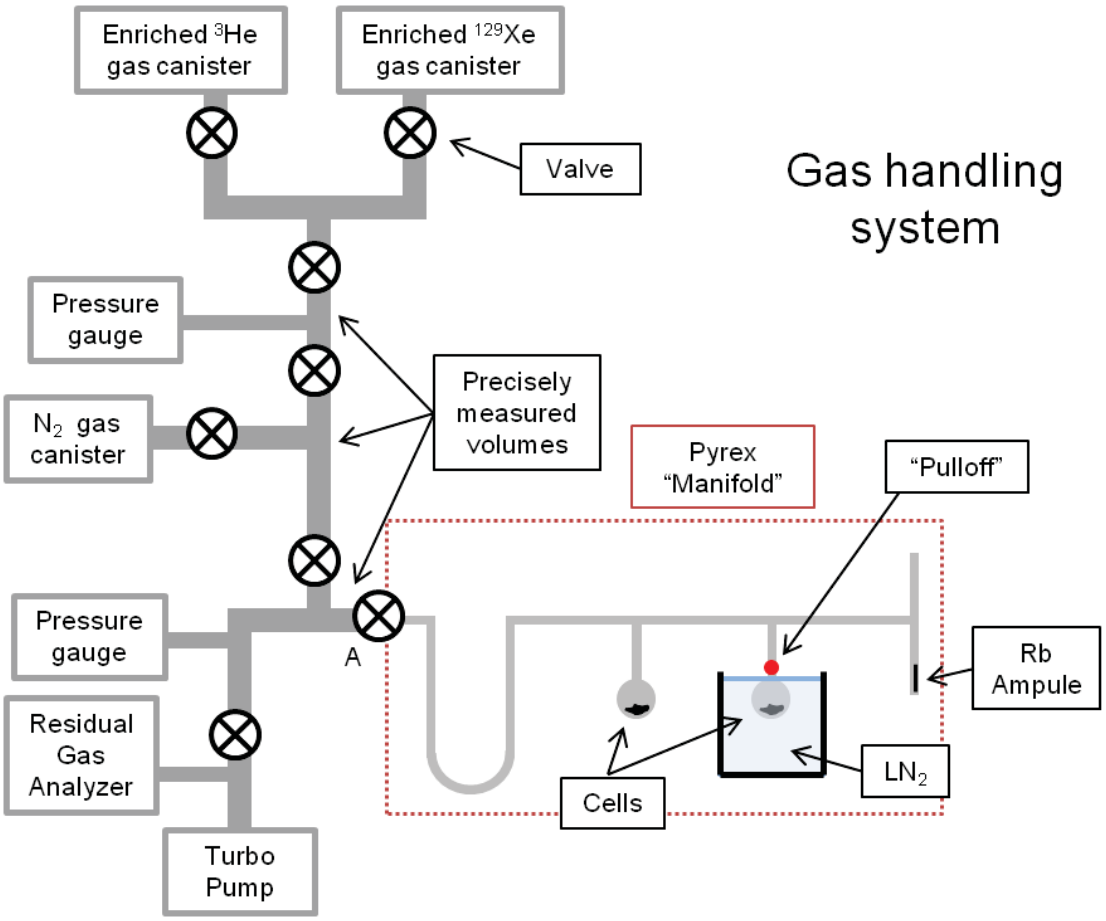

Figure C.1. Schematic of gas handling system used to clean and to fill cells with various gas mixtures. The manifold containing the cells is made by a glass blower, attached to the vacuum system with a Cajon fitting (A), and the volumed measured. A Rb ampule (≈1 gm) is dropped into the manifold and part of the manifold with the cells is sealed and heated with the Turbo pump open for several days. The Rb is moved into the cells with heat. Enriched Xe is allowed to fill one or more of the precisely measured volumes with a pre-calculated pressure and then is frozen into the cells with LN_2. ^{3}He and N_2 and then admitted to the manifold at less than atmospheric pressure. The N_2 partial pressure has to be low enough to avoid liquefying the N_2 in the cell. The cell is kept immersed in LN_2 while a torch is used to melt through the pulloff and remove the cell from the manifold.

the desired pressure inside the cell. The volume containing the Xe gas is then opened to the manifold where one cell is held under LN_2. All the pressure gauges immediately drop to zero when this happens and the only way to ensure Xe was in the cells was to keep the LN_2 level constant and wait a A few minutes (the real proof ^{129}Xe got into the cell was when a NMR signal was detected). ^{3}He was then added to the manifold to the desired pressure, and N_2 was added last. Note that no matter what pressure was put into the cells, the total

pressure at room temp was always less than atmosphere. Since the N_2 was added after the ^{3}He the distribution of gas in the manifold was definitely not uniform. To homogenize the gas, hot and cold air was blown on the manifold near the U-bend for ≈15 minutes with ≈2 minute periods. Throughout this heating and cooling the cell was always kept under LN_2.

Once the gas was homogenized the cell could be removed from the manifold. This was the hardest part of the procedure. A 1 cm sphere had to be held under LN_2 while a torch, a few millimeters above the LN_2 level, melted the Pyrex until it was sealed (called the "Pulloff"). This was accomplished with two graduate students and much cursing. One student held the cell under LN_2 with a pair of modified tweezers and maintained the LN_2 level with a Jiffy-Jack holding a dewer under the cell. The other student had a #1 glass-blowing torch on a full blast pointed at the Pyrex just above the LN_2. The difficulty was keeping the torch on long enough to melt through the pulloff because the LN_2 boiloff from the heat was rapid enough to frequently put out the torch. Nonetheless all cells were made successfully.

The cells were held under LN_2 because the Xe needed to stay frozen. The low temperature in the cell also had the advantage of increasing the ^{3}He and N_2 density by about a factor of 3. However, because the glass torch was right next to the cell at 77 K, we cannot claim high precision numbers for the gas densities. Hence the stated 50% uncertainty in the Xe pressure quoted in the caption of Table 2.1.

APPENDIX D

HYPERFINE SUBLEVEL TRANSITIONS AT LOW FIELD

The ground state hyperfine sublevel transition frequencies for arbitrary field are found by taking the difference between two m_{F} levels given by the Breit-Rabi equation

$$\frac{E}{h} = -\frac{\nu_{\mathrm{HF}}}{2(2I+1)} \pm \frac{\nu_{\mathrm{HF}}}{2}\left(1 + \frac{2m_{\mathrm{F}}}{I+1/2}\left(\frac{g_s\mu_{\mathrm{B}}}{h\nu_{\mathrm{HF}}}\mathbf{B}\right) + \left(\frac{g_s\mu_{\mathrm{B}}}{h\nu_{\mathrm{HF}}}\mathbf{B}\right)^2\right)^{1/2}. \tag{D.1}$$

The following simple calculation will be done for $F = I + 1/2$, i.e. the "+" sign in equation (D.1). Letting $x = \left(\frac{g_s\mu_{\mathrm{B}}}{h\nu_{\mathrm{HF}}}\mathbf{B}\right)$ and taking the difference between m_{F} and $m_{\mathrm{F}} - 1$ gives

$$(\nu_{\mathrm{F}} - \nu_{\mathrm{F\text{-}1}}) = -\frac{\nu_{\mathrm{HF}}}{2}\left(\left(1 + \frac{2m_{\mathrm{F}}}{I+1/2}(x) + (x)^2\right)^{1/2} - \left(1 + \frac{2(m_{\mathrm{F}}-1)}{I+1/2}(x) + (x)^2\right)^{1/2}\right). \tag{D.2}$$

Since $x \ll 1$ the x^2 can be ignored and the square root expanded out to second order.

$$\begin{aligned}(\nu_{\mathrm{F}} - \nu_{\mathrm{F\text{-}1}}) = -\frac{\nu_{\mathrm{HF}}}{2}\Bigg(1 + \frac{1}{2}\frac{4}{(2I+1)}(m_{\mathrm{F}})x - \frac{1}{8}\left(\frac{4}{2I+1}\right)^2 (m_{\mathrm{F}})^2 x^2 \\ - 1 - \frac{1}{2}\frac{4}{(2I+1)}(m_{\mathrm{F}}-1)x + \frac{1}{8}\left(\frac{4}{2I+1}\right)^2 (m_{\mathrm{F}}-1)^2 x^2\Bigg)\end{aligned} \tag{D.3}$$

$$(\nu_{\mathrm{F}} - \nu_{\mathrm{F\text{-}1}}) = \frac{\nu_{\mathrm{HF}}}{(2I+1)}\left(x - \frac{2}{(2I+1)}\left(m_{\mathrm{F}} - \frac{1}{2}\right)x^2\right) \tag{D.4}$$

This equation gives the sublevel transition frequency defined by $F = I + 1/2$ and $m_{\mathrm{F}} \leftrightarrow m_{\mathrm{F}} - 1$ as a function of field. However, the Rb atoms are experiencing a very small additional field ($\approx$2 mG) from collisions with polarized ^{129}Xe atoms which is well approximated by a derivative (2 mG$\ll$27 G) with respect to the magnetic field.

$$d(\nu_{\mathrm{F}} - \nu_{\mathrm{F\text{-}1}}) = \frac{g_s\mu_{\mathrm{B}}}{h(2I+1)}\left[1 - \left(m_{\mathrm{F}} - \frac{1}{2}\right)\frac{4}{(2I+1)}\frac{g_s\mu_{\mathrm{B}}}{h\nu_{\mathrm{HF}}}\mathbf{B_0}\right]d\mathbf{B} \tag{D.5}$$

In equation (D.5), $d\left(\nu_{\mathrm{F}}-\nu_{\text{F-1}}\right)$ is the same as $\Delta\nu_A$ in equations (2.3) and (3.1), and $\mathbf{B_0}$ is the static applied field. $d\mathbf{B}$ is the small additional field from collisions with polarized ^{129}Xe which is given by the field inside of a uniformly magnetized sphere enhanced by κ_0.

$$d\mathbf{B}=\frac{8\pi}{3}\mathbf{M}\rightarrow\frac{8\pi}{3}\kappa_0\left(\mu_{\mathrm{Xe}}\left[\mathrm{Xe}\right]P_{\mathrm{Xe}}\right) \tag{D.6}$$

$$\Delta\nu_{\mathrm{Rb}}=\frac{g_s\mu_{\mathrm{B}}}{h(2I+1)}\left[1-\left(m_{\mathrm{F}}-\frac{1}{2}\right)\frac{4}{(2I+1)}\frac{g_s\mu_{\mathrm{B}}}{h\nu_{\mathrm{HF}}}\mathbf{B_0}\right]\frac{8\pi}{3}\kappa_0\left(\mu_{\mathrm{Xe}}\left[\mathrm{Xe}\right]P_{\mathrm{Xe}}\right) \tag{D.7}$$

Optical pumping continuously adds angular momentum into the Rb vapor and, as a consequence, most of the EPR signal comes from edge-transitions ($\langle 2,-2\rangle\leftrightarrow\langle 2,-1\rangle$ and $\langle 2,2\rangle\leftrightarrow\langle 2,1\rangle$ for ^{87}Rb). Equation (D.7) can be written specifically for these edge-transitions as

$$\Delta\nu_{\mathrm{Rb}}=\frac{4}{3}\frac{\mu_{\mathrm{B}}g_{\mathrm{s}}}{(2I+1)}\gamma_{\mathrm{Xe}}K\left(\kappa_0\right)_{\mathrm{RbXe}}\left[\mathrm{Xe}\right]P_{Xe}\left(1\mp\frac{4I}{(2I+1)}\frac{\mu_{\mathrm{B}}g_{\mathrm{s}}}{h\nu_{\mathrm{HF}}}\mathbf{B_0}\right), \tag{D.8}$$

where the $\mp$ is for the $m_{\mathrm{F}}=\pm(I+1/2)$.

APPENDIX E

EQUIPMENT AND ELECTRONICS USED TO MEASURE ^{87}Rb EPR FREQUENCY

As shown in Figure 3.3, the electronics are broadly divided into high (≈20 MHz) and low (≈500 Hz) frequency components. Section 3.5 stated that the size of the Faraday rotation angle would be used to map and monitor ^{87}Rb hyperfine resonances. This appendix will describe how the high- and low-frequency electronics interact to achieve this. In addition photographs and schematics of equipment are shown in Figures E.1 and E.2

E.1 High Frequency Electronics and Demodulation

The RF excitation coils drive ^{87}Rb spins into coherent precession about the main magnetic field at the excitation frequency. Consequently the linearly polarized probe laser's plane of polarization is rotated at the excitation frequency as the transverse component of the ^{87}Rb spins points towards and away from the direction of propagation. To detect this oscillation of polarization, a linear polarizer is placed in front of the detection photo-diode at 45° with respect to the original polarization direction of the probe laser (see Figure 3.4). This is done because the transmitted intensity through a linear polarizer goes like $cos^2(\theta)$ where θ is the angle between the polarizer and light polarization directions and the derivative of the intensity with respect to θ has a maxima at 45°. An order of magnitude estimation of the size of the signal at the photo-diode using Equation (3.17) and the transmitted intensity gives about a 4% change in photocurrent. This is buried in the noise of a fast acting photo-diode and consequently we have to do high-frequency lock-in detection in order to extract the signal.

The small signal from the photo-diode is sent through a series of preamplifiers and then fed into a mixer that is driven at the same frequency as the RF exciting the ^{87}Rb atoms. Since a RF-mixer outputs the sum and the difference frequencies of the two inputs, and in our case the input frequencies are the same, the output from the mixer is a DC signal (and a really high frequency signal that is easily filtered) that corresponds to the relative

amplitudes of the two signals. For a steady signal driving the mixer, the DC output level will directly correlate to the size of the modulation at the photo-diode which is directly related to how much spin is in the transverse plane, or identically, how close to resonance the excitation frequency is. Whether this slowly varying DC signal, as a function of frequency, is absorptive or dispersive depends on the relative phase of the signal from the photo diode to the RF driving frequency. To adjust the relative phase and generate absorptive peaks in all situations, a phase shifter from Mini-Circuits was used to delay the reference frequency before going into the mixer.

The frequency synthesizer used in this experiment has the capability to perform frequency sweeps as well as receive a DC voltage that programs the output frequency (voltage controller oscillator, or VCO). The frequency sweep is necessary to generate a ^{87}Rb hyperfine spectrum, and the VCO feature is essential to lock-to and monitor a hyperfine transition frequency. In addition to these excellent features, it is a total and complete piece of junk.

This inexpensive and simple high-frequency lock-in scheme works very well and under the right conditions the single-shot signal to noise of a ^{87}Rb spectrum can be as much as 20:1.

E.2 Low Frequency Modulation and Frequency Locking

The low-frequency electronics are designed to provide an oscillating voltage at ≈500 Hz to the VCO which will modulate the excitation RF at the coil by about ≈1.2 kHz. This modulating RF will translate into a 500 Hz envelope modulation of the RF at the photo-diode as the RF frequency moves around a hyperfine resonance. The RF will be demodulated as described in section E.1 and the 500 Hz envelope modulation will be outputed as a 500 Hz sine wave from the mixer in the high-frequency section. This 500 Hz audio oscillation is then filtered and amplified as necessary and fed into a lock-in amplifier that is referenced to the audio source.

Depending on where the RF excitation frequency is with respect to the peak of the hyperfine transition, the amplitude of the 500 Hz voltage from the mixer will change. On the side of an absorptive resonance peak the amplitude will be largest, and at the peak the amplitude will be small and the frequency double (1 kHz). Therefore when this audio oscillation is fed into the lock-in amplifier the output of the lock-in as a function of RF frequency is a derivative of the resonance. For a well shaped peak, this derivative signal has a clean zero crossing with positive on one side, and negative on the other. This zero

crossing is what is used to force the output of the VCO to follow the frequency at the center of the hyperfine resonance.

To understand how the control circuit and the subsequent addition of the modulation voltage works, illustration with an example may be helpful. Consider the average output RF frequency of the VCO to be slightly high from the peak of a resonance. Of course the RF frequency is being modulated at 500 Hz at the same time. Let being on the high side of the hyperfine resonance in frequency have a negative voltage output from the lock-in amplifier. Fed directly into the VCO, the lock-in's negative voltage will force the VCO to reduce its frequency and move the lock-in voltage back towards zero. However, when the frequency of the VCO matches the peak of the resonance, the lock-in will output 0 volts and the VCO will move back towards its set point. This will cause the RF frequency to beat as the VCO sloshes between its set point and the peak of the resonance. This is a common problem with "proportional" only control and is easily solved with a capacitor to integrate the output voltage of the lock-in. The capacitor will add or subtract charge if the lock-in output is not zero, however, once the lock-in output is zero (peak of the resonance) the capacitor will hold whatever voltage it has and consequently not allow the VCO to drift back towards its set point. The control circuit used in this experiment to condition the output of the lock-in amplifier had both proportional and integral branches and is shown in Figure E.2.

The output from the control circuit is a slowly varying DC voltage that tells the VCO what frequency to output in order to keep the lock-in amplifier's output at zero. However, the VCO output frequency must also oscillate so the lock-in has a signal to process. To oscillate the VCO output a 500 Hz signal is added to the control circuit output before being fed into the VCO.

Figure E.1. Photograph of almost all of the electronic equipment used to monitor the ^{87}Rb EPR frequency. The labels are the same as in Table 3.1 and Figure 3.3. The preamplifiers (C) are located behind the power supplies (A) in a shielded box close to the photo-diode to reduce noise pickup.

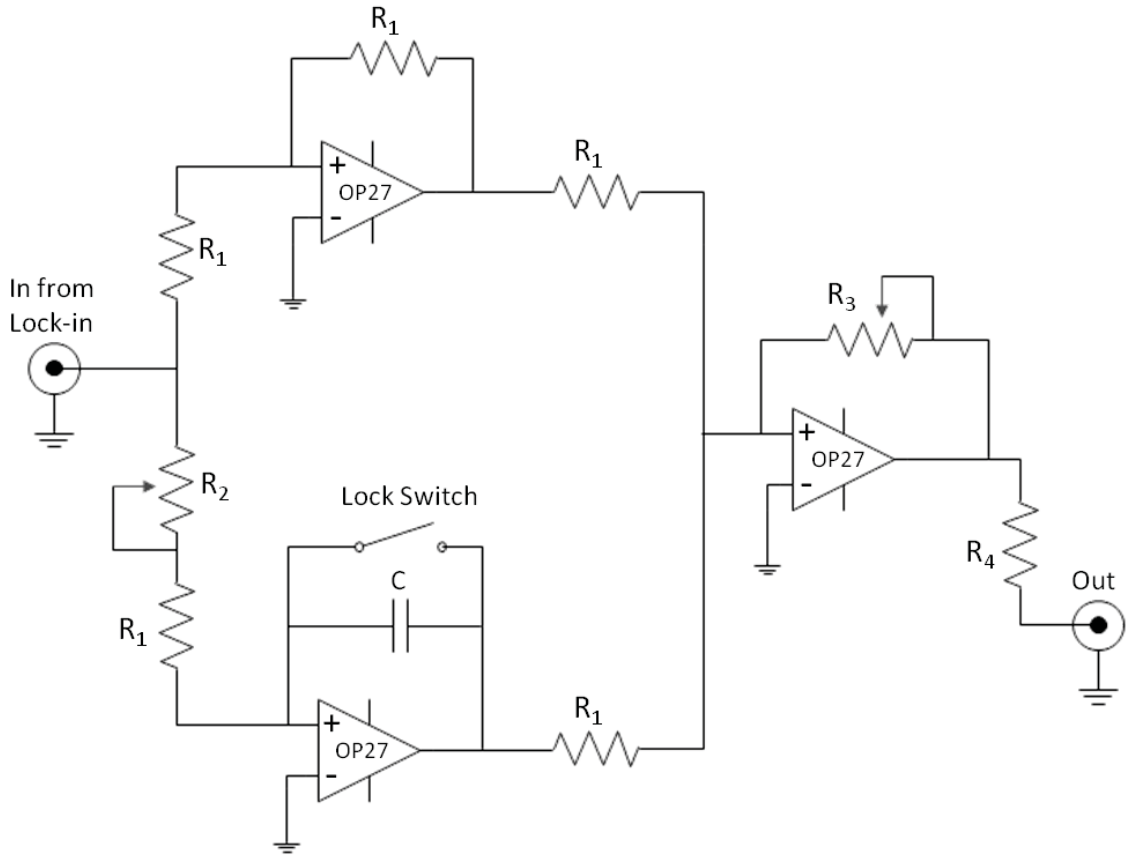

Figure E.2. Control Circuit used to condition the lock-in amplifier output before being fed to the VCO. The top branch is proportional control, and the bottom branch is integral control. The "lock switch" is used to control charging of the capacitor. With the switch closed the control circuit has only proportional control. The proportional and integral control are added together with an inverting summing junction with variable gain. R_1 =10kΩ, R_2 =20Ω-110kΩ, R_3 =30Ω-41.6kΩ, R_4 =2.2kΩ, C=1.94μF

APPENDIX F

PDB ENTRIES USED FOR CAST CALCULATIONS

Used CAST algorithm [43] implemented on the CASTp web server [25] (`http://sts.bioengr.uic.edu/castp`), with probe radii of 1.4 or 2 Å.

Atomic coordinates (PDB entries) used for calculations:

1. Y23A BPTI: 1BPT
2. F45S BPTI: 1FAN (F45A mutant) with A45S substitution modeled.
3. T4 lysozyme: 1L63 (WT* pseudo wild-type, with C54T and C97A substitutions)
4. T4 lysozyme L99A, site 1: 1C6K (L99A in WT* background in presence of 8 Atm Xe), with Xe atom 500 removed to open only site 1.
5. T4 lysozyme L99A, site 2: 1L83 (L99A in WT* background in presence of n-butyl benzene, which blocks site 1)
6. L19A Ribose binding protein, in open conformation: 1URP (wild-type protein) with modeled L19A substitution
7. L19A Ribose binding protein, in closed conformation: 2DRI (wild-type protein) with modeled L19A substitution
8. Maltose binding protein: 1OMP
9. CheY, inactive: 1JBE. The 1.08 Å crystal structure includes alternate conformations, which have been assigned to the inactive state and a "meta-active" state[63]. The atom positions for alternate conformation B were used.
10. CheY, active: 1FQW (with BeF^{3-} bound to Asp57 to mimic phosphorylation). The crystal contains two molecules in the asymmetric unit. The cavity volumes for both molecules were calculated and averaged.

11. Metmyoglobin, horse: 1YMB. The listed volume is the average of values for the four crystallographically-identified sites [69]. (54, 71, 74 and 19 $Å^3$).

12. Metmyoglobin, pig: 1MYG. The listed volume is the average for the four sites were identified by analogy to the horse protein [20] (40, 48, 60 and 31 $Å^3$).

13. Lipid transfer protein: 1TI2. This PDB entry includes 10 structures derived from NMR restraints. Structure 2 was determined to have the smalled RMS deviation from a computed mean structure and was used for volume calculations. The volume listed in Table 2 is the average of the calculated volumes for the four sites identified in reference [24] (59, 41, 58 and 28 $Å^3$).

REFERENCES

[1] Abragam, A. 1961, The Principles of Nuclear Magnetism, International Series of Monographs on Physics (Clarendon Press)

[2] Appelt, S., Baranga, A. B.-A., Erickson, C. J., Romalis, M. V., Young, A. R., & Happer, W. 1998, Phys. Rev. A, 58, 1412

[3] Arditi, M., & Carver, T. R. 1961, Phys. Rev., 124, 800

[4] Babcock, E. 2005, PhD thesis, University of Wisconsin Madison

[5] Bain, A. D. 2003, Progress in Nuclear Magnetic Resonance Spectroscopy, 43, 63

[6] Baranga, A. B.-A., Appelt, S., Erickson, C. J., Young, A. R., & Happer, W. 1998, Phys. Rev. A, 58, 2282

[7] Barrat, J., & Cohen-Tannoudji, C. 1961, J. Phys. Radium, 22, 443

[8] Barton, A. S., Newbury, N. R., Cates, G. D., Driehuys, B., Middleton, H., & Saam, B. 1994, Phys. Rev. A, 49, 2766

[9] Baumer, D., Brunner, E., Blümler, P., Zänker, P. P., & Spiess, H. W. 2006, Angew. Chem. Int. Ed., 45, 7282

[10] Bouchiat, C. C., Bouchiat, M. A., & Pottier, L. C. L. 1969, Phys. Rev., 181, 144

[11] Bouchiat, M. A., Brossel, J., & Pottier, L. C. 1972, The Journal of Chemical Physics, 56, 3703

[12] Bouchiat, M. A., Carver, T. R., & Varnum, C. M. 1960, Phys. Rev. Lett., 5, 373

[13] Breit, G., & Rabi, I. I. 1931, Phys. Rev., 38, 2082

[14] Brossel, J., Kastler, A., & Winter, J. 1952, J. Phys. Radium, 13, 668

[15] Carver, T. R., & Slichter, C. P. 1956, Phys. Rev., 102, 975

[16] Cates, G. D., Benton, D. R., Gatzke, M., Happer, W., Hasson, K. C., & Newbury, N. R. 1990, Phys. Rev. Lett., 65, 2591

[17] Cates, G. D., Fitzgerald, R. J., Barton, A. S., Bogorad, P., Gatzke, M., Newbury, N. R., & Saam, B. 1992, Phys. Rev. A, 45, 4631

[18] Chann, B., Babcock, E., Anderson, L. W., & Walker, T. G. 2002, Phys. Rev. A, 66, 032703

[19] Chann, B., Nelson, I., & Walker, T. G. 2000, Opt. Lett., 25, 1352

[20] Corda, M., Era, B., Fais, A., & Casu, M. 2004, Biochim. Biophys. Acta, 1674, 182

[21] Corney, A. 1977, Atomic and Laser Spectroscopy (Oxford University Press)

[22] Desvaux, H., Dubois, L., Huber, G., Quillin, M. L., Berthault, P., & Matthews, B. W. 2005, J. Am. Chem. Soc., 127, 11676

[23] Driehuys, B., Cates, G. D., Miron, E., Sauer, K., Walter, D. K., & Happer, W. 1996, Applied Physics Letters, 69, 1668

[24] Dubois, L., Da Silva, P., Landon, C., Huber, J. G., Ponchet, M., Vovelle, F., Bertelsen, E., & Desvaux, H. 2004, J. Am. Chem. Soc., 126, 15738

[25] Dundas, J., Ouyang, Z., Tseng, J., Binkowski, A., Turpaz, Y., & Liang, J. 2006, Nucl. Acids Res., 34, W116

[26] Finney, J. L. 1975, J. Mol. Biol., 96, 721

[27] Fitzgerald, R. J., Gatzke, M., Fox, D. C., Cates, G. D., & Happer, W. 1999, Phys. Rev. B, 59, 8795

[28] Gatzke, M., Cates, G. D., Driehuys, B., Fox, D., Happer, W., & Saam, B. 1993, Phys. Rev. Lett., 70, 690

[29] Grover, B. C. 1978, Phys. Rev. Lett., 40, 391

[30] Happer, W. 1972, Rev. Mod. Phys., 44, 169

[31] Happer, W., Miron, E., Schaefer, S., Schreiber, D., van Wijngaarden, W. A., & Zeng, X. 1984, Phys. Rev. A, 29, 3092

[32] Happer, W., & Tam, A. C. 1977, Phys. Rev. A, 16, 1877

[33] Jackson, J. 1999, Classical Electrodynamics (Wiley)

[34] Kadlecek, S., Anderson, L. W., Erickson, C. J., & Walker, T. G. 2001, Phys. Rev. A, 64, 052717

[35] Kadlecek, S. J. 1999, PhD thesis, University of Wisconsin Madison

[36] Kaushik, S. S., et al. 2011, Magnetic Resonance in Medicine, 65, 1154

[37] Kestin, J., Knierim, K., Mason, E. A., Najafi, B., Ro, S. T., & Waldman, M. 1984, Journal of Physical and Chemical Reference Data, 13, 229

[38] Killian, T. J. 1926, Phys. Rev., 27, 578

[39] Knight, W. D. 1949, Phys. Rev., 76, 1259

[40] Kriminski, S., Caylor, C. L., Nonato, M. C., Finkelstein, K. D., & Thorne, R. E. 2002, Acta Cryst., D58, 459

[41] Kristensen, M., van Eijkelenborg, M. A., & Woerdman, J. P. 1994, Phys. Rev. Lett., 72, 2155

[42] Kuzma, N. N., Patton, B., Raman, K., & Happer, W. 2002, Phys. Rev. Lett., 88, 147602

[43] Liang, J., Edelsbrunner, H., & Woodward, C. 1998, Protein Sci., 7, 1884

[44] Locci, E., Dehouck, Y., Casu, M., Saba, G., Lai, A., Luhmer, M., Reisse, J., & Bartik, K. 2001, J. Magn. Reson., 150, 167

[45] Lowery, T. J., Rubin, S. M., Ruiz, E. J., Pines, A., & Wemmer, D. E. 2004, Angew. Chem. Int. Ed., 43, 6320

[46] Ma, Z. L., Sorte, E. G., & Saam, B. 2011, Phys. Rev. Lett., 106, 193005

[47] Mathur, B. S., Tang, H., & Happer, W. 1968, Phys. Rev., 171, 11

[48] Nelson, I. A., & Walker, T. G. 2001, Phys. Rev. A, 65, 012712

[49] NIST. 2011, Xenon, nIST Chemistry WebBook

[50] Overhauser, A. W. 1953, Phys. Rev., 92, 411

[51] Patton, B. 2007, PhD thesis, Princeton University

[52] Reif, F. 1965, Fundamentals of Statistical and Thermal Physics, ed. E. U. Condon (McGraw-Hill)

[53] Richards, F. M. 1974, J. Mol. Biol., 82, 1

[54] Romalis, M. V., & Cates, G. D. 1998, Phys. Rev. A, 58, 3004

[55] Romalis, M. V., Miron, E., & Cates, G. D. 1997, Phys. Rev. A, 56, 4569

[56] Rubin, S. M., Lee, S.-Y., Ruiz, E., Pines, A., & Wemmer, D. E. 2002, J. Mol. Bio., 322, 425

[57] Ruset, I. C., Ketel, S., & Hersman, F. W. 2006, Phys. Rev. Lett., 96, 053002

[58] Sandstrm, J. 1982, Dynamic NMR Spectroscopy (Academic Press)

[59] Schaefer, S. R., Cates, G. D., Chien, T.-R., Gonatas, D., Happer, W., & Walker, T. G. 1989, Phys. Rev. A, 39, 5613

[60] Schrank, G. 2009, PhD thesis, University of Utah

[61] Schrank, G., Ma, Z., Schoeck, A., & Saam, B. 2009, Phys. Rev. A, 80, 063424

[62] Sears, D. R., & Klug, H. P. 1962, The Journal of Chemical Physics, 37, 3002

[63] Simonovic, M., & Volz, K. 2001, J. Biol. Chem., 276, 28637

[64] Slichter, C. P. 1996, Principles of Magnetic Resonance, 3rd edn., ed. H. K. V. Lotsch, Solid-State Sciences 1 (Springer)

[65] Solvignon, P., et al. 2008, Phys. Rev. Lett., 101, 182502

[66] Steck, D. A. 2010, Rubidium 87 D Line Data

[67] Sukstanskii, A. L., & Yablonskiy, D. A. 2012, Magnetic Resonance in Medicine, 67, 856

[68] Teng, T.-Y., & Moffat, K. 1998, J. Appl. Cryst., 31, 252

[69] Tilton, Jr., R. F., Kuntz, Jr., I. D., & Petsko, G. A. 1984, Biochemistry, 23, 2849

[70] Vliegen, E., Kadlecek, S., Anderson, L., Walker, T., Erickson, C., & Happer, W. 2000, Nuclear Instruments and Methods in Physics Research A, 460, 444

[71] Wagshul, M. E., & Chupp, T. E. 1989, Phys. Rev. A, 40, 4447

[72] Walker, T. G., & Happer, W. 1997, Rev. Mod. Phys., 69, 629

[73] Wu, Z., Kitano, M., Happer, W., Hou, M., & Daniels, J. 1986, Appl. Opt., 25, 4483

[74] Zeng, X., Wu, Z., Call, T., Miron, E., Schreiber, D., & Happer, W. 1985, Phys. Rev. A, 31, 260

[75] Zhou, X., Graziani, D., & Pines, A. 2009, Proceedings of the National Academy of Sciences, 106, 16903